THE UNIVERSITY *of* EDINBURGH

Modelling Collective Behaviour and Pattern Formation in Bacterial Colonies

Fred Farrell

A thesis submitted in fulfilment of the requirements
for the degree of Doctor of Philosophy
to the
University of Edinburgh
August 2014

Abstract

In this Thesis I present simulation- and theory-based studies of pattern formation and growth in collections of micro-organisms, in particular bacterial colonies. The aim of these studies is to introduce simple models of the 'micro-scale' behaviour of bacterial cells in order to study the emergent behaviour of large collections of them. To do this, computer simulations and theoretical techniques from statistical physics, and in particular non-equilibrium statistical physics, were used, as the systems under study are far from thermodynamic equilibrium, in common with most biological systems. Since the elements making up these sytems – the micro-organisms – are active, constantly transducing energy from their environment in order to move and grow, they can be viewed as 'active matter' systems.

First, I describe my work on a generalization of an archetypal model of active matter – the Vicsek model of flocking behaviour – in which the speed of motion of active particles depends on the local density of particles. Such an interaction had previously been shown to be responsible for some forms of pattern formation in bacterial colonies grown on agar plates in the laboratory. Simulations and theory demonstrated a variety of pattern formation in this system, and these results may be relevant to explaining behaviour observed in experiments done on collections of molecular motors and actin fibres.

I then go on to describe work on modelling pattern formation and growth in bacterial biofilms - dense colonies of cells growing on top of solid surfaces. I introduce a simple simulation model for the growth of non-motile cells on a flat surface, whereby they move only by growing and pushing on each other as they grow. Such colonies have previously been observed experimentally to demonstrate a transition from round to 'branched' colonies, with a pattern similar to diffusion-limited aggregation. From these simulations and analytical modelling, a theory of the growth of such colonies is developed which is quite different from previous

theories. For example, I find that the colony cannot grow at a constant speed if the cells are not compressible.

Finally, I present some results on genetic drift and evolution in growing bacterial colonies. Genetic drift is greatly enhanced in colonies which are expanding in space, as only a few individuals at the edge of the population are able to pass on their genes onto their progeny. The individual-based simulations of biofilms described above are used to analyse which factors - such as the shape of the colony, the thickness of the growing layer of cells, and the interactions between the cells - affect the rate of genetic drift and the probability of fixation of beneficial mutations. This has implications, for example, for the evolution of antibiotic resistance in such colonies.

Lay Summary

In this Thesis I describe the research I have done during my PhD, using computer models and mathematics to make models of the behaviour of colonies of bacteria. The aim of this is to help understand what happens when large numbers of bacteria interact with each other, as they might do in the laboratory on a Petri dish, or in the natural environment such as inside an animal or human host. My aim was to use models to better understand what is going on in these situations, which could for example help us treat diseases which involve biofilms growing inside humans.

My research involved two somewhat separate projects. In the first project, I looked at a model of swimming bacteria, where the bacteria align their direction of motion with their neighbours, leading to a situation where all the cells move in the same direction, known as 'flocking' behaviour, as in a flock of birds. I introduced a new feature to this model in which the cells' speed depended on how many cells are nearby. This led to some interesting new behaviour, such as the formation of moving streaks or lanes of bacteria, which was similar to what has been observed in some experiments on colonies of swimming bacteria.

In the second project I looked at a model of a growing colony of bacteria on a surface. I modelled the cells very simply as elastic rods which push each other out of the way as they grow, and consume a nutrient. We used the model to explain an experimental phenomenon where a colony will either grow into a round colony or a complicated branching pattern depending on the initial amount of nutrient. I also used the model to look at the evolution of genetic mutations which make cells grow faster, such as mutations for antibiotic resistance in a human disease-causing bacterium. I found that the shape of the colony - round or branched - has a significant affect on the rate at which such mutstions appear.

Declaration

Except where otherwise stated, the research undertaken in this thesis was the unaided work of the author. Where the work was done in collaboration with others, a significant contribution was made by the author.

F. D. C. Farrell
August 2014

Acknowledgements

I would like to thank the following people:

Dr. Davide Marenduzzo, for his constant support, encouragement and optimism and for being such a helpful and reliable supervisor.

Dr. Bartlomiej Waclaw, with whom I collaborated extensively on my second research project on growing bacterial colonies, and who has been a pleasure to work with.

Dr. Julien Tailleur, who helped a great deal in directing the research on the modified Vicsek model and working out the mathematics describing it.

Prof. Martin Evans, my second supervisor, for help with manuscripts and the Thesis, and general advice.

Finally, the inhabitants of Room 1511, Alys Jepson, Steve Court, Giula Foffano and Matt Carr, for much help and moral support.

Contents

Chapter 1

Introduction

1.1 Active matter and collective behaviour

Biological matter is in many ways different from any other kind of matter – it is responsive, mutable. A major reason for this is that the matter making up biological systems is constantly taking energy from the environment and converting it into other forms, usually by the conversion of the molecule adenosine triphosphate (ATP) into adenosine diphosphate (ADP), in order to grow, move or reproduce. This constant energy flux means that such systems are not in thermodynamic equilibrium, and are often *far* from equilibrium; therefore the standard results of equilibrium thermodynamics and statistical mechanics do not apply. Such far-from-equilibrium, energetically driven matter is often termed *active matter* [1, 2], and is interesting to study both because it is crucial to understanding how biological matter works, and because the physics of far-from-equilibrium systems is different from and in many ways more complicated than that of equilibrium systems, and is still far from well understood. The methods used to study active matter include generalizations of theoretical techniques from statistical physics and condensed matter, as well as computer simulation and experiment.

1.1.1 Models of collective animal behaviour and flocking

One fascinating area to which these ideas have been applied is the study of flocking behaviours. Flocking phenomena are some of the most beautiful in nature, classic

examples being the complex and ordered motion of flocks of birds and schools of fish, where thousands of individuals move coherently and respond to outside stimuli, despite the fact each individual has very limited information about the flock as a whole - for a popular article on flocking see [3], and for an interesting review of collective animal behaviour from a biological perspective see [4]. These phenomena have received attention from statistical physicists as they concern the emergent behaviour which occurs when a group of agents interacting with each other in fairly simple ways are brought together in large numbers; this is somewhat analogous to the study of interacting systems in traditional statistical physics, although obviously the interactions between organisms are rather more complicated than those between atoms and molecules.

The statistical mechanical study of flocking began with the seminal work of Vicsek in 1995 [5] (though Reynolds [6] had earlier proposed a similar model in the context of computer animation, in 1987), who introduced a minimal model whereby particles move at a constant speed, and their only interaction is to align their direction of motion with each other – at each time step particles adjust their direction to the local average within some radius R, subject to some noise. Simulations (and subsequently analytical work [7]) demonstrated that the Vicsek model exhibits a non-equilibrium phase transition from a disordered state where particles move randomly, to a state with polar order where the particles move together, i.e. a flocking state. Of particular interest to physicists was the fact that this transition occured even in two dimensions, constrasting with equilibrium sytems, where a two-dimensional system with local interactions and a continuous order parameter cannot undergo a true phase transition (the Mermin-Wagner theorem [8]). The Vicsek model was hugely influential, and led to a large amount of further work [9, 10, 11, 12, 13, 14]. From a statistical physics point of view, there has been a lot of work characterising the dynamical transition and the ordered and disordered phases quantitatively. For example, it is still somewhat controversial whether the transition is continuous or discontinuous [10, 15]. The flocking state has some interesting statistical properties, such as far larger number fluctuations than are observed in an equilibrium fluid, and the existence of an instability to the formation of travelling waves of high density [7, 16, 13].

On the other hand, the Vicsek model has inspired a lot of work geared more towards understanding actual animal groups. Many more detailed models of

the behaviour of the agents in a flock have been created, but they still usually contain the same basic idea of agents which propel themselves forwards and interact in simple ways (attraction, repulsion, alignment) with the animals close to them. For example, the work of Couzin *et al.* uses such a model to show how different structures such as flocks, swarms and vortices may form, and how information about external conditions and individuals' positions within the group are transmitted through the flock [17, 18]. The work of Hemelrijk *et al.* on starling flocks [19, 20], again using a flocking model with attraction, repulsion and alignment, but also including some elements of the aerodynamics of flight, showed how the difficulty of changing speed quickly and the fact that birds need to bank when turning can explain many of the features of the flocks, such as their amorphous shape. There have also been experimental studies, such as the STARFLAG project [21, 22, 23], which made movies of starling flocks roosting at dusk above Rome, and used these to make three-dimensional reconstructions of the paths of every bird. An important result of this work was that the birds align with their neighbours using 'topological' rather than 'metric' distance: that is, they tend to align with about seven of their nearest neighbours regardless of how far away they are, rather than all the neighbours within a certain distance as in the Vicsek model.

More relevantly to this Thesis, flocking models have also been used to understand the behaviour of micro-organisms. Dense suspensions of bacterial cells are often observed to undergo spontaneous large-scale flows in a way which is similar to a flocking transition [24, 25]. These flows often appear unstable, and can even be described as turbulent [26]. Modelling work on these systems has included simuations of dense collections of self-propelled rods on a substrate [27, 28, 29]. In these models, hard rods propel themselves along their axes, and the steric interaction between them leads to alignment, and therefore to a flocking state as in the Vicsek model. Another class of models includes the fluid in which the cells are swimming, as the hydrodynamics of this fluid has important effects [30]. Indeed, hydrodynamic interactions between the cells cause the flocking state where all the cells are swimming in the same direction to be unstable, and the nature of this instability depends on whether the cells 'pull' (e.g. with cilia, as many algal cells) or 'push' (e.g. with a flagellum, as many bacteria) themselves through the fluid [31].

1.1.2 Active gels and materials

Another area in which the idea of active matter has been very useful is in the study of the cellular cytoskeleton. The cytoskeleton is what gives cells their shape and material properties, and is a three-dimensionsal network of polar elastic filaments such as actin [32, 33]. Depending on the lifetime and degree of cross-linking of these filaments, the cytoskeleton can have properties ranging from a viscous fluid to an elastic gel. The material is also highly active, consuming ATP to constantly polymerize and depolymerize the actin fibres. Additionally, myosin molecular motors move along the fibres, causing them to contract and therefore changing the properties of the network [34, 35]. The cytoskeleon can therefore be modelled as an active viscoelastic fluid, using hydrodynamic equations (similar to the normal Navier-Stokes equations of an equilibirum fluid), with additional terms to take into account the contractile activity. Often, in addition to the density and velocity fields used to describe a fluid, an additional field $\mathbf{p}(\mathbf{x})$ is used to describe the polarity of the actin filaments [36, 37]. This modelling has shown that such an active polar gel can exhibit effects such as spontaneous polarization of the actin filaments, and instabilities such as asters, vortices and spirals [37, 38, 39].

On a larger scale, collections of cells, such as animal tissues, can also be thought of as active gels, since they are made of cells which adhere to one another and generate active stresses [40, 41]. In a tissue, an additional important source of activity is growth - the fact that the cells grow, reproduce and die (apoptosis) has effects on the material properties of the tissue. In a similar fashion to to the case of the cytoskeleton, hydrodynamic equations with additional terms to describe this activity can be written down [41, 42]. These models have been used to study, for example, buckling instabilities in epithelial tissues such as those in the intestines [43, 44], the competition between healthy and cancerous tissues in tumour growth [45], and instabilities occuring during early embryo development [46].

1.2 Collective behaviour and pattern formation in bacterial colonies

In this Thesis I mostly focus on studying bacterial colonies as active matter systems. Bacteria have often in the past mostly been characterized as living as individual cells, swimming or suspended in a fluid. Recently, however, it has increasingly been recognized that bacteria often live in dense communities of cells, and that interactions between the cells are very important [47, 48]. In particular, they exhibit what is known as 'quorum sensing': cells produce small signalling molecules which are released into the environemnt, and are also capable of sensing the concentration of these molecules, so that they act as a proxy of the local density of bacteria [49]. The cells then use this information to control many aspects of their behaviour, such as growth rate, virulence and motility. It is thought that quorum sensing may have been an early step towards the development of multicellularity.

A particularly important multicellular phenomenon in bacteria is the formation of biofilms. Biofilms are dense collections of bacterial cells which grow on two-dimensional surfaces [47]. These are extremely prevalent in nature (biofilms will colonize almost any available surface) and are implicated in a wide variety of diseases, for example cystic fibrosis and endocarditis; they also cause health problems when they grow on hospital equipment and indwelling medical devices [50]. A familiar example of a biofilm is dental plaque. They are particularly troublesome because bacteria in biofilms exhibit enhanced resistance to antibiotic agents - this may indeed be one reason why they form [51]. They also cause problems in industrial settings, forming on surfaces that obstruct fluid flow or contaminate drinking water [48].

In a biofilm, the bacterial cells interact with each other in many ways. The initial formation of a biofilm involves quorum sensing: when the density of bacterial cells is large enough, genes involved in the formation of the biofilm will be activated [52]. Cells in a biofilm undergo phenotypic changes, and will strongly adhere to the surface, and produce material, primarily polysaccharides, which give the biofilm structure (this is known as the extracellular polymeric substance or EPS) [47]. Biofilms also exhibit complex structures, such as channels for the transport of nutrient and waste products [53] and structures similar to

fruiting bodies from which cells sporulate [54]. They are also often made up of many different species, with the different species often stratifying into defined areas of the biofilm and having different behaviours (e.g. metabolising different nutrients) [55, 56]. Fig. 1.1 is a schematic showing the development of a typical biofilm.

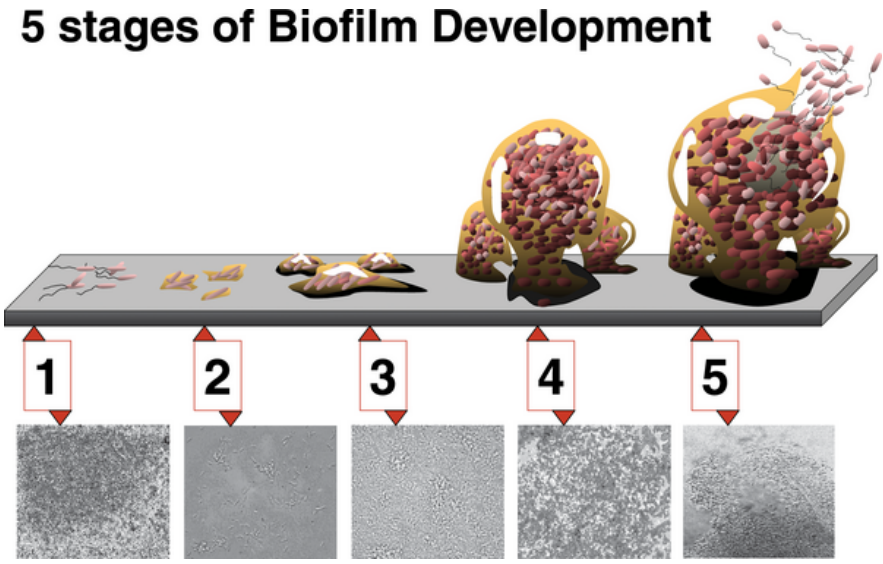

Figure 1.1: Reproduced from [57]. Diagram showing successive stages of the formation of a typical biofilm: cells first collect at a surface (1), then they lose their motility and start to produce EPS (2). The biofilm then grows (3-4), and may eventually reach a stage where cells are released back into the surrounding fluid in a planktonic state (5). Images are of a biofilm of *P. aeruginosa*.

It is possible, however, that many of these structures may not form by complex intercellular signalling as in a eukaryotic organism, but instead can self organize and emerge due to the interaction of the cells which grow, interact mechanically and compete for nutrients, in a way more similar to the collective bahaviour of flocks of birds or schools of fish described in the last section [55]. This idea is supported by many computational models of biofilm growth which exhibit the formation of rather complex structures such as branches and channels in the absence of any intercellular signalling effects [58, 59, 60, 61]. Additionally, experiments where bacteria are cultured on agar plates can give an insight into pattern formation in biofilms: even in a simple case where a single bacterial strain is grown on top of an agar surface, a wide variety of complex patterns are seen, depending on the strain used and the amount of nutrient available [54, 62, 63], see

Fig. 1.2 for some examples. Many of these patterns have similarities to non-living growth processes, such as the growth of crystals or the aggregation of diffusing particles.

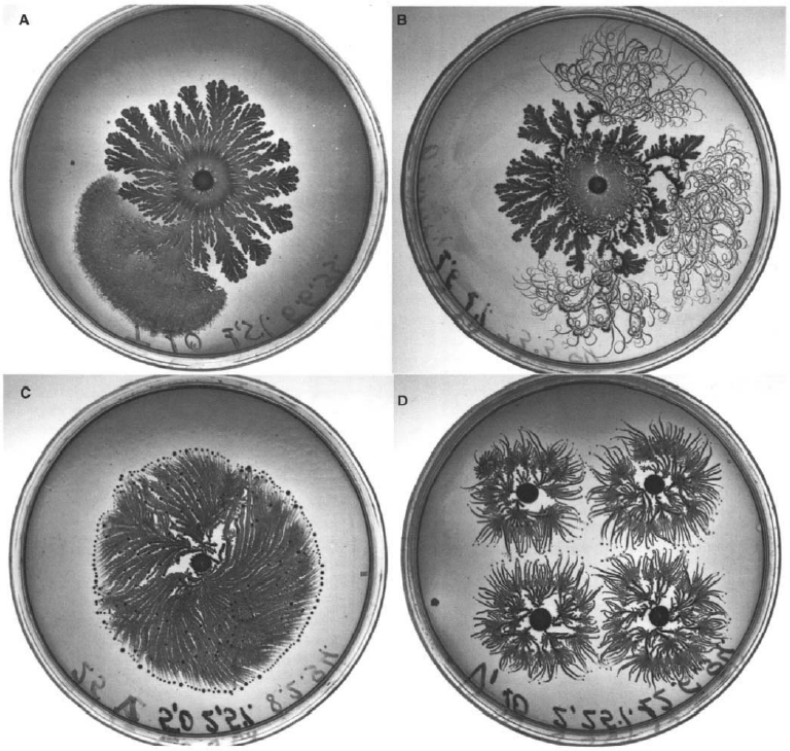

Figure 1.2: Reproduced from [63]. Colonies of *Bacillus subtilis* grown in petri dishes on agar, showing a variety of rather complex patterns. A and B are branching patterns caused by nutrient scarcity, but some cells, either due to mutation or a phenotypic change, have broken away and exhibit different behaviours. C and D are formed by rotating rafts of cells, visible as small black circles, leaving behind non-motile cells.

It is also interesting to consider biofilms from an evolutionary perspective. The cells making up a biofilm are in competition with each other for space and nutrients, but it may also be useful for them to cooperate, for example by producing EPS and chemicals to break down metabolites in the environment. Under some circumstances, the spatial structure of biofilms may make cooperation more evolutionarily stable than in well-mixed populations [64], but cooperation will not always be favoured, especially when multiple species are present [56, 65]. The presence of competition between cells is a difference between biofilms and truly multicellular organisms (although of course the cooperation is not perfect

even in multicellular organisms, as in the case of diseases such as cancer). The spatial structure present in biofilms has been shown to affect how likely it is that a beneficial genetic mutation (i.e. a mutation whuch makes the colony grow more quickly) will survive and take over the population rather than dying out due to the stochastic nature of the competition between cells [66, 67]. In a pathogenic biofilm, this will affect, for example, how quickly the cells will become resistant to an antibiotic.

1.3 Present work and thesis outline

In this Thesis I present work done during my PhD on models of the collective behaviour of bacteria. In Chapter 2 I describe some of the techniques and ideas used in this, both computational and analytical, consider their strengths and weaknesses and give some examples of their use. In Chapter 3 I describe a generalization of a flocking model in which the speed of propulsion of the particles depends on their local density. This was originally intended as a model for bacterial cells, which are known sometimes to vary their motility as a function of the local density of cells via chemotaxis (a kind of quorum sensing), but is also applicable to other instances of active matter, such as assemblages of molecular motors and actin fibres. I found that this model leads to novel instabilities which are similar to what is seen in *in vitro* experiments on molecular motors, and develop a continuum 'hydrodynamic' theory of the model which is in good agreement with the microscopic simulations. In Chapter 4 I describe a model of the growth of bacterial colonies in biofilms, made up of non-motile cells. In our model, which differs significantly from previous models of colony growth using generalized Fisher-Kolmogorov equations [58, 68, 69], cells grow and divide on a substrate, pushing each other out of the way as they grow, which leads to the expansion of the colony. This model was simulated using an individual-based simulation of the cells and the forces between them, and we also developed an analytical theory which describes the cells as an active, growing fluid. I derive some surprising results, such as that a round, two-dimensional colony made up of incompressible cells cannot in general grow at a constant speed – the cells must either be compressed or be pushed up into the third dimesion. Finally, in Chapter 5 I use a generalization of this model of colony growth to study evolution

in growing colonies. The fact that such a population of cells is expanding, rather than being well-mixed in space or spatially structured but fixed in size, has important effects on evolution, greatly increasing the amount of genetic drift at the expanding frontier and therefore reducing the effectiveness of selection. I present results on the rates of fixation of beneficial mutations, an important measure of how quickly the population adapts to its environment, and how this depends on properties such as the morphology of the colony.

Chapter 2

Methods and models

2.1 Introduction

In this section I describe the methods used to carry out my research. These consisted of extensive computer simulations of active matter systems, supported by analytical work to aid in elucidating the physics and general principles underlying the results of the simulations.

2.2 Agent-based models

The aim of my research is to understand active matter systems such as colonies of bacteria. Active matter systems usually consist of a large number of individuals (these might be molecules, cells or even macroscopic organisms), which interact with each other in certain ways. The main method I use to simulate such systems is so-called 'agent-based' (or individual-based) modelling: that is the individuals or 'agents' which make up the system and their interactions are simulated directly. The emergent behaviour which occurs when many agents are brought together can therefore be observed. The number of agents which can be considered using modern computing power is fairly large (10^5 - 10^6), and often leads to surprising results which could not have easily been predicted from the underlying interactions. The method is analogous to molecular dynamics in statistical physics, in which interactions between individual atoms or molecules are directly simulated [70].

Agent-based models are often used in active matter, for example in the models

of flocking behaviour, cellections of swimmers and active gels described in the last chapter. They are also used in a wide range of other circumstances where it is necessary to model the interactions of a large number of agents, such as the flow of traffic [71, 72] and pedestrians [73] or the spread of epidemics on human social networks [74, 75]. They have found use in ecology to explain patterns of species diversity [76], and in linguistics to describe the language change and evolution [77, 78]. They are also increasingly used in economics, where the idea is that an economy is made up of many agents (e.g. firms and consumers) who have strategies (e.g. when to buy or sell a good and at what price), which they can change as they interact with each other through the market [79, 80, 81].

Agent-based models, then, are very useful as they allow us to simply model what happens in a complex system given the behaviour of the agents which make it up. However, there are certainly problems and difficulties associated with them. The behaviour of the individuals usually has to be enormously simplified, especially if we are modelling animals or humans, with all their complexity reduced down to a few simple behavioural rules. Clearly, there are many possible ways to do this; we need to decide which interactions and behaviours we think are important. This also means that such models generally have quite a large number of parameters which are often difficult to calibrate. The main way these models are useful is in elucidating what the most important features of a system are, and in demonstrating that complex collective effects can arise from simple interactions without the need for extensive coordination between the agents. We saw this in the last chapter, for example, in the transition to a flocking state without the need for leadership in the Vicsek model [5], and in pattern formation without extensive intercellular signalling in biofilms [58, 59]. Often, they are effectively used as 'null models', showing what the simplest possible microscopic behaviour leading to an observed macroscopic phenomenon can be.

Another idea is that of 'universality': often, the emergent behaviours of a system do not actually depend very much on the details of the microscopic interactions. (For reviews of the concept of universality in statistical physics, see [82, 83].) This cannot be relied upon *a priori*, however, especially in out-of-equilibrium systems, where seemingly insignificant details *do* sometimes have an impact on the large-scale behaviour, as in the case of angular versus vector noise in the Vicsek model described below.

2.2.1 Spatial agent based models

In this Thesis, I mostly use spatial agent-based models, where n individuals (agents) move around in a two- or three-dimensional continuous space, and interact with the other agents, usually only those which are close to them. There is an issue of computational efficiency here, as at every time step a agent must decide which other agents to interact with, i.e. find which agents are its 'neighbours' for the purposes of the simulation. If done naively, this is an $\mathcal{O}(n^2)$ operation as it requires going through every pair of agents and calculating their distance from each other, and would become prohibitively slow even for a few thousand agents. There are, however, many ways around this problem, which has received extensive attention as it also frequently occurs in molecular dynamics simulations of atoms and molecules [70].

One such technique is the neighbour list or Verlet list [70, 84]. This works as follows. Say the agents only interact with agents a maximum distance R from them. In the neighbour list method, we introduce a second radius $R_v > R$. Initially, we calculate all the agents which are within a distance R_v of each agent, and put these in a list associated with each agent (this is still an $\mathcal{O}(n^2)$ operation). However, the list only needs to be updated if any of the agents have moved a distance greater than $R_v - R$, since this is the only way any agent not previously in the list of a agent could have entered its interaction radius, so this does not have to be done every time step. When the interactions are calculated, we just go through each agent's list, an operation which only requires $\mathcal{O}(n)$ calculations. By optimizing the distance R_v, we can gain significantly in efficiency.

A second technique is the 'cell list' [70, 85]. In this method the simulation box is split into boxes of size R_c, equal to or slightly bigger than the cutoff radius R. Each time step, every agent is assigned a box, and a list of the cells in each box is kept. For each agent, only agents in the same box or a neighbouring box are considered. The number of computations required thus scales as n times the number of boxes in the simulation. The efficiency of this algorithm can be further improved by checking whether a cell has moved out of a box into a new one at every time step, and updating the lists appropriately if it has. This removes the need to completely re-fill the box lists at every time step. To do this efficiently, it is necessary to keep an array `where_is[]` which contains for each agent its position within the list of the box it is in. So, for example, say that box 7

contains agents 2, 6, 9 and 23: `cell_list[7] = {2,6,9,23}`. Agent 9 has array index 3, so `where_is[9]=3`. The agent can then be quickly taken out of the box without having to search through the list for it.

2.3 Analytical methods

2.3.1 Hydrodynamics and the Boltzmann equation

Often, we will want to describe the dynamics of a collection of particles on large scales. The obvious way to do this is by a coarse-grained description in terms of fields such as the density and velocity of particles, which can vary in space: $\rho(\mathbf{x}), \mathbf{v}(\mathbf{x})$, and so on. The aim is to derive equations describing the dynamics of these fields. One way to do this is phenomenologically by appeal to the symmetries of the system, as is done in the Landau theory of phase transitions [86]. The classic example is that of the Ising model of interacting spins on a lattice, see e.g. [8], pp. 151-159. If the local magnetization (the order paramter) of the system is given by $\psi(\mathbf{x})$, then close to the phase transition the free energy can be written as

$$F = \int d^D\mathbf{x} \left(a + b\psi^2 + c\psi^4 + \lambda(\nabla\psi)^2 + \mathcal{O}(\psi^6, \nabla\psi^4)\right), \tag{2.1}$$

where a, b, c, λ are phenomenological parameters and only terms allowed by symmetry are included. From this free energy, the dynamics of the field $\psi(\mathbf{x}, t)$ can be derived, although this procedure is not trivial. In particular, hydrodynamic equations must be derived for all conserved quantities in the system under question, see [8], Chapter 8. In a non-equilibrium system, this free energy formulation will not be valid, but similar arguments based on symmetries can be used to write down hydrodynamic equations, as in the Toner-Tu field equations of the Vicsek model described below [7].

An alternative route is to try and derive equations for coarse-grained fields directly from their microscopic interactions. The classic example of such an analysis is the procedure to derive the Navier-Stokes equations from the Boltzmann equation, see for example [87]. The Boltzmann equation is an equation describing the out-of-equilibrium behaviour of a classical gas. We consider a box containing N particles of mass m with positions $\mathbf{x}_i$ and momenta $\mathbf{p}_i$. The strategy

is to derive an equation for the dynamics of the quantity $f(\mathbf{x}, \mathbf{p}, t)$, the density of particles with momentum $\mathbf{p}$ at position $\mathbf{x}$ at time t. Using Liouville's equation, and under the 'molecular chaos' assumption that there are no correlations between particles' positions and momenta when they collide, it can be shown that

$$\left(\frac{\partial}{\partial t} + \frac{1}{m}\mathbf{p} \cdot \nabla_x\right) f(\mathbf{x}, \mathbf{p}, t) = \int d\mathbf{p}^{*'} d\mathbf{p}' d\mathbf{p}^{*'} \Phi(\mathbf{p}, \mathbf{p}^*; \mathbf{p}', \mathbf{p}^{*'})[f(\mathbf{x}, \mathbf{p}', t) f(\mathbf{x}, \mathbf{p}^{*'}, t) - f(\mathbf{x}, \mathbf{p}, t) f(\mathbf{x}, \mathbf{p}^*, t)] \tag{2.2}$$

where the term on the RHS describes collisions between particles; $\Phi(\mathbf{p}, \mathbf{p}^*; \mathbf{p}', \mathbf{p}^{*'})$ is the rate at which particles with momenta $\mathbf{p}, \mathbf{p}^*$ collide to give particles with momentum $\mathbf{p}', \mathbf{p}^{*'}$. These collisions are assumed to obey conservation of mass and momentum.

From this equation, some very important results can be derived, such as the fact that entropy will increase over time, and the fact that the velocities of particles follow a Boltzmann distribution at steady state. It can also be used to derive equations for the dynamics of coarse-grained fields of the gas which are moments of $f(\mathbf{x}, \mathbf{p}, t)$, quantities such as

$$\rho(\mathbf{x}, t) = \int d^3\mathbf{p} f(\mathbf{x}, \mathbf{p}, t) \tag{2.3}$$

$$\rho(\mathbf{x}, t)\mathbf{u}(\mathbf{x}, t) = \int d^3\mathbf{p}\mathbf{p} f(\mathbf{x}, \mathbf{p}, t) \tag{2.4}$$

where ρ is the density field and u the velocity field. By integrating Eq. 2.2 over the momentum, a hierarchy of equations for these moments can be derived. Since the equation for each moment will depend on higher moments, approximations must be used to close the system. This yields equations describing the conservation of mass and momentum in the gas – the Navier-Stokes equations for a compressible fluid – and for heat flow. Thus, it is possible to derive the equations describing mass and momentum flow in a classical gas starting directly from the microscopic interactions between particles. A similar procedure to this is used later in the Thesis to derive hydrodynamic equations for a Vicsek-like model, although the procedure is somewhat different as monentum is not conserved in such active matter models.

2.3.2 Linear stability analysis

Very often, we will derive systems of partial differential equations describing the systems we want to study. Important examples include the diffusion equation, which describes the motion of particles undergoing a random walk, and the Navier-Stokes equations of fluid dynamics (as can be derived for a classical gas using the method above). The full analytical solution of such equations is usually impossible (though numerical solution is often useful, see next section), so approximations need to be made. One very useful technique is to probe the stability of a steady state solution, that is, whether such a solution is stable to small fluctuations, or whether such fluctuations will grow exponentially; this is known as linear stability analysis. An instability often points to interesting behaviour, such as pattern formation. To demonstrate the method, I take the simple example of the Fisher equation [88], an equation combining diffusion and logistic growth used to describe growing populations:

$$\frac{\partial \phi}{\partial t} = D\nabla^2\phi + \alpha\phi(1 - \frac{\phi}{\phi_0}), \tag{2.5}$$

where $\phi(\mathbf{x}, t)$ is density of diffusing particles/organisms. There are two steady-state solutions of this equation: $\phi = 0$ and $\phi = \phi_0$. We now want to analyse whether these are stable. Starting with the solution $\phi = \phi_0$, we set $\phi(x, t) = \phi_0 + \delta\phi(x, t)$, where $\delta\phi$ is a small fluctuation. Putting this into Eq. 2.5 yields

$$\frac{\partial \delta\phi}{\partial t} = D\nabla^2\delta\phi + \alpha(\phi_0 + \delta\phi)(1 - \frac{\phi_0 + \delta\phi}{\phi_0}). \tag{2.6}$$

We now *linearize* by ignoring terms of order $\delta\phi^2$ or higher, yielding

$$\frac{\partial \delta\phi}{\partial t} = D\nabla^2\delta\phi - \alpha\delta\phi. \tag{2.7}$$

To analyze stability we assume a form $\delta\phi = \tilde{\phi}e^{i(\mathbf{k}\cdot\mathbf{x}-\omega t)}$. One can then derive a relation $\omega(\mathbf{k})$, known as the *dispersion relation*. If the imaginary part of ω is positive for any $\mathbf{k}$, then this corresponds to an exponentially increasing mode and the solution is unstable. Here we have

$$-i\omega\tilde{\phi} = -Dk^2\tilde{\phi} - \alpha\tilde{\phi}, \tag{2.8}$$

so $\Im[\omega(\mathbf{k})] = -Dk^2 - \alpha$. Provided that $D, \alpha > 0$, the solution is stable for all $\mathbf{k}$. Now consider the solution $\phi = 0$. We set $\phi(x,t) = \delta\phi(x,t)$, and the same procedure as above now yields

$$-i\omega\tilde{\phi} = -Dk^2\tilde{\phi} + \alpha\tilde{\phi}, \tag{2.9}$$

and therefore $\Im[\omega(\mathbf{k})] = -Dk^2 + \alpha$. This solution is unstable for small values of $k \leq \sqrt{\alpha/D}$, and therefore large wavelengths $\lambda \geq 2\pi\sqrt{D/\alpha}$. What in fact occurs in the Fisher equation if started from $\phi = 0$ is that any small fluctuation will lead ϕ to grow and increase to ϕ_0 locally, and the high density region will then spread outwards in a travelling wave.

2.4 Numerical solution of partial differential equations

Very often, we will find that we have a system of partial differential equations, such as diffusion or hydrodynamic equations, which it is not possible or useful to solve analytically. In these cases we need to use numerical algorithms. The space and time dimensions must both be discretized so that instead of continuous fields we have (in one dimension) $t_n = ndt$ and $x_j = jdx$ where dt and dx are the time and space steps (note that they are finite numbers, not infinitesimals here), and n and j are integers. $u(\mathbf{x}, t)$ then becomes u_j^n. The derivatives which appear in the equations then need to be approximated, so for example

$$\frac{\partial u}{\partial x} = \frac{u_j^{n+1} - u_j^n}{dx}. \tag{2.10}$$

These approximations will introduce errors, so the time and space steps need to be sufficiently small. An important concern is the 'numerical stability' of the algorithm – the approximations of the space derivatives can introduce spurious instabilities which will grow exponentially. Avoiding these is not as simple as choosing small enough values of dt and dx. The precise form used for the derivatives is very important. A common choice is to use 'centred difference':

$$\frac{\partial u}{\partial x} = \frac{u_{j+1}^n - u_{j-1}^n}{2dx}. \tag{2.11}$$

Using forward differencing (Eq. 2.10) for the time derivatives and centred differencing for the space dimension is known as forward-time-cented-space or FTCS, and works reasonably well for equations like the diffusion equation:

$$\frac{\partial u}{\partial x} = D\frac{\partial^2 u}{\partial x^2}. \tag{2.12}$$

In the FTCS scheme this becomes

$$\frac{u_j^{n+1} - u_j^{n-1}}{dt} = D\left[\frac{u_{j-1}^n + u_{j+1}^n - 2u_j^n}{dx^2}\right]. \tag{2.13}$$

To analyse numerical stability, we do a stability analysis similar to the linear stability analysis described above in section 2.3.2, but discretized (see e.g. [89]; this method of stability anlysis was originally developed by von Neumann [90]). We look for so-called *eigenmodes* of the system, given by

$$u_j^n = \xi^n e^{ijkdx}. \tag{2.14}$$

Each eigenmode is made of successive integer powers of ξ, so if the modulus of $\xi(k)$ is greater than 1 for any k, then this mode will grow exponentially and there is a numerical instability. Putting Eq. 2.14 into Eq. 2.13 yields

$$\xi(k) = 1 - \frac{4Ddt}{dx^2}\sin^2(\frac{kdx}{2}). \tag{2.15}$$

Therefore the solution is stable only if

$$\frac{2Ddt}{dx^2} \leq 1. \tag{2.16}$$

Therefore, to increase the time step it is necessary to decrease the spatial step, and so simulating large length scales will be slow. To further improve stability, allowing one to use larger dt for the same dx, it is possible to use centred differencing for the time derivative as well, however this is more complicated as the expression for the derivative will involve u_i^{t+1}, which is unknown; a linear system of equations must be solved to find all the u_i^{t+1}. For our purposes the FTCS scheme will generally be sufficient.

It is also worth noting that for *advective* equations such as

$$\frac{\partial u}{\partial x} = v\frac{\partial u}{\partial x} \tag{2.17}$$

the FTCS scheme is always numerically unstable and more complex methods must be used to ensure stability [89], pp.1031-1043. This makes such equations (with advection but not diffusion terms) more difficult to deal with.

2.5 The Vicsek model

In this section I describe in detail the Vicsek model, an archetypal model of active matter, which I develop an extension of in Chapter 3, and which helps to illustrate the type of modelling done throughout this Thesis.

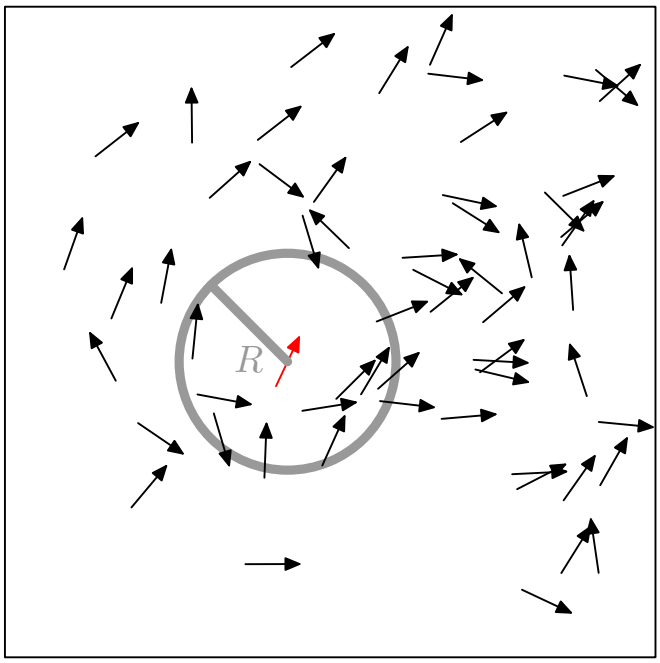

Figure 2.1: Schematic of the Vicsek model. Each time step, the red agent sets its direction of motion equal to the vectorial average of the directions of all the agents within the grey circle, with some noise added, and all other agents do the same.

The Vicsek model is an agent-based model consisting of a collection of particles in two dimensions, which all move with a constant velocity, v_0. At each time step, particles change the direction of their velocity, setting it to the local average

direction, calculated by vector addition of the velocities of all particles within a radius R, see Fig. 2.1. There is also noise: particles do not follow the average velocity exactly, but add a noise term as well. In their original paper [5], Vicsek et al. modelled the system computationally, and observed a dynamical phase transition between a disordered state and a polar ordered flocking state, at a critical strength of the noise (see Figure 2.2). They originally claimed that the transition was continuous, but this was disputed by Chaté et al. [10], who claimed that it was discontinuous (first order). There has subsequently been much controversy on the issue [12, 91, 92, 93]. It was observed [15] that the model is quite sensitive to details in its implementation, such as order in which the steps (average calculation, velocity update, moving), and in particular the nature of the noise. Two ways of implementing the noise are common: 'angular noise', where the noise is added on to the average,

$$\theta_i(t) = \arg\left[\frac{1}{N}\sum_{j\in R}\hat{\mathbf{v}}_j(t)\right] + \xi(t) \tag{2.18}$$

where the sum is over all N particles j within a radius R of particle i and $\xi(t)$ is a uniformly distributed noise between $-\eta$ and η, η being the parameter governing the noise strength. Another method is 'vectorial noise', where the noise is added to each direction vector, the idea being that the particles cannot determine each others' velocities exactly:

$$\theta_i(t) = \arg\left[\frac{1}{N}\sum_{j\in R}(\hat{\mathbf{v}}_j(t) + \eta\hat{\mathbf{e}}_j)\right] \tag{2.19}$$

where $\hat{\mathbf{e}}_j$ are random, independent, uniformly distributed unit vectors. These differences in implementation appear sometimes to affect the order of the flocking transition [15].

As well as agent-based simulations, there have been many analytical studies of the Vicsek model and similar flocking models. Among the first were Toner and Tu [7], who derived phenomenological hydrodynamic equations based on symmetries for a collection of self-propelled particles with alignment interaction, such as the Vicsek model, in terms of two hydrodynamic fields: the density of particles, ρ, and the local average velocity, $\mathbf{v}$. These equations are somewhat similar to the

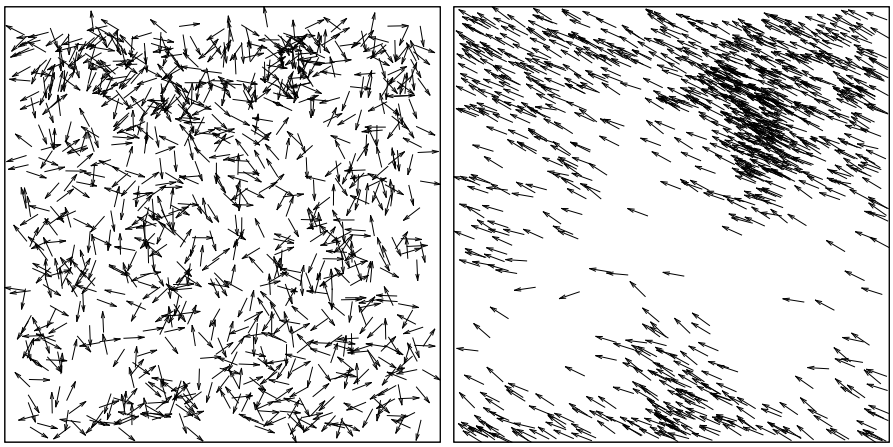

Figure 2.2: Snapshots from the Vicsek model for N=1000 particles; size L=10, showing the disordered phase at high noise (left, $\eta = 10$) and the ordered, 'flocking' phase at low noise (right, $\eta = 1$).

Navier-Stokes equations for a normal, equilibrium fluid, but have extra terms due to the lack of Galilean invariance, and can develop a spontaneous velocity. They are as follows:

$$\frac{\partial \rho}{\partial t} + \nabla \cdot (\rho \mathbf{v}) = 0 \tag{2.20}$$

$$\begin{aligned} \frac{\partial \mathbf{v}}{\partial t} + \lambda_1(\mathbf{v}\cdot\nabla)\mathbf{v} + \lambda_2(\nabla\cdot\mathbf{v})\mathbf{v} + \lambda_3\nabla(v^2) = \alpha\mathbf{v} - \beta v^2\mathbf{v} - \nabla P(\rho) \\ + D_B\nabla(\nabla\cdot\mathbf{v}) + D_T\nabla^2\mathbf{v} + D_2(\mathbf{v}\cdot\nabla)^2\mathbf{v} \end{aligned} \tag{2.21}$$

λ_i, D_i, α and β are phenomenological parameters, and $P(\rho)$ is a pressure-like term which tends to resist density gradients. Toner and Tu showed that the system exhibits true long-ranged order in two dimensions, which is surprising as in equilibrium thermodynamics there are no phase transitions with broken symmetries in systems with short-ranged interactions in two dimensions – the Mermin-Wagner theorem [8]. The theorem is not violated, however, as the system is not in equilibrium. Such flocking models can be viewed as non-equilibrium analogues of the XY model of a ferromagnet, in which two-dimensional spins tend to align due to magnetic interactions. The XY model has no ordered phase, but the motion of the particles in flocking models allows them to exert a wider influence on each other, allowing the order to be maintained against fluctuations. They also showed that the system exhibits propagative sound

waves and 'giant number fluctuations' (GNFs), density fluctuations which diverge and long wavelength. These effects have been observed in simulations of the Vicsek model, with the GNFs easily visible in a snapshot (Fig. 2.2) – the density fluctuations are clearly much larger than in an equilibrium fluid.

More recently, others [16, 28] have derived hydrodynamic equations for various flocking models, including, recently, the Vicsek model itself [94], from a microscopic description, allowing values for the parameters to be obtained. These derivations rely on various approximations, and as such are generally not valid deep in the flocking phase. The equations obtained are consistent with the Toner-Tu equations.

Another interesting emergent feature of flocking models is an instability of the flocking state which leads to the formation of travelling high-density bands, with the particles travelling perpendicular to the band direction. The instability is apparent from the linear stability analysis of the hydrodynamic equations, and the bands have been observed in agent-based simulations and in numerical solutions of the hydrodynamic equations [12, 13, 16]. The bands occur when the noise strength is not too far below the critical noise for the flocking transition. It seems that these bands are the reason the the transition is discontinuous [12], which would make sense as they can cause phase coexistence, with an ordered phase inside the bands and disorder outside them (phase coexistence is usually associated with a first order transition). Interestingly, the bands do not appear in a version of the model where the interaction between the agents is topological rather than metric (they interact with a fixed number of neighbours irrespective of distance) [95, 96]. In this case the transition is therefore continuous.

The Vicsek model is a good example of a system of interacting particles out of equilibrium which, given some very simple rules governing their interactions, exhibits a wide range of interesting behaviours, which have been studied in great detail since the model was first proposed twenty years ago. In the next chapter I will discuss my work on a variation of the model, where a new interaction (density-dependent speed) is introduced, leading to new pattern-formation effects.

Chapter 3

Self-propelled particles with variable motility

3.1 Introduction and motivation

In this chapter I introduce a variant of a Vicsek-like flocking model whereby the propulsion speed of the particles is not constant but rather depends on the local density of particles. Our motivation in doing this is to model pattern formation effects observed in bacterial colonies in the laboratory [69], in particular arrays of spots and rings (see Fig. 3.1) which are understood to arise from chemotactic interactions (i.e. quorum sensing) between the bacteria: the cells emit a chemoattractant, which tends to bias the run-and-tumble motion of other cells such that they move up the concentration gradient of the chemical. The bacteria bias their random walk by tumbling less often when they are moving up a concentration gradient of nutrient, essentially increasing their speed in this direction. In [97] it was shown that such chemotactic interactions can lead to a phase separation into high- and low-density domains of cells in space. In [98], this idea was used to model the formation of the aforementioned patterns. Essentially, the chemotactic dynamics leads to an effective dependence of the motility of the cells on the local density of cells, $v(\rho)$, and therefore their diffusion constant also depends on ρ, $D(\rho) \sim v(\rho)^2$. This dependence leads to a drift term which is proportional to the velocity gradient [98, 99], reflecting the fact that particles tend to accumulate where they go more slowly. This means that the equation

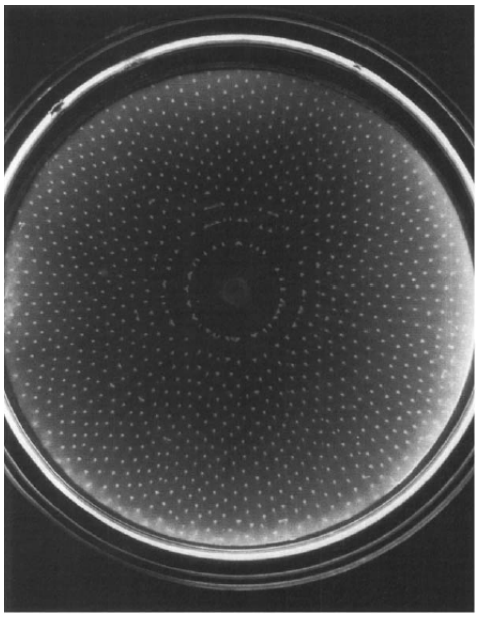

Figure 3.1: Pattern formed by *E. coli* in soft agar, showing an ordered array of spots due to the autoaggregation of the cells. Reproduced from [63]

describing the diffusion of the particles is now

$$\frac{\partial \rho}{\partial t} = \nabla \cdot [D_{eff}(\rho) \nabla \rho], \tag{3.1}$$

where $D_{eff}(\rho)$ is an effective diffusion constant including the drift effect, and is given by

$$D_{eff}(\rho) = D(\rho) + \rho D'(\rho)/2. \tag{3.2}$$

Note that if $D'(\rho)$ is a function that decreases significantly quickly with ρ, this effective diffusion constant 3.2 can become *negative*, leading to an instability. Starting from a uniform density, this instability leads to the formation of an array of high-density spots, which then coarsen into a single high-density region over time. In [98], it was shown that if birth and death of cells is added to this model, via a logisitic growth term, the spot pattern can be stabilized as cells continually die in the high density regions and proliferate in the low density regions. Starting from a single inoculum and allowing this to spread outwards, the system first forms rings, which then break up into ordered arrays of spots, in a similar manner to what is observed experimentally.

While the above models took the density-dependence of motility to be due to chemotactic effects, they are more generally applicable. Many interactions between agents might cause their effective motility to be a decreasing function of local density, for example steric repulsion between agents, where crowding will inhibit the ability to move. Models of self propelled particles with steric repulsion have shown interesting pattern formation effects, such as the formation of clusters and lanes [28, 29]. In flocks of macroscopic animals, it is easy to imagine that animals might have to slow down in high-density conditions to avoid collisions, leading to a similar effect. By using a very coarse-grained description of these interactions via a density dependent motility $v(\rho)$, we aim for a generic description of such systems. Below, I show the results of a model (active particles with density-dependent motility; we do not consider growth) combining this effect with an alignment (flocking) interaction. Flocking, or alignment, interactions are also known to be important in colonies of motile bacteria under some circumstances [100, 101, 102], since steric repulsion between the cells will tend to align them when they collide; we were interested in how these two effects might combine in interesting ways.

3.2 Model

We use a model of cells with a polar alignment interaction which is slightly different from the Viscek model. The Vicsek model is rather unusual in statistical physics terms as it includes many-body interactions: at each time step each cell takes an average of the orientations of all its neighbours. This makes a macroscopic, hydrodynamic description of the model rather difficult. We therefore modify the dynamics such that the interactions are pairwise, with each cell essentially feeling an aligment force from each of its neighbours. In 2D the position r_i and direction, identified by an angle θ_i (or a vector $\mathbf{e}_{\theta_i}$), of the ith particle evolves according to

$$\dot{r}_i = v\,\mathbf{e}_{\theta_i};\ \dot{\theta}_i = \gamma \sum_j F(\theta_j - \theta_i, r_j - r_i) + \sqrt{2\epsilon}\tilde{\eta}_i(t) \tag{3.3}$$

where γ and ϵ are parameters describing the strength of alignment and fluctuations respectively, and $\tilde{\eta}(t)$ is Gaussian white noise with zero mean and unit

variance. F controls the alignment interactions between the spins. For simplicity, we choose

$$F(\theta, r) = \sin(\theta)/\pi R^2 \tag{3.4}$$

if $|r| < R$ and 0 otherwise, though its precise shape does not dramatically affect the physics. As in the Vicsek models, the aligning interactions are only computed between particles up to a distance R apart. In the $v \to 0$ limit, our model is an off-lattice analogue of the XY model for a ferromagnet, hence we call it the *flying XY model*. Last, a density-dependent velocity is introduced in the model by stipulating that v depends on the number of particles n within a given radius R_n. Ordinarily, we take a form where the speed decreases with increasing density, $v(n) = v_0 e^{-\lambda n} + v_1$, where $v_0 \gg v_1 > 0$ are the dilute and crowded limiting velocities respectively, and $\lambda > 0$ controls the decay of the motility decreases with increasing density. This decrease in speed with density could, for example, represent steric interactions or chemotactic effects. We take $v_1 > 0$ as it is known that $v_1 = 0$ leads to pathological behaviour [97]. Note, however, that much of the analysis below is done for general $v(n)$. Hereupon we restrict to $R_n = R$ for simplicity.

As in the Vicsek model, simulations are performed in a box of side L with periodic boundary conditions, containing N agents. The dynamics 3.3 for each particle are calculated using a simple Euler method, with time step $dt = 0.01$. This time step needs to be small enough that the amount an agent changes its orientation in a single time step is much less than 2π. For computational efficiency a 'cell list' method, as described in Chapter 2, is used, whereby the simulation box is split into boxes of side R, and a list of cells in each box is maintained in order to determine which cells are neighbours. Simulations were started with the particles at random positions within the simulation box and with random orientations. To measure the stationary properties of the system, it is necessary to make sure the system reaches a steady state. We found that allowing the simulation to run for 10^5 time steps was sufficient. Quantities were then averaged over a further 10^4 time steps.

Fistly, we need to check that our model displays the same phase transition to a flocking state as the Vicsek model, ignoring the density-dependence part. Fig. 3.2 shows the order parameter $< v >= (1/N) \sum_i \mathbf{v}_i$ as the noise parameter ϵ is varied. As expected, there is a clear non-equilibrium phase transition from

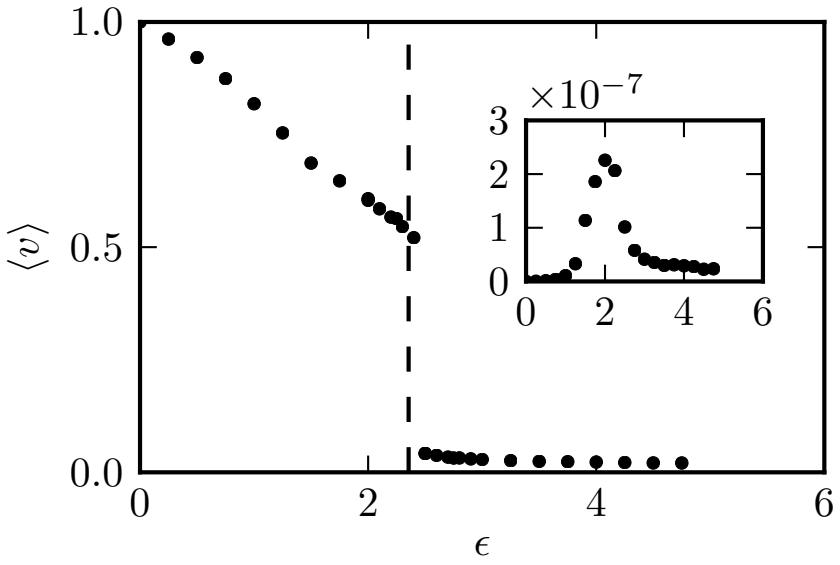

Figure 3.2: Orientational order parameter $< v >$ as a function of noise, for $\lambda = 0$. Other parameter values are $N = 3000$, $L = 10$, $\gamma = 0.16$, $v_0 = 2$ and $v_1 = 0$ Inset: temporal fluctuations in the order parameter, $< \Delta v^2 >_t$. The phase boundary was taken to be the peak in the fluctuations.

a disordered to a flocking state as the noise is decreased. The transition appears to be discontinuous. This would make sense if the banding instability discussed above in Section 2.5 does cause a discontinuous phase transition, as this instability is evident in our simulations, see Fig. 3.3, pattern (b), however we are not concerned with the nature of this transition here. In the next section I describe the results of our model when the density-dependent motility effect is turned on.

3.3 Results

The combination of the Vicsek-like alignment interaction and the self-trapping mechanism leads to novel pattern formation behaviour. Figure 3.3 shows a phase diagram of the system, with snapshots from the various different regimes. Figures 3.4 and 3.2 shows plots of the order parameter, demonstrating how the phase boundaries were determined. If only the self-trapping interaction is present, the particles phase-separate into high-density clumps which coarsen over time. If only alignment is present, the standard behaviour of the Vicsek

model is recovered, with giant density fluctuations [7] and travelling high-density waves [13, 16]. If both effects are present, depending on their relative strengths, the system either forms dynamic moving clumps which continually coalesce and break up, or forms a pattern of large stripes, with the particles moving parallel to the direction of the stripe, as opposed to the density waves in the standard Vicsek model, in which the direction of motion is perpendicular to the stripe. Fig. 3.5 shows snapshots of these patterns for a larger system size at the same density, for clarity and to demonstrate that they are not caused by finite size effects.

However, there are some caveats associated with this phase diagram. The number of particles $N = 3000$ is rather small, and there are significant finite size effects, especially with respect to the clumping transition, which occurs at larger λ for larger system sizes, see Fig. 3.8. Also, the dynamics of the clustered phase can be quite slow, so that 10^5 time steps may not be enough to equilibrate the system; in particular longer simulations show that the non-moving clusters tend to coarsen into a single cluster over time. Another point to note is that for larger system sizes the 'moving clump' phase d(i) does not display long-ranged orientational order since the clumps move in different directions, as in Fig. 3.5, and this situation appears to be stable.

For very high densities or values of λ, rather than phase separating into a few high-density clumps, the system can form a high density background with a few low-density voids (Fig. 3.6). Whether this happens will depend on how much of the system is taken up by the two phases at steady state.

3.4 Analytical theory

In order to gain insight into the pattern formation process, and clarify what properties of the model lead to the observed behaviour, we wanted to derive a coarse-grained, 'hydrodynamic' description of the system. Note that by 'hydrodynamic' I mean coarse-grained equations for the fields describing the system, not anything to do with actual fluid: the fluid through which cells swim is not being modelled here. Hydrodynamic equations for flocking models were first written down by Toner and Tu on phenomenological grounds, based on symmetries [7]. Equations for different models of flocking [16, 28] and for the original Vicsek model [94] have since been derived directly from the microscopic

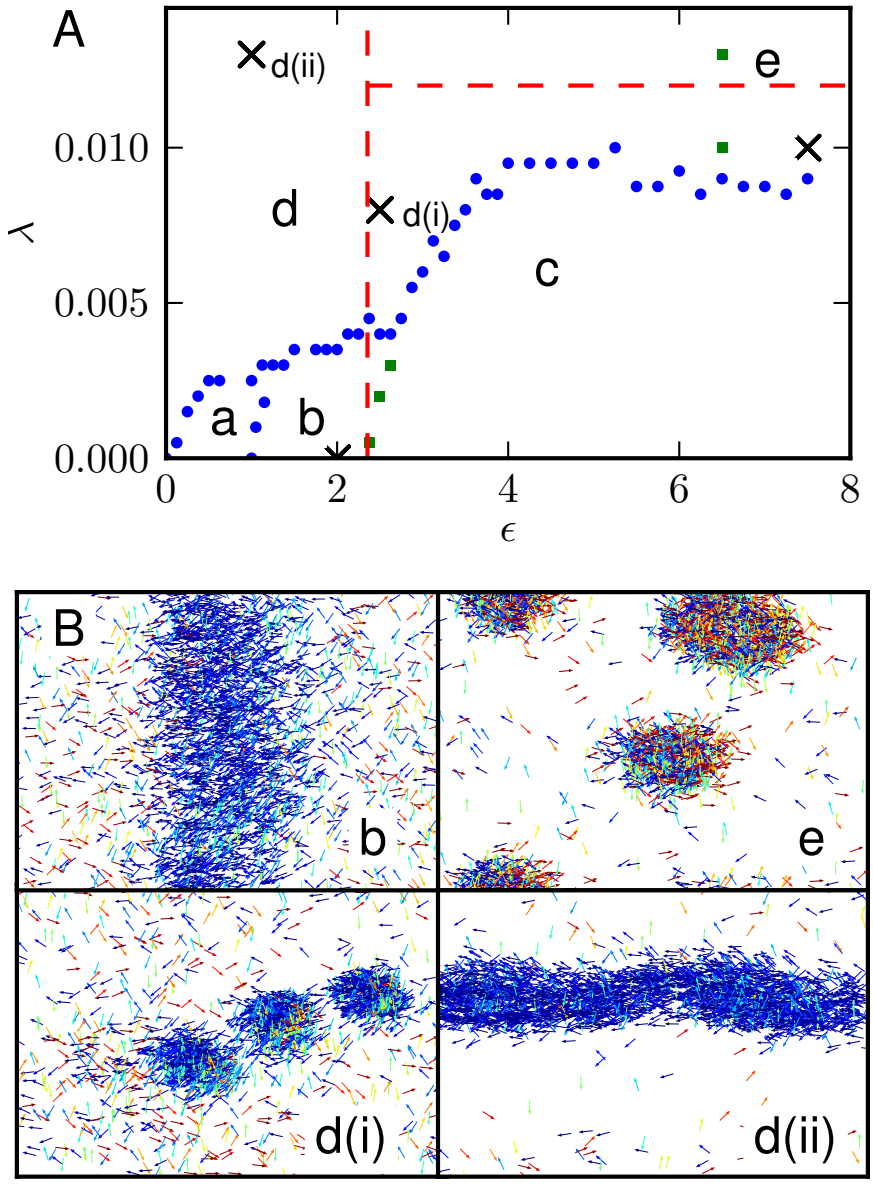

Figure 3.3: Phase behaviour when $v(n) = v_0 e^{-\lambda n} + v_1$. (A) Phase diagram in the (ϵ, λ) plane, for $N = 3000$, $L = 10$, $\gamma = 0.16$, $v_0 = 2$ and $v_1 = 0.1$. Blue filled circles on the phase boundary correspond to peaks in the variance of the particle density, while green squares separate states with zero mean orientation from states with nonzero mean orientation. At the boundary between phases (c) and (d) both order parameters change sharply, as the clustering effect sharply increases particle density within the clusters, leading to ordering. Horizontal and vertical red lines indicate linear instabilities towards clustering and ordering, respectively. (B) Snapshots of the stripy (b), aster (e), moving clumps (d(i)), lane (d(ii)) patterns. The crosses in A correspond to the snapshots in B. Particles are colour coded by direction, with blue horizontal and red vertical.

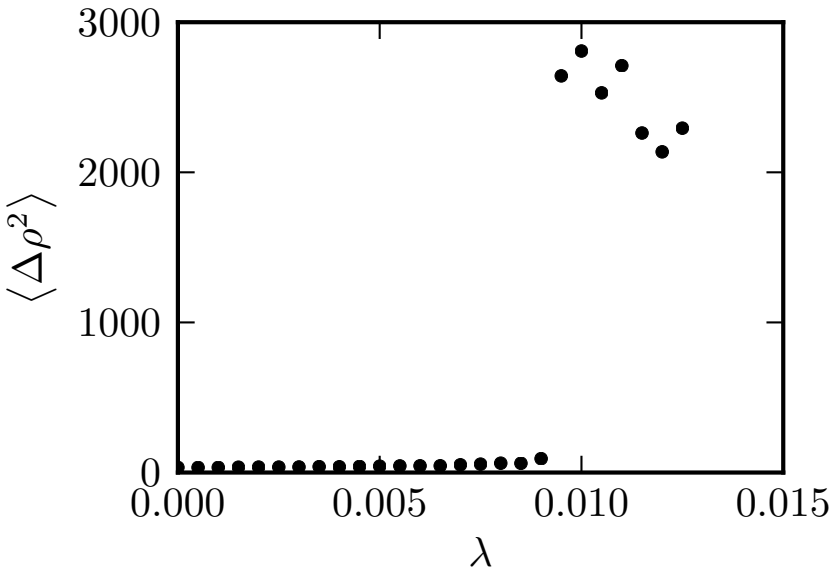

Figure 3.4: Spatial fluctuations in the local density of particles, $< \Delta\rho^2 >$ as a function of λ, for $\gamma = 0.16$, $\epsilon = 5.0$, $N = 3000$, $L = 10$, $v_0 = 2$ and $v_1 = 0.1$. The phase boundary was taken to be the point with the largest jump.

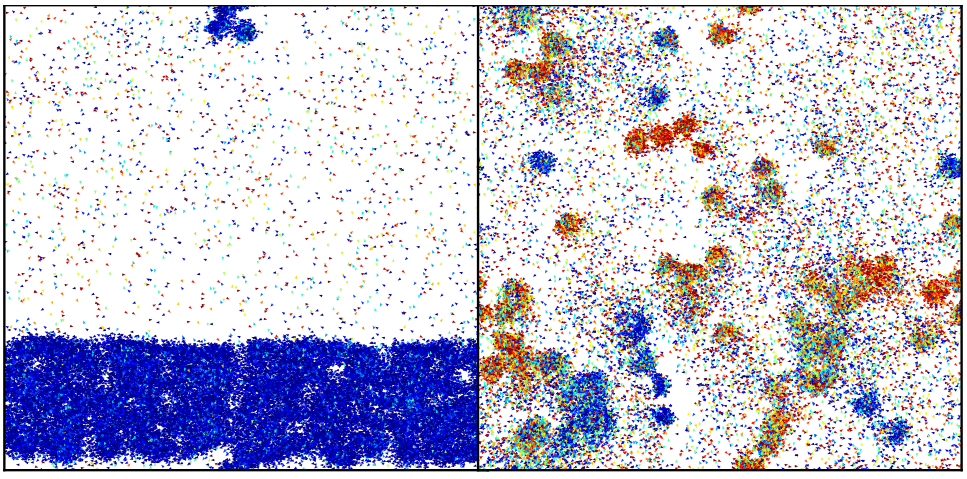

Figure 3.5: Inhomegeneous disordered phases, for the same parameters as in Fig. 3.3, but for a system 4 times larger, with the same particle density. Values of λ and ϵ are those marked with crosses in that figure, (ii) left and (i) right.

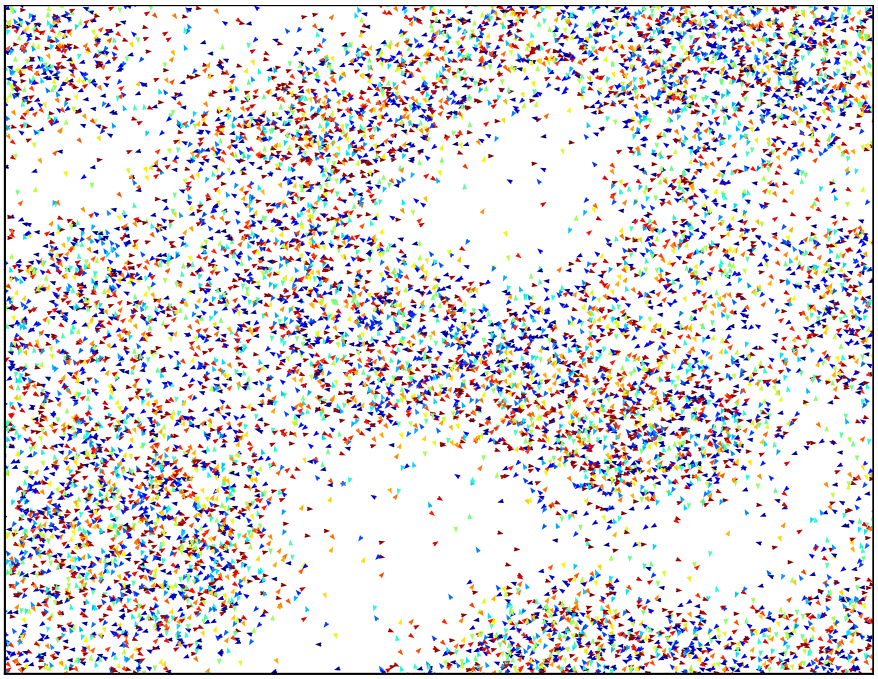

Figure 3.6: Snapshot of the simulation in a case where the system forms voids against a high-density background. Parameters as in figure 3.3, but with higher density, $N = 10000$; $\epsilon = 8.0$ and $\lambda = 0.01$.

models, and here we derive such equations for our model. On symmetry grounds, the hydrodynamic variables describing the system will be the density of particles, ρ, and the local polarization (direction) of the particles, $\mathbf{P}$. To do this we first derive a stochastic field equation for the quantity $f(\mathbf{r}, \theta) = \sum_{j=1}^{N} \delta(\mathbf{r}-\mathbf{r}_j)\delta(\theta-\theta_j)$, which is the density of particles at position $\mathbf{r}$ with angle θ. This method is similar to what was done in [16], and is equivalent to the Boltzmann equation describing an equilibrium fluid. The derivation of this Boltzmann-like equation is done in Appendix A; it is:

$$\begin{aligned}\dot{f}(\mathbf{r},\theta) = &-\nabla[f(\mathbf{r},\theta)\mathbf{v}] - \gamma\frac{\partial}{\partial\theta}\int d\mathbf{r}'d\theta' f(\mathbf{r},\theta)F(\theta-\theta',\mathbf{r}-\mathbf{r}')f(\mathbf{r}',\theta') \\ &+\epsilon\frac{\partial^2}{\partial\theta^2}f(\mathbf{r},\theta) - \frac{\partial}{\partial\theta}\sqrt{2\epsilon f(\mathbf{r},\theta)}\eta(\mathbf{r},\theta,t)]\end{aligned} \tag{3.5}$$

where $\eta(\mathbf{r}, \theta, t)$ is a Gaussian white noise of unit variance. Note that the velocity $\mathbf{v}$ appears inside the gradient in the first term in the RHS. This is crucial to the pattern formation due to the self trapping effect. We drop the noise

term and derive deterministic hydrodynamic equations; it could in principle be included to derive more realistic, noisy equations. Since we are looking at the large-scale, hydrodynamic description of the system, we take the limit where the interaction range R is very small, so that the spatial part of the function $F(\theta - \theta', \mathbf{r} - \mathbf{r}')$ can be replaced by a delta function, making the second term on the RHS $\gamma \frac{\partial}{\partial \theta} \int d\theta' f(\mathbf{r}, \theta) F(\theta - \theta') f(\mathbf{r}, \theta')$. We now Fourier transform Eq. 3.5 with respect to θ to get equations of motion for $f_k \equiv \int f e^{ik\theta} d\theta$. Using $2\pi f(\theta) = \sum_k f_k e^{-ik\theta}$ and $2\pi F(\theta) = \sum_k F_k e^{-ik\theta}$, we obtain a hierarchy of equations:

$$\begin{aligned} &\partial_t f_k + \frac{\partial}{\partial x} \frac{v f_{k+1} + v f_{k-1}}{2} + \frac{\partial}{\partial y} \frac{v f_{k+1} - v f_{k-1}}{2i} \\ &= -k^2 \epsilon f_k + i \frac{\gamma k}{2\pi} \sum_m f_m F_{-m} f_{k-m}, \end{aligned} \tag{3.6}$$

where all sums run from $-\infty$ to $+\infty$. We see that f_0 is simply the particle density field ρ. Since we are in two dimensions we can identify complex numbers with vectors: the real part of f_1 is $\int f \cos\theta d\theta$ and is therefore the x-component of the polarization order parameter $\mathbf{P}$, and similarly the imaginary part is the y-component. We easily recover the continuity equation in the case $k = 0$:

$$\partial_t f_0 = -\frac{\partial}{\partial x}(v f_i^x) - \frac{\partial}{\partial y}(v f_i^y) \tag{3.7}$$

$$\Rightarrow \partial_t \rho = -\nabla \cdot (v \rho \mathbf{P}). \tag{3.8}$$

In order to close this system of equations for $k > 0$, we need to make some approximations. In particular we assume that we are not too deeply in the ordered phase, so that $f(\theta)$ is almost homogeneous, and higher Fourier components can be neglected. We therefore neglect f_k for $k \geq 3$ and further assume that f_2 is a fast mode of the system, so that $\dot{f}_2 \simeq 0$. We also set the function $F(\theta) = \sin(\theta)$, so that $F_1 = -\frac{1}{2i}$, $F_{-1} = \frac{1}{2i}$ and all the other F_k are zero. The equations for $k = 1$ and 2 are then:

$$\partial_t f_1 = -\frac{1}{2}(\partial_x + i\partial_y)(v f_0) - \frac{1}{2}(\partial_x - i\partial_y)(v f_2) - \epsilon f_1 + \frac{1}{2}\gamma \rho f_1 - \frac{1}{2}\gamma f_1^* f_2 \tag{3.9}$$

$$\partial_t f_2 = -\frac{1}{2}(\partial_x + i\partial_y)(vf_1) - 4\epsilon f_2 + \gamma f_1^2 = 0. \tag{3.10}$$

Hence

$$f_2 = \frac{1}{4\epsilon}\left[\gamma f_1^2 - \frac{1}{2}(\partial_x + i\partial_y)(vf_1)\right] \tag{3.11}$$

whence

$$\begin{aligned}\partial_t f_1 =&(\frac{1}{2}\gamma\rho - \epsilon)f_1 - \frac{\gamma^2}{8\epsilon}|f_1^2|f_1 - \frac{1}{2}(\partial_x + i\partial_y)(vf_0) + \frac{\gamma}{16\epsilon}f_1^*(\partial_x + i\partial_y)(vf_1) - \\ &\frac{\gamma}{8\epsilon}(\partial_x - i\partial_y)(vf_1^2) + \frac{1}{16\epsilon}(\partial_x - i\partial_y)\left[v(\partial_x + i\partial_y)(vf_1)\right]\end{aligned} \tag{3.12}$$

Converting Eq. 3.12 into vector form is rather more complicated. The first three terms on the RHS are straightforward, but the terms involving complex conjugates of f_1 and the gradient operator must be expanded out in terms of their real and imaginary parts and compared to the expansions of various combinations of ∇ and $\mathbf{W} \equiv \rho\mathbf{P}$ in terms of their x- and y-components. Doing this yields the equivalences:

$$\begin{aligned}\nabla^*(vf_1^2) \equiv&(\mathbf{W}\cdot\nabla)(v\mathbf{W}) + \mathbf{W}(\nabla\cdot(v\mathbf{W})) + v(\mathbf{W}\cdot\nabla)\mathbf{W} \\ &+ v\mathbf{W}(\nabla\cdot\mathbf{W}) - \nabla(v|\mathbf{W}|^2)\end{aligned} \tag{3.13}$$

$$f^*\nabla(vf_1) \equiv (\mathbf{W}\cdot\nabla)(v\mathbf{W}) - \mathbf{W}(\nabla\cdot(v\mathbf{W})) + \nabla(v|\mathbf{W}|^2) - \frac{1}{2}v\nabla(|\mathbf{W}|^2) \tag{3.14}$$

$$\nabla^*\left[v\nabla(vf_1)\right] \equiv \partial_j(v\partial_j(v\mathbf{W})) + (\nabla v\cdot\nabla)(v\mathbf{W}) - (\nabla v)\nabla\cdot(v\mathbf{W}) \tag{3.15}$$

where the quantities on the LHS are complex numbers, those on the RHS the equivalent vectors, and * denotes conjugation. Applying these gives the hydrodynamic equation for the polarization field as:

$$\begin{aligned}&\partial_t\mathbf{W} + \frac{\gamma}{16\epsilon}(\mathbf{W}\cdot\nabla)(v\mathbf{W}) = (\frac{1}{2}\gamma\rho - \epsilon)\mathbf{W} - \frac{\gamma^2}{8\epsilon}W^2\mathbf{W} - \frac{1}{2}\nabla(v\rho) + \\ &\frac{3\gamma}{16\epsilon}\nabla(vW^2) - \frac{\gamma}{32\epsilon}v\nabla W^2 - \frac{3\gamma}{16\epsilon}\mathbf{W}\nabla\cdot(v\mathbf{W}) - \frac{\gamma}{8\epsilon}v\mathbf{W}(\nabla\cdot\mathbf{W}) - \frac{\gamma}{8\epsilon}v(\mathbf{W}\cdot\nabla)\mathbf{W} \\ &+ \frac{1}{16\epsilon}\left[(\nabla\cdot(v\nabla))(v\mathbf{W}) + (\nabla v\cdot\nabla)(v\mathbf{W}) - (\nabla v)\nabla\cdot(v\mathbf{W})\right]\end{aligned} \tag{3.16}$$

Equation 3.16 is certainly rather unwieldy, but some of the terms are relatively easily interpreted. The second term on the LHS describes advection of particles, and has a coefficient not equal to one as Galilean invariance does not apply.

The first two terms on the RHS describe the symmetry breaking which leads to spontaneous ordered motion in flocking models. The term $\frac{1}{2}\nabla(v\rho)$ is something like a pressure, in that it resists density gradients, and is crucial to the pattern formation here: if $v(\rho)$ is a sufficiently decreasing function it can become negative, leading to an instability in which the particles tend to clump together. The precise meaning of higher order terms is less immediately clear. The final three terms in square brackets are something akin to viscous terms in an equilibrium fluid, tending to oppose gradients in the velocity. In the rest of this section I analyse the hydrodynamic equations in more detail, performing linear stability analysis in order to elucidate which terms are important to the pattern formation, and presenting results on their numerical solution.

3.4.1 Linear stability analysis

In order to clarify the relationship between the hydrodynamic equations derived above and the pattern-forming behaviour of the model, we now perform linear stability analysis of Eqs. 3.8 and 3.16. For simplicity, I consider only cases when one or other of the effects in the model (alignment or self-trapping) is present. To analyse the effect of combining the two, I solve the equations numerically, in the next section.

If only the alignment interaction is present ($\lambda = 0$ and v is constant), we are in the standard situation for flocking models. Ignoring spatial gradients to start with, we have at steady state

$$\partial_t \mathbf{W} = (\frac{1}{2}\gamma\rho - \epsilon)\mathbf{W} - \frac{\gamma^2}{8\epsilon}W^2\mathbf{W} = 0. \tag{3.17}$$

Clearly, if the first term in Equation 3.17 is positive, the symmetry will be broken, leading to a non-zero $\mathbf{W}$ with $|\mathbf{W}| = W_0 = \sqrt{8\epsilon(\epsilon_c - \epsilon)/\gamma^2}$, as in the standard Landau theory of a continuous phase transition. This transition occurs when

$$\epsilon = \epsilon_c = \frac{1}{2}\gamma\rho. \tag{3.18}$$

As mentioned before, the flocking state is unstable to the formation of travelling density waves parallel to the flocking direction (phase (b) in Fig. 3.3). Linear stability analysis of the flocking state, done in Appendix B, shows that the

flocking state is unstable to formation of such a state (i.e. is unstable to density fluctuations parallel to the direction of flocking) if

$$\frac{7}{11}\epsilon_c < \epsilon < \epsilon_c \tag{3.19}$$

where $\epsilon_c = \frac{1}{2}\gamma\rho$ as before. This is in agreement with previous work on the hydrodynamics of flocking models [13, 16], in that the banding instability appears in the flocking phase when the noise is not too low.

I now consider what happens if we turn on the self-trapping interaction ($\lambda \neq 0$) in the disordered phase, $\epsilon > \epsilon_c$, and $\mathbf{W} = 0$. Performing linear stability analysis about this solution, setting $\mathbf{W} = \delta\mathbf{W}$ and $\rho = \rho_0 + \delta\rho$:

$$\partial_t \delta\rho = -\nabla \cdot (v\delta\mathbf{W}) \tag{3.20}$$

$$\partial_t \delta\mathbf{W} = -(\epsilon - \frac{1}{2}\gamma\rho)\delta\mathbf{W} - \frac{1}{2}\nabla(v\rho). \tag{3.21}$$

Since $\delta\mathbf{W}$ decays away quickly, we can take $\partial_t \delta\mathbf{W} = 0$, so that

$$\delta\mathbf{W} = -\frac{1}{\epsilon - \frac{1}{2}\gamma\rho}\nabla(v\rho). \tag{3.22}$$

Putting Eq. 3.22 in Eq. 3.21 then yields

$$\partial_t \delta\rho = \nabla \cdot \left[\frac{v}{2\epsilon - \gamma\rho}\nabla(v\rho)\right] = \frac{v(\rho_0)}{2\epsilon - \gamma\rho_0}\left(\rho_0 v'(\rho_0) + v(\rho_0)\right)\nabla^2\delta\rho \tag{3.23}$$

We have thus eliminated $\mathbf{W}$ to obtain an equation for the density. There is a negative diffusion constant, and therefore a clumping instability, if

$$\rho_0 v'(\rho_0) + v(\rho_0) < 0, \tag{3.24}$$

which is the same result derived in [98] for diffusing particles with density-dependent velocities. Taking $v(\rho) = v_0 e^{-\lambda\rho}$, we have

$$\lambda_c = \frac{1}{\rho_0}. \tag{3.25}$$

Fig. 3.7 shows results from the simulations of the positions of the phase transition to the flocking state and to the self-trapped state when these effects are considered

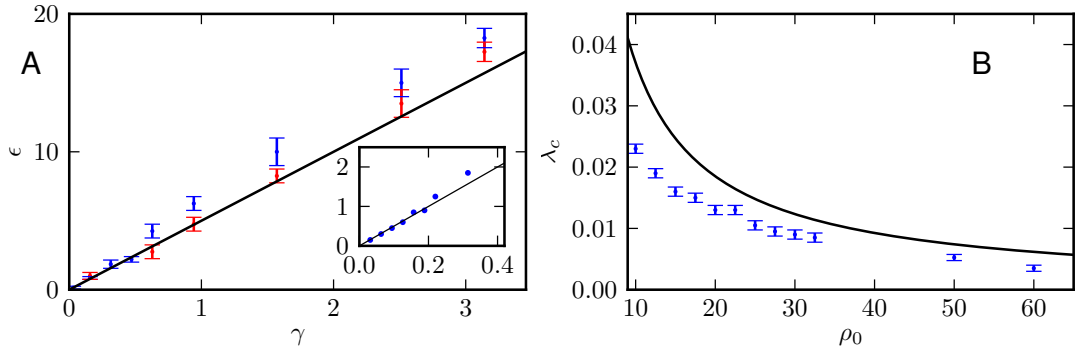

Figure 3.7: (A) Phase boundary for the flying XY model when $\lambda = 0$, showing the critical value of ϵ as a function of γ. Blue points for $v = 2.0$, red for $v = 0.5$; $v_1 = 0$ in both cases. Inset: data for $v = 2.0$ for smaller values of γ. The line is the theoretical result from the hydrodynamic equations, $\epsilon_c = \frac{1}{2}\gamma\rho$. (B) Phase boundary of the self-trapping/stationary clump phase for $\epsilon = 5.0$, $\gamma = 0.16$, $v_1 = 0.1$. The line is the theoretical result $\lambda_c = 1/\rho_0$. In all cases $L = 10$ and $N = 1000$.

separately, showing good agreement with the above results. Note that the transition to the clumpy state in simulations consistently happens for a smaller value of λ than predicted from the above (this is also visible in Fig. 3.3, where the red dotted line represents the predicted instability). This may be because fluctuations in the density can take the density above the critical value, in a similar way to nucleated phase separation in an equilibrium fluid.

Fig. 3.8 shows the two transitions for different system sizes, to show the effects of finite system size. Note that the transition line for the clumping transition at high noise moves closer to the predicted value for small system sizes, perhaps because fluctuations that cause nucleation are less likely in a smaller system. For the flocking transition, the boundary does not depend very much on system size, and becomes sharper for larger systems as expected.

3.4.2 Numerical solution

In order to go beyond the above simple linear stability analysis and account for the effect of the non-linear terms, and hence explore the range of patterns compatible with our hydrodynamic equations, we solved Eqs. (3.8) and (3.16) numerically, using standard finite-difference methods for solving partial differential equations. The finite difference scheme used was simply the Euler method (see Chapter 2), combined with a predictor-corrector routine to improve stability. There are

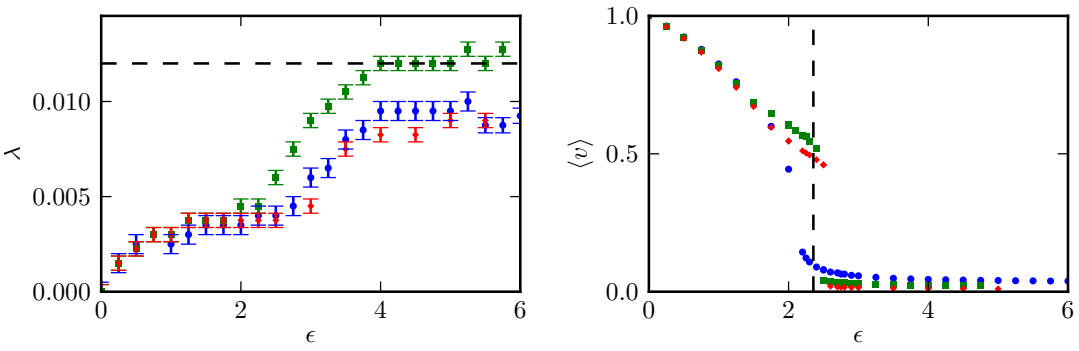

Figure 3.8: Left: phase boundary between homogeneous and inhomogeneous ('clumpy') phases, for 3 different system sizes, with the same particle density ρ. Green points, $N = 750$, $L = 5.0$; blue points $N = 3000$, $L = 10.0$; red points $N = 12000$, $L = 20.0$. The alignment parameter γ=0.05, as in Fig. 3.3. Dashed line is the theoretical prediction for the phase boundary at high noise, from linear stability analysis of the hydrodynamic equations. Right: order parameter as a function of noise for the same 3 system sizes at $\lambda = 0$, showing the order-disorder transition from the flocking state. Again, the dashed line shows the theoretical position of the transition from linear stability analysis.

various numerical stability problems associated with advective equations such as these, so to simplify the situation we added in a small diffusion term $D\nabla^2\rho$ on the right hand side of Eq. (3.8) (a similar strategy was used in [13]). The results of this show that all patterns observable in the microscopic simulations can be recovered in numerical solution of these equations: the fluctuating flocking state, travelling density waves, high-density 'lanes', static clusters and moving clumps. Fig. 3.9 shows snaphots of the $\lambda \neq 0$ patterns obtained from the numerical solution. These are compared with data from the agent-based (microscopic) simulations. To make the comparison clearer, the results from the microscopic simulations have been averaged over time and space, to give a coarse-grained, average description of the velocity field $\mathbf{W}(\mathbf{x})$, which is what is plotted for the numerical solution. Fig. 3.10 shows a larger image of the stripe pattern for a larger system size in the hydrodynamic equation solution, colour coded for the magnitude of the order parameter rather than the density to clearly show the ordering within the stripe.

One interesting feature is the nature of the coarse-grained field for the 'clumpy' pattern. The velocity field in these clumps is not zero, but points towards the centre of the clump – they can be seen as 'aster' patterns, like those seen in models of active gels. This can be understood by looking at the hydrodynamic

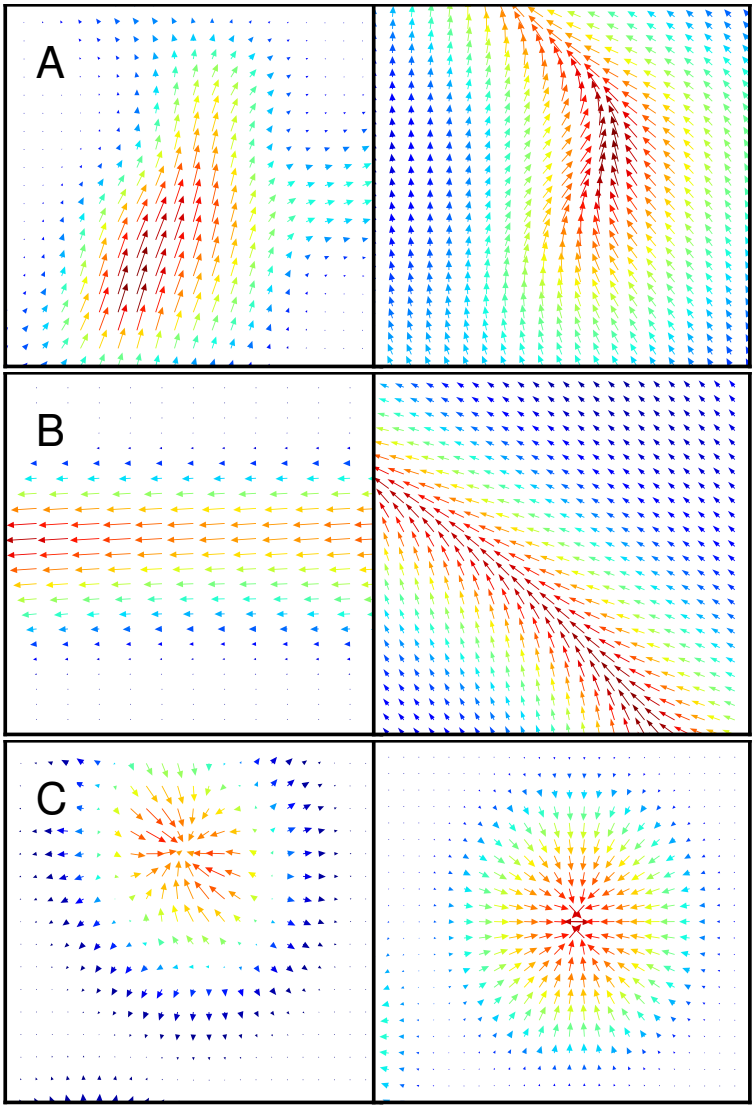

$\tilde{\lambda}$	0.75	1.5
$\tilde{v_1}$	0.05	0.09
$\tilde{\gamma}$	1.6	3.6
$\tilde{D}$	-	0.02

$\tilde{\lambda}$	1.2	1.5
$\tilde{v_1}$	0.05	0.12
$\tilde{\gamma}$	4.8	4.5
$\tilde{D}$	-	0.02

$\tilde{\lambda}$	0.94	1.5
$\tilde{v_1}$	0	0
$\tilde{\gamma}$	0.64	2.3
$\tilde{D}$	-	0.01

Figure 3.9: Patterns found for $\lambda \neq 0$ in the microscopic simulations (left column) and in the numerical solution of the hydrodynamic equations (right). Tables show dimensionless parameter values: $\tilde{\lambda} = \lambda\rho_0$, $\tilde{v_1} = v_1/v_0$, $\tilde{\gamma} = \gamma\rho_0/\epsilon$, $\tilde{D} = D\epsilon/v_0^2$. Arrows show the **W** field, colors the density (red: high; blue: low). In the right column, only a fraction of the simulated system is shown for clarity.

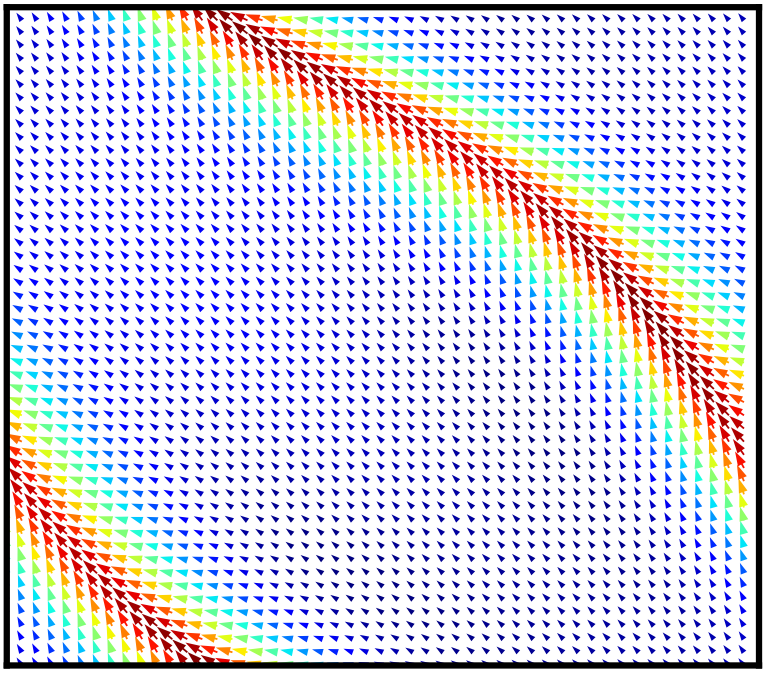

Figure 3.10: Parallel stripe pattern from numerical solution of the hydrodynamic equations. Parameters used are as in Fig. 3.9B, right. Here the colour scale shows the magnitude of the order parameter $\mathbf{W}$, and the full simulation box is shown.

equations in the limit of small $\mathbf{W}$ in the steady state. Eq. 3.16 reduces to

$$(\gamma\rho/2 - \epsilon)\mathbf{W} = \nabla(\rho v/2) \tag{3.26}$$

and therefore $\nabla(v\rho)$ thus acts as an ordering field for $\mathbf{W}$: the net flow is caused by gradients in $v\rho$ within the clusters. Note also that in the averaged image from the microscopic simulations, at the edge of the aster the field changes direction. Along the radius of an aster, the density increases towards the center whereas the velocity decreases. Their product can thus be non-monotonic, which makes $\mathbf{W}$ change direction.

3.5 Discussion and extensions

We have shown that a density-dependent motility in our flying XY model, a close relative of the Vicsek model, yields new patterns in suspensions of self-propelled particles. The derivation of hydrodynamic equations helped to identify the key

ingredient causing the pattern formation in the 'pressure term' $-\frac{1}{2}\nabla(v\rho)$: if $v(\rho)$ is sufficiently quickly decreasing with ρ, this term will encourage rather than oppose density gradients, leading to a self-trapping instability and the formation of new patterns. The patterns are not very sensitive to the precise form of $v(\rho)$; all that is required is that the condition 3.24 is met. For instance, steric hindrance results in velocities that typically decrease linearly with density [103] and would give similar instabilities. A recent work by Peruani et al. [104] studied a microscopic lattice variant of the Vicsek model, and also found asters and moving clumps, dubbed traffic jams and gliders. This is again naturally explained by our theory, as their origin there lies in the slowdown of particles due to crowding, which causes an effective 'pressure term' analogous to that in Eq. (3.16).

Recent experiments have also shown results similar to the patterns observed in our model, which may have a similar origin. For example, experiments performed on *in vitro* collections of active fibres moving on a carpet of molecular motors show collective behaviour effects as the collision of the fibres tends to align them. These experiments have exhibited moving high-density clusters of fibres [105], and high-density 'streaks' or bands in which the fibres move parallel to the band [106], amongst other patterns. A density-dependent motility, induced either by steric hindrance or by crosslinkers between actin fibers, may be the cause of these.

3.5.1 Alternative forms of the density dependence

Thus far we have mostly considered a particular form for the density dependence of the velocity, one that decreases exponentially with density. The above analysis is easily generalized to other forms of the dependence. Any decreasing function of density will exhibit very similar behaviour, with a clumping instability existing for high noise if $\rho_0 v'(\rho_0) + v(\rho_0) < 0$, as derived above in Section 3.4.1, with these clumps moving or forming lanes if the alignment interaction is strong. If the velocity is an increasing function of density, no such instability exists and the behaviour is not very interesting. However, we have observed some unexpected bahaviour in our simulations in the case where the function $v(\rho)$ has a peak. In particular, if it is peaked at or close to the initial density ρ_0, the system forms an array of small, stationary clumps, roughly in a hexagonal lattice, which do not coarsen over time as they do in the ordinary clumpy phase (Fig. 3.11). Note that there is no linear instability here as $v'(\rho_0) = 0$. The clumps have a size

which is of the order of the interaction radius R, so clearly this pattern depends crucially on the fact that there is such a finite radius in the system, an effect not so far included in our hydrodynamic equations. Qualitatively, the pattern is stable because the average density over the interaction radius in the region between the clumps is near the position of the peak in the velocity function, so particles move fast and these regions remain empty.

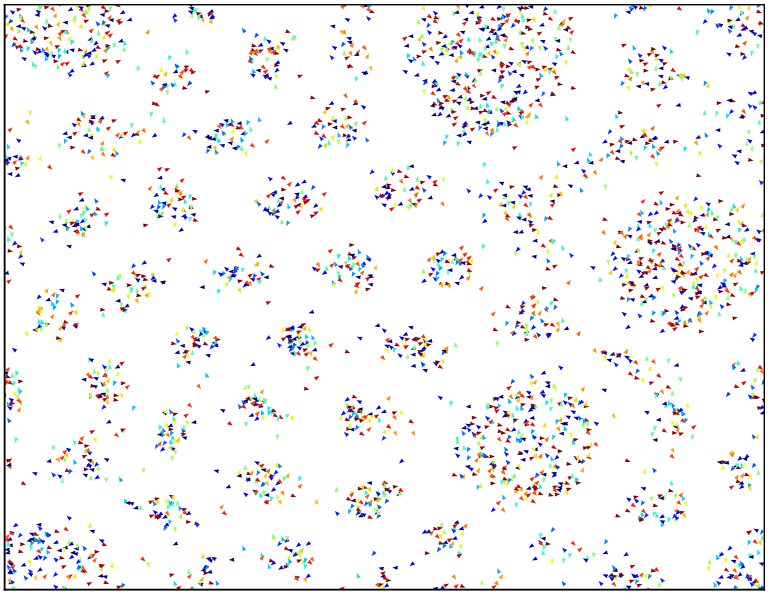

Figure 3.11: Snapshot of the system for $v(\rho) = v_0 e^{-(\rho-\rho_0)^2/\sigma^2}$, a Gaussian peaked around the initial density. Here $\rho_0 = 30.0$ and $\sigma^2 = 200$. $\gamma = 0.16$, $\epsilon = 5.0$, $N = 3000$, $L = 10$, $v_0 = 2$ and $v_1 = 0.1$.

3.6 Conlusions

In this chapter I have described a model of collective motion in self-propelled particles in which the propulsion speed of the particles depends on their local density. This dependence could be the result of signalling between agents (e.g. chemotaxis), or to crowding and steric hindrance, and was intended to be a model of motile bacterial cells in a dense colony, where both of these effects might be significant. I started by introducing a variation of the Vicsek model, which we term the *flying XY model*, where the interactions between agents are pairwise rather than many-body to simplify the mathematical treatment of the model, and showing that it displays behaviour broadly similar to the Vicsek model. I then

introduced a density-dependent motility to this model, by making the propulsion speed depend on the number of neighbours within a given radius.

Simulating the model demonstrated the formation of new patterns (coherently moving clusters and 'lanes' with particles moving along the direction of a high-density band), depending on the parameters of the model (degree of density-dependence of the speed, strength of alignment compared to noise, density). We also derived coarse-grained 'hydrodynamic' equations for the model, that is, partial differential equations describing the dynamics of coarse-grained density and velocity fields. Elementary linear stability analysis of these equations yielded predictions of the phase boundaries for transitions to the flocking state and to the self-trapping state which fit well with the results of the agent-based simulations, and by numerical solution we were able to show that they reproduce all the patterns seen in the simulations. These results are useful in understanding recent experimental work on active matter systems which exhibit collective behaviour, in particular collections of actin fibres and myosin molecular motors studied *in vitro* [105, 106].

Chapter 4

Mechanical models of biofilm growth

4.1 Introduction

4.1.1 Biofilms

Bacteria are often pictured as living as individuals, swimming around in a fluid. Recently, however, it is increasingly being recognized that they very often live in dense multicellular communities with many other cells, interacting with them in various complex ways [47, 48, 53]. This 'multicellularity' can confer many advantages to the cells, such as increased antibiotic resistance and resilience to environmental changes [51, 55]. These colonies often grow on two-dimensional surfaces, where they are known as 'biofilms' (see Section 1.2). Biofilms are involved in a great number of diseases [50], cause problems – and have applications – in many industrial settings, and are perhaps one of the dominant ways in which bacteria live [57].

4.1.2 Pattern formation in colonies grown on agar paltes

Biofilms are also a fascinating example of an active matter system, whose behaviour is determined by the collective interactions of a great number of individuals. The activity in this case arises from the growth, death and migration of the cells. Biofilms are often very complex, with spatial structure, features such as nutrient and waste channels, and multiple species of microbes. Rather

than dealing with all of this complexity, it is interesting to study a very simple model system in order to see what features can emerge. A common experimental analogue of a biofilm is the growth of a colony of bacteria on agarose, a semi-solid material which is infused with nutrients necessary for the bacteria to grow. A colony can be started from a single cell, so will consist of only one strain. Even in this very simple situation, interesting pattern formation effects can be observed [58, 63, 98].

In the regime we are interested in here, the agarose is hard enough that the colony grows on top of it similarly to a biofilm, and the cells are not able to swim around within the medium. We do not consider any of the various interactions between cells, such as chemotaxis, which lead to many of the more complex patterns described in the above papers. When colonies are grown in the laboratory on such a hard agarose surface, there is a transition between a roughly circular colony, and a highly branched, fractal pattern [68, 62], see Fig. 4.1. The compact shape, seen at high nutrient concentrations, is similar to what is observed in the so-called 'Eden model' of growth processes [107]. This is a lattice model of a growing cluster (such a colony of cells) whereby at each time step an empty lattice site with an occupied neighbour becomes full. At long times, roughly round clusters are observed. It is believed that this model falls into the KPZ (Kardar-Parisi-Zhang) universality class of growth models [108, 109]. The branched shape, on the other hand, is similar to patterns observed in diffusion-limited aggregation (DLA) [110], a process whereby particles diffuse around outside of a growing cluster until they hit it, at which point they are frozen in place.

These observations have inspired a lot of theoretical work studying how such patterns might be formed, and what controls the transitions between them. These have mostly involved generalization of the Fisher equation, an equation combining diffusion and growth which is used to describe growing populations in many circumstances [88, 69]. In its basic form, the Fisher equation is given by

$$\frac{\partial \phi}{\partial t} = D\nabla^2\phi + \alpha\phi(1 - \frac{\phi}{\phi_0}) \tag{4.1}$$

where ϕ is the density of individuals (here cells), D is their diffusion constant, α describes their growth rate, and ϕ_0 is the 'carrying capacity', and represents the maximum density of organsisms which can be maintained (e.g. because because of limited resources). The solution to this equation is a travelling wave, with a

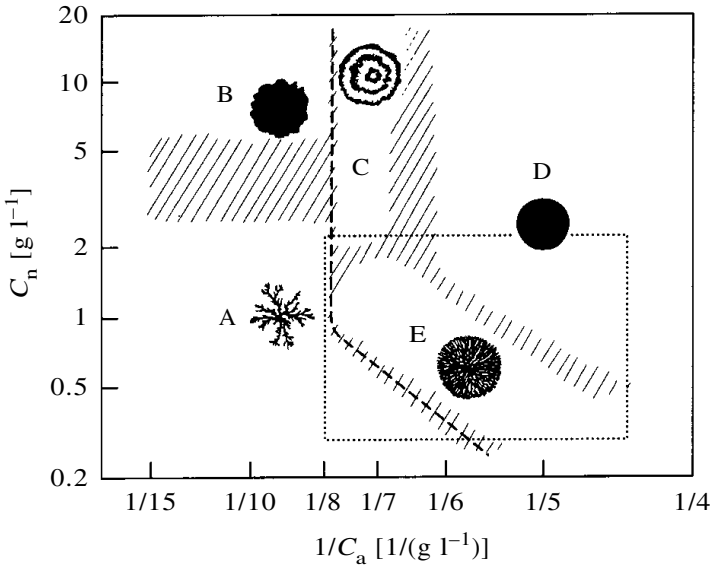

Figure 4.1: Reproduced from [68]. Diagram showing observed colony patterns of the rod-shaped bacterium *Bacillus subtilis* as a function of nutrient concentration C_n and agar concentration (which determines the solidity of the substrate) C_a. We are here concerned with the patterns A and B which occur on hard agar.

front of high density expanding outwards at a constant speed, with the density deep within the expanding front (far from the frontier) given by the carrying capacity ϕ_0. This is used as a model of a bacterial colony consisting of cells which swim around randomly (diffusion) and proliferate (growth). Generalizing this equation to include a description of the diffusion of nutrients in a bacterial colony, and effects such as density-dependence of the diffusion constant, various instabilities are found which can lead to pattern formation of the kind observed experimentally [58, 68, 69].

However, this model, which considers the bacteria as diffusing particles, is not very accurate in the case of biofilm growth, in which the cells are often not motile and move mostly by simply pushing each other out of the way as they grow. We aimed to study such colonies using a model where such mechanical pushing is the source of the expansion of the colony, using agent-based computer simulations, and a theory whereby the colony is treated as an expanding cellular 'fluid'. Doing this, we derive results which are quite different to those obtained using a Fisher-like theory, such as that a colony cannot expand at a constant speed unless the cells are compressed, and a different origin of the transition between dense and branched colonies, which in our theory is driven by the balance between

biomass growth and nutrient uptake. There do exist other agent-based, more mechanically-motivated models of biofilm growth (e.g. [61, 111, 112]), which have been used to develop detailed models of biofilm growth for industrial purposes, and to study issues such as cooperation and competition within and between biofilm species. However, these models generally treat the mechanical forces between cells in a schematic way; here we aim to model these physical forces in some detail, and find that they can be very important to colony growth.

4.2 Simulation model

4.2.1 Outline of the model

To model the growth of non-motile cells on a solid surface, we use a simple two-dimensional model whereby the cells are treated as rigid spherocylinders (or more accurately 'discorectangles' as they are two dimensional). The radius of the cells' end caps is given by $r_0 = 0.5\mu$m, their diameter $d = 2r_0$. This model is similar to that used in [113], which was used to study nematic ordering of cells in dense colonies. Each cell is described by two coordinates $\mathbf{r} = (x, y)$ and an angle ϕ which gives the orientation of the main axis. As the cells grow, they push against each other, interacting mechanically in accordance with the Hertzian theory of elastic contact [114], which describes the force felt between solid elastic bodies in contact with each other, i.e. we approximate the cells as being made of a homogeneous elastic material. The force between two rods is approximated as a force between two spheres placed at major axes of the two rods in such positions that their distance is minimal, but the spheres remain within the rods, see Fig. 4.2. If r is the distance between the centres of the spheres and $h = 1-r$ is the overlap in μm, then the force is assumed to be equal to $F = Ed^{1/2}h^{3/2}$ where E parametrizes the strength of the interaction and is proportional to the elastic modulus of the cells. To model the response of the cells to these forces, we assume that the dynamics is overdamped, and use the following equations to calculate the linear and angular velocity of the cell:

$$\dot{\mathbf{r}} = \frac{1}{\zeta\ell}\mathbf{F}; \tag{4.2}$$

$$\dot{\phi} = \frac{12}{\zeta\ell^3}\tau \tag{4.3}$$

where ζ is a constant describing the friction between the surface and the cell, and τ is the torque on a cell. These equations come from assuming that every infinitesimal section of the cell experiences a friction force with the surface proportional to its velocity. Note that this is a simplification: in reality the frictional force between the cell and the surface is likely to take a more complicated form due to effects such as static friction and adhesion with the surface. This frictional force is not currently well characterised experimentally. Generalizations of our model which use different forms of this friction force will be discussed later; simulations indicate that the details of this force do not make a large difference to the overall behaviour of colonies.

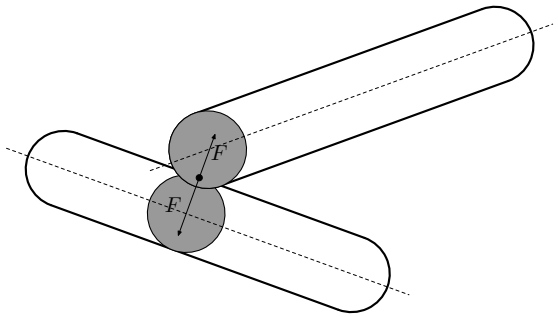

Figure 4.2: Diagram showing how the force between overlapping cells is calculated.

When a growing cell reaches a certain length ℓ_c, it will reproduce by dividing into two identical cells. This length is usually taken to be four times the cells' diameter d, similar to bacteria such as *E. coli*, but can be varied, for example it can be made smaller to make the cells more similar to yeast cells. The two daughter cells have the same orientation as the parent, with each receiving a small random perturbation to this angle to prevent the cells from growing in a straight line. So, if a simulation is started from a single cell, this cell will grow, then divide, then these cells which push each other apart before dividing again, leading at long times to a roughly circular, expanding colony. Fig. 4.3 shows such a colony after a few divisions, along with a snapshot of an experimental colony growing on an agar plate in the lab, of a similar size.

If this were allowed to continue, the colony would expand at an exponential rate for all times. Obviously this is not realistic, and in real life the growth will be limited, for example by diffusion of nutrients into the colony or by the build-up of waste products within the colony. We model this by including the dynamics

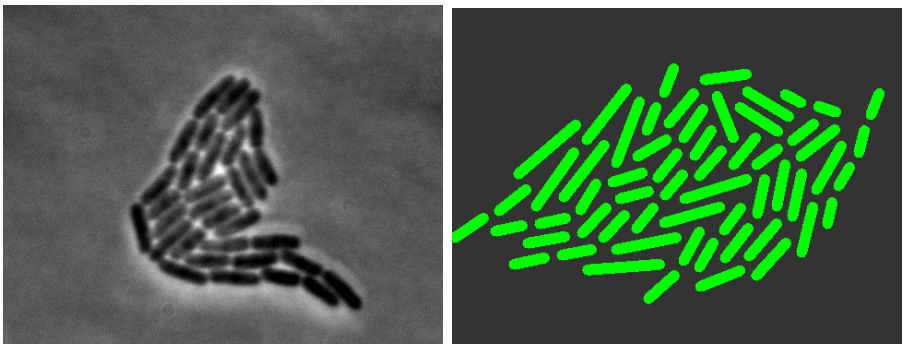

Figure 4.3: Top left: experimental image of *E. coli* growing on an agar plate in the laboratory (courtesy Dario dell'Arciprete). Top right: a snapshot from our simulation model showing a colony of a similar size.

of a limiting nutrient. The nutrient obeys the diffusion equation. The cells eat the nutrient in order to grow, so the growth rate of cells will depend on the concentration of this nutrient, and the nutrient will be depleted by the growth of the cells. The nutrient concentration $c(x, y)$ is governed by the diffusion equation with a sink:

$$\frac{\partial c}{\partial t} = D\left(\frac{\partial^2 c}{\partial x^2} + \frac{\partial^2 c}{\partial y^2}\right) - k\sum_i A_i f(c(x_i, y_i)) \tag{4.4}$$

where A_i is the area of cell in i square microns and x_i, y_i are its spatial coordinates. D is the diffusion constant of the nutrient, and k is parameter discribing how quickly cells deplete the nutrient. The function $f(c)$ is a monotonously increasing function of c. In most simulations, we assume that $f(c) = c/(1 + c)$ is a Monod function with half-saturation concentration equal to 1 (arbitrary units), but we have checked that other reasonable functions $f(c)$ (such as the linear one $f(c) = c$) lead to qualitatively identical behaviour. The length of cell i grows at a rate $\gamma_g A_i f(c(x_i, y_i))$ where γ_g is a parameter describing the cells' growth rate, and A_i is the area of cell i. Note that a cell's growth rate will therefore increase as it grows. The inclusion of the area here also ensures that colonies made up of cells of different aspect ratios will grow at the same rate, as γ_g is a growth rate per unit cellular area. The simulation is started with a uniform concentration of nutrient c_0, and the concentration is held constant at the boundaries of the simulation box. The nutrient limitation means that after a long time, there will be no nutrient in the middle of the colony, and the cells there will not be growing; cells only grow in a narrow layer at the edge of the colony leading to a colony

which expands linearly in time. This situation is what is observed experimentally [66, 115].

As well as starting from a single initial cell which grows into a roughly circular colony, we ran simulations in which we started with a line of cells, which grow into a flat front. In this case, periodic boundary conditions are used in the direction lateral to the front. This geometry is far more computationally efficient, as cells deep within the colony which are no longer growing can be discarded, allowing the simulation to be run in a frame comoving with the advancing front.

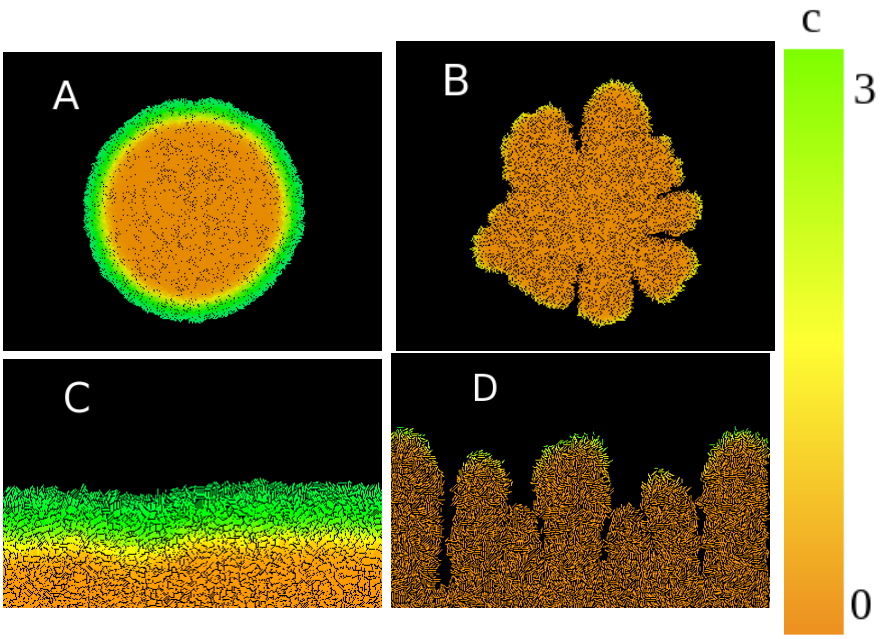

Figure 4.4: A-B: snapshots from the simulation of $N \sim 10^5$ cells. Colours correspond to the local nutrient concentration $c(\mathbf{r}, t)$, see the colourmap on the right. Only a thin layer of cells (green) grows appreciably. C-D: growth in a narrow, long strip. Parameter values are as in Table 4.1; in B and D the nutrient uptake rate k has been increased from 50 to 100 h^{-1}, causing the morphology of the colony to change.

4.2.2 Details of the simulation algorithm

In order to maximize efficiency, the simulation box is split into a grid of boxes of side length r_0, the cell diameter. This grid is kept as a three-dimensional array, with the first two arguments being the x- and y-postitions of the box, and the

third containing the label of a cell which occupies the box, if any. A separate grid is used to contain the concentration of nutrient at each point (the two grids can have diffrent lattice sizes). Each time step, the program loops through all the cells in the colony and adds the cell to each box which it enters (which will be many boxes for each cell). The forces between cells are then calculated. For each cell, every grid box which is a neighbour of a box occupied by the cell is checked to see if there is a different cell in it; if there is then the force between the two cells is calculated as described above. The x, y and angular (torque) components of this force are added to variables describing the total force on the cell. This procedure avoids the need for an $\mathcal{O}(n^2)$ loop through every pair of cells to find overlaps.

After this, the cells are moved given the forces acting upon them using the Euler method (note that we do not use the Verlet algorithm since the dynamics is overdamped). The cells then grow according to $\dot{\ell} = \gamma_g A f(c)$ where c is measured at the cell's center of mass. An amount $dtkf(c)$ of the nutrient is removed from the appropriate diffusion grid box. If the cell's length after growth is greater than ℓ_c, the cell reproduces, splitting into two cells with the splitting point at the centre of the mother cell. The two daughter cells have the same orientation as the mother cell, plus a very small random 'kick'. If this were not present, a colony starting from a single cell would grow in a straight line, as there would be nothing to destabilize the growth into another direction. However, this effect can be turned off after the first cell division, and causes no noticable difference to how the colony grows after that. Additionally, the splitting length for each cell ℓ_c can be slightly different: ℓ_c is taken from a uniform distribution in the range $(\bar{\ell}_c - \Delta\ell, \bar{\ell}_c + \Delta\ell)$. This prevents spurious synchronization of the cell divisions; such randomness in division times is observed experimentally.

Finally, the diffusion of the nutrient is calculated. The diffusion equation is moved forward one time step using a simple FTCS method, see Section 2.4. The time step used for the diffusion can in general be different than that used for the cells' dynamics. The nutrient concentration is held constant at the boundaries of the simulation box.

There are a few additional things to consider in the geometry comoving with a flat colony front. Here, cells which are deep within the colony and no longer growing appreciably must be discarded. Cells which have a growth rate below

some small threshold ϵ are set to be inactive, and no longer grow or move. If a cell is inactive and aditionally does not overlap with any cells which are active, it is removed from the simulation. Each time step, all variables are moved down in the y-direction so that the farthest back active cell is at the bottom of the simulation box; the simulation therefore takes place in a frame comoving with the actively growing front.

4.2.3 Parameters

Table 4.1 shows a summary of all parameters used in the simulation model and typical values used, along with estimates of realistic values for *E. coli* cells taken from experiments. All parameters have values which match fairly well with experimental values, apart from the diffusion constant D, which is considerably smaller in simulations. This was for reasons of computational efficiency, as a higher diffusion constant requires a smaller time step to solve numerically, and also would require a larger simulation box to prevent edge effects becoming significant. However, the diffusion constant does not appear to affect the dynamics of the front very much, for example Fig. 4.5 shows the speed of advance of the colony against D, showing little dependence. The parameter values given in the second column of the table are default values, and these are used in all simulations unless otherwise stated.

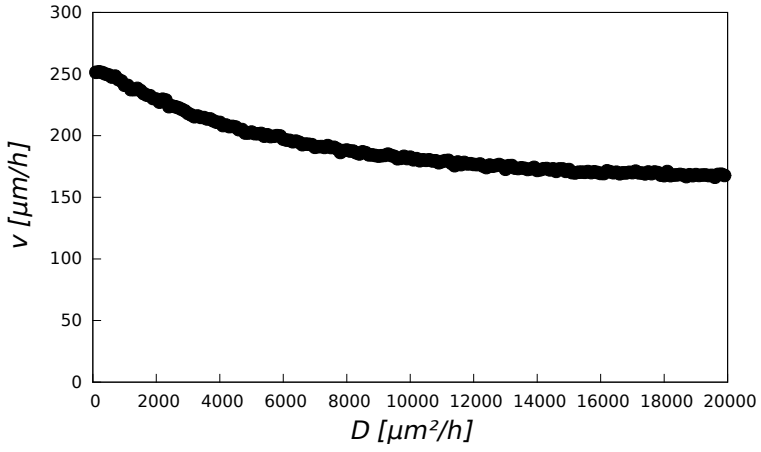

Figure 4.5: Expansion velocity V as a function of diffusion constant of the nutrient field D.

Parameter	**Simulations**	***E. coli***
Average length	3.75μm	2—4μm [116]
Average diameter	1μm	0.7—1.4μm [116]
Linear growth rate v_g	10μm/h	$\phi \approx$ 1—2h^{-1} which corresponds to $v_g \approx$ 4—8μm/h
Elastic modulus E	4×10^6 (10^5—10^7) Pa	0.5—5MPa ([117])
Friction coefficient ζ	200Pa·h	unknown
Nutrient concentration c_0	3 (0.1—5.0)fg/μm^3	4fg/μm^3 (0.4% M9 glucose medium)
Nutrient consumption rate k	50 (10—100)h^{-1}	80—160h^{-1} (estimated from data from Refs. [118])
Diffusion rate (glucose)	500 (100—10^5)μm^2/h	2—$4 \times 10^6$$\mu$m^2/h [119]

Table 4.1: Typical values of the parameters used in the simulation, and realistic values of the parameters for the bacterium *E. coli*. Values given in parentheses indicate the range of a particular parameter that has been explored in simulations. Note that the choice of units for E and ζ is somewhat arbitrary, as they only appear in the ratio E/ζ in simulations.

4.2.4 Morphology transition

Changing the initial concentration of nutrients c_0, or equivalently the rate at which cells deplete the nutrient k, can change the morphology of the colony in the same way as in the experiments described above: for high initial nutrient concentrations the colonies are dense and roughly round ('Eden-like' growth), whereas for low c_0 the colony exhibits a highly branched, fractal pattern, similar to diffusion-limited aggregation. Fig. 4.4 shows examples of these morphologies, in both the flat and round simulation geometries.

4.3 Theory of morphology transition

In order to develop a better understanding of what drives the growth of colonies under these circumstances, and in particular the origin of the observed morphology transition, we use a model whereby we approximate the growing colony as an incompressible cellular 'fluid'. Mass conservation in such a fluid is described by the equation $\nabla \cdot \mathbf{v} = \phi f(c(\mathbf{x}))$, where $\mathbf{v}$ the fluid velocity, $f(c)$ is the dimensionless nutrient uptake function, and ϕ is the growth rate of the cellular fluid, given by $\phi = \gamma_g/\ell_c$. This equation is the same as the mass

conservation equation for an ordinary fluid, except that the right hand side is not zero, reflecting the fact that the cells are proliferating, equivalent to there being 'sources' of fluid everywhere within it. A similar model was used in [120] to model biofilm growth, however there the circumstances modelled were different (fluid flow leading to a constant nutrient concentration a certain distance above the colony), and led to quite different results from those derived here.

Let us begin by considering this equation in a one dimensional case of a colony advancing from the left and consuming nutrient, and characterized by a single number $x_0(t)$ which is the position of the front:

$$\partial_t c(x,t) = D\partial_x^2 c(x,t) - k\rho_0 f(c(x,t))\Theta(x_0 - x), \tag{4.5}$$

$$v(x_0) = \frac{dx_0}{dt} = \phi \int_{-\infty}^{x_0(t)} f(c(x,t))dx. \tag{4.6}$$

Here D is the nutrient diffusion constant, k the rate of uptake of nutrient by cells, ρ_0 the cell density (constant everywhere due to incompressibility), and Θ is the Heaviside step function. Because cells do not migrate and they are tightly packed, the density is either ρ_0 or zero, so we take $\rho(x,t) = \rho_0\Theta(x_0(t)-x)$. Equation (4.6) comes from the fact that in one dimension and assuming incompressibility $dv/dx = \phi f(c)$. We also impose boundary conditions that $c(-\infty) = 0$ and $c(\infty) = c_0$.

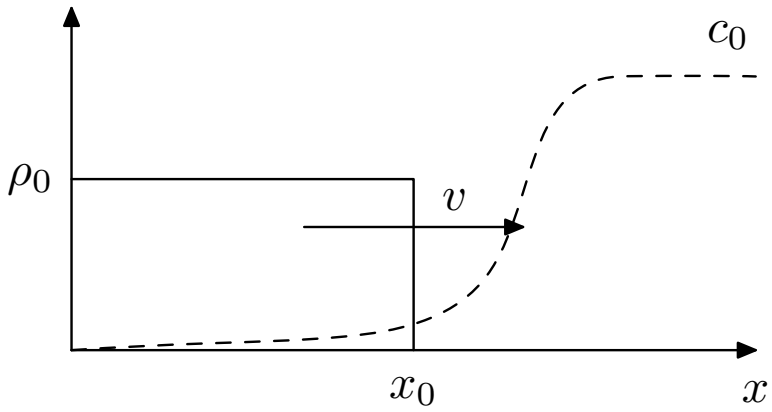

Figure 4.6: Schematic showing a travelling wave solution to Eqs. (4.5, 4.6). Solid line is cell density, dashed line nutrient concentration.

We first determine whether Eqs. (4.5, 4.6) admit a travelling-wave solution where the colony front expands forwards at a constant speed V; it seems

reasonable to expect this to be the steady-state solution. Such a solution will be of the form $c(x,t) = \hat{c}(x - vt) \equiv \hat{c}(z)$ in the limit $t \to \infty$, where the velocity V is constant; a schematic of such a solution is shown in Fig. 4.6. The resulting equations for $\hat{c}(z)$ and V are

$$-V\hat{c}'(z) = D\hat{c}''(z) - k\rho_0 f(\hat{c})\Theta(-z), \tag{4.7}$$

$$V = \phi \int_{-\infty}^{0} f(\hat{c}(z))dz. \tag{4.8}$$

For $z > 0$, the solution to Eq. (4.7) is given by $\hat{c}(z) = c_0 + Ae^{-vz/D}$ (as $c(\infty) = c_0$). For $z < 0$, we can rearrange the equation to yield

$$f(\hat{c}(z)) = \frac{1}{k\rho_0}\left(D\hat{c}''(z) + V\hat{c}'(z)\right)) \tag{4.9}$$

which, upon insertion into Eq. (4.8) gives

$$V = \frac{\phi}{k\rho_0}\left(D\hat{c}'(0) + V\hat{c}(0)\right) = \frac{\phi c_0}{k\rho_0}V, \tag{4.10}$$

where we have integrated by parts, and used the fact that $\hat{c}$ vanishes at $-\infty$, and that $\hat{c}$ and $\hat{c}'$ must be continuous at $z = 0$. Therefore, a solution for V exists only if $\phi c_0 = k\rho_0$ exactly: we have therefore found that in the incompressible limit the front cannot in general advance at a constant speed! This is in contrast to the Fisher framework, where travelling waves exist for a range of parameters. It is useful at this point to define the dimensionless parameter $\beta \equiv k\rho_0/\phi c_0$. This gives the amount of bacterial biomass produced per unit of nutrient, and a travelling wave solution only exists if $\beta = 1$ exactly. The implications of this are discussed further in the next section. Numerical solutions of Eqs. (4.5, 4.6) fully confirm our prediction, showing exponential growth for $\beta < 1$ and sublinear growth for $\beta > 1$, see figure 4.7.

From this simplified 1D model, we can see that $\beta = 1$ seems to be a critical value that separates different regimes of colony growth. For $\beta > 1$, growth is limited by nutrient diffusion and the colony slows down over time as nutrients become less and less available, whereas for $\beta < 1$ nutrient is plentiful and the colony grows exponentially, as it would if there were no nutrient limitation at all. However, the front has more freedom in two dimensions than it does in the

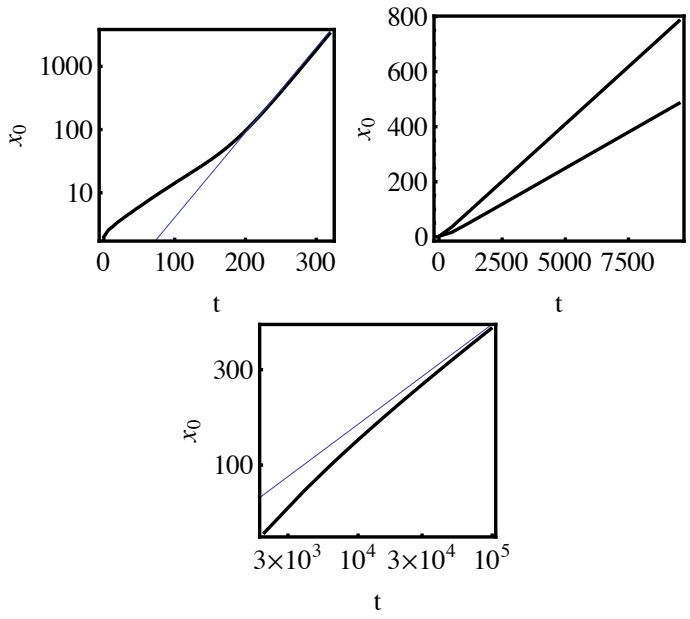

Figure 4.7: Numerical solution of Eqs. (4.7, 4.8). In all cases $c_0 = \rho_0 = 1$. Left: exponential regime, $\phi = 1.5k$ ($\beta = 2/3$), with fit to exponential. Right: linear regime, $\phi = k$ ($\beta = 1$). Here the behaviour depends on the initial condition; the two lines show solutions starting from two different starting values of x_0. Bottom: sublinear regime, $\phi = 0.7k$ ($\beta = 10/7$). The fit is to $\sqrt{t}$

simple one-dimensional model - it can develop irregularities (branches) in the direction lateral to the front gorwth direction. It is appealing to conjecture that the branching transition in Fig. 4.8 is linked to the switch in growth laws for incompressible colonies described above, i.e. that the branched growth occurs when $\beta > 1$. Running simulations using our model for different values of β lends support to this idea; it does indeed seem that β is the crucial parameter controlling the transition, which occurs when β is close to 1.

To quantify the transition, we measure the 'roughness' of the colony front σ_h, defined as the standard deviation of the colony height:

$$\sigma_h = \sqrt{\left\langle (h(x) - \bar{h}(x))^2 \right\rangle} \tag{4.11}$$

where the average is taken by measuring the height at 1μm intervals along the front. This quantity will depend on the width L of the colony if the colony

is rough: according to the Eden model of growth it will scale as $L^{1/2}$ at long times [109]. Fig. 4.8 shows the roughness as a function of β, from simulations done in the flat geometry for three different front widths L. Also plotted is the fraction s of space behind the front which is filled by cells; $s = 1$ for a perfectly flat colony ans $s < 1$ if there are branches leading to 'gaps' inside the colony. It can be seen that there are in fact two transitions, one from colonies that are almost completely flat to colonies that are rough, 'Eden-like', but still compact; and one between 'Eden-like' colonies and branched colonies with s significantly diffrent to 1 (i.e. there are gaps between branches).

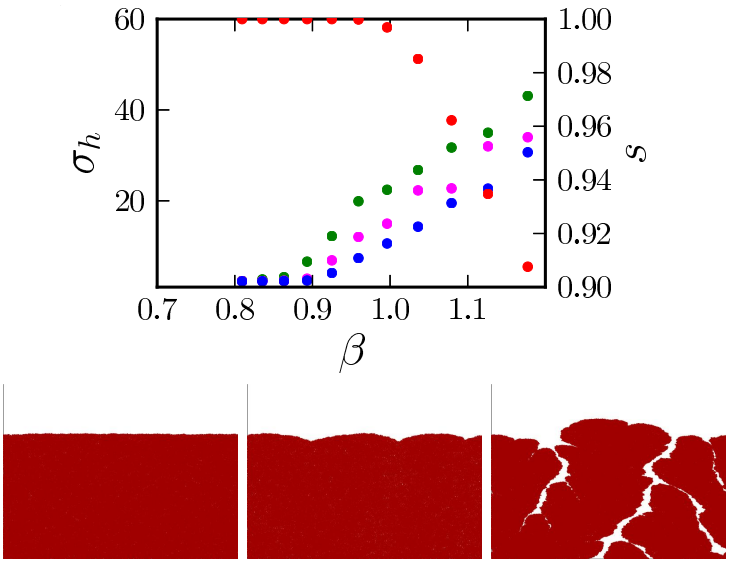

Figure 4.8: Top: colony roughness σ_h and filling fraction s as a function of β (done by varying nutrient conentration c_0, in the flat geometry). σ_h is the standard deviation of the colony height in microns, s the fraction of space behind the colony front filled by cells. The roughness is shown for three simulation box widths as it will depend on this width: $L = 500\mu$m (green points), $L = 250\mu$m (magenta) and $L = 125\mu$m (blue). In each case, there is a transition to a rough front around $\beta = 0.9$. The filling fraction s (red points, calculated for $L = 500\mu$m) first becomes different to 1 very close to $\beta = 1$. Bottom: snapshots of colonies, from left to right $\beta = 0.86$, 0.95 and 1.12.

The theory described above, then, seems to be a good description of the second transition, which occurs when $\beta = 1$. However, this incompressible theory predicts that growth cannot be linear, unless $\beta = 1$ exactly. This is inconsistent with experimental results: the size of a colony of non-swimming

bacteria growing on stiff agar gels *does* increase linearly with time [66]. Moreover, our simulations also lead to a finite steady state speed, even when $\beta < 1$ and the colony does not develop branches. The speed found in simulations depends on the cells' elastic modulus E: increasing the modulus increases the speed of advance of the front. This can be seen in Fig. 4.11. This suggests that the fact that the cells in simulations are not in fact incompressible but have a finite compressibility is important. We therefore developed a theory where the 'cellular fluid' is compressible, described in the next section.

4.4 Compressible theory

To describe a compressible cellular fluid, we use the mass conservation equation for a compressible fluid with a 'source' term describing cellular proliferation:

$$\partial_t \rho + \nabla \cdot (\rho \mathbf{v}) = \phi \rho f(c). \tag{4.12}$$

Unlike in the compressible case, when this along with the equation of the nutrient was enough to describe the dynamics of the front, we need a third equation since we have a third variable, ρ. This is the momentum conservation equation describing force balance:

$$\partial_t(\rho v) + (\mathbf{v} \cdot \nabla)(\rho \mathbf{v}) = -\nabla p - \mu \rho v. \tag{4.13}$$

Where p is the pressure in the fluid, and the final term on the RHS describes the frictional force exerted by the surface on the cells. Since the dynamics is overdamped, this can be simplified to

$$\nabla p = -\mu \rho \mathbf{v}, \tag{4.14}$$

note that this is the same form as 'Darcy's Law' [121] for fluid flow through a porous medium. Combining these equations with that for the nutrient diffusion, and again looking at the one-dimensional case of a flat front advancing in the x-direction, we have:

$$\partial_t c = D\partial_x^2 c - k\rho f(c), \tag{4.15}$$

$$\partial_t \rho + \partial_z(\rho v) = \phi \rho f(c), \tag{4.16}$$

$$\partial_x p = -\mu \rho v. \tag{4.17}$$

For the pressure constitutive equation $p(\rho)$, we take $p(\rho) = E(1 - \rho_0/\rho)^{3/2}$ to be consistent with our simulations, because the force that acts between two overlapping cells is then proportional to $Ed^{1/2}h^{3/2}$, where $h = d(1 - \rho_0/\rho)$ is the overlap. ρ_0 is the uncompressed density of closely-packed cells. It turns out that in this case a travelling wave solution does exist. The equations do not admit exact analytical solution, but some properties of the solution can be deduced without solving them directly.

If we again look for a travelling-wave solution of the form $c(x - Vt)$ and $\rho(x - Vt)$, we obtain:

$$Dc'' + uc' = kf(c)\rho \tag{4.18}$$

$$-u\rho' + (\rho v)' = \phi \rho f(c) \tag{4.19}$$

$$p' = -\mu \rho v \tag{4.20}$$

where the primes denote differentiation with respect to $z = x - Vt$. We can obtain an important constraint on the solution by just considering the conservation (including growth and depletion) of nutrient and of cells (equations 4.15 and 4.16). Integrating these over all z gives

$$[Dc' + uc]_{-\infty}^{\infty} = kI \tag{4.21}$$

$$[u\rho + \rho v]_{-\infty}^{\infty} = \phi I \tag{4.22}$$

where

$$I = \int_{-\infty}^{\infty} \rho f(c) dz \tag{4.23}$$

Putting in boundary conditions at $\pm\infty$, we get $uc_0 = kI$ and $u\rho_{\text{in}} = \phi I$, hence

$$\rho_{\text{in}} = \frac{\phi c_0}{k} \tag{4.24}$$

where $\rho_{\text{in}} = \rho(-\infty)$ is the density of cells deep within the colony. This equation makes intuitive sense and describes something akin to overall mass conservation:

the density of cells far from the colony front equals the nutrient density times the efficiency with which nutrient is converted to biomass, given by ϕ/k. This makes it clear why a travelling wave solution cannot exist in the incompressible case: unless the cell density takes the exact value $\phi c_0/k$ it will not match the density of biomass produced by the nutrient. It also explains why there is a morphological transition to branched colonies at $\beta \simeq 1$: growth of a compact colony is not possible for $\beta > 1$ as it would need to have a density less than ρ_0. Finally, it suggests that if bacteria are restricted to grow as a monolayer, then, when nutrient is abundant, they will grow exponentially until intermicrobial forces within the colony are so large that the bacteria in the middle are squashed to the appropriate density ρ_0/β. Fig 4.9 shows a schematic of the travelling wave solution and the conservation law.

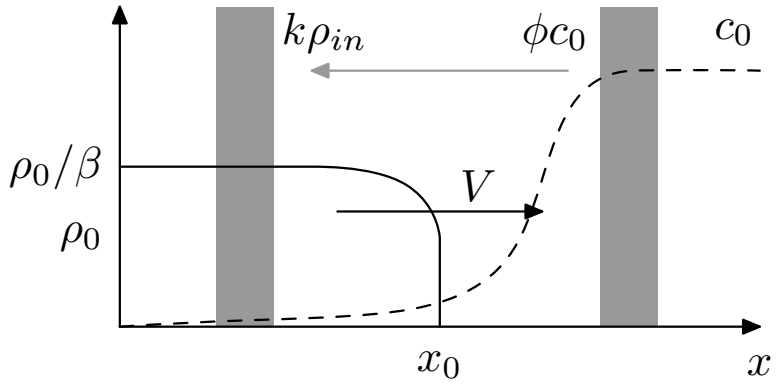

Figure 4.9: Sketch of the travelling wave solution of the compressible equations 4.15-4.17. For given parameters, an amount of nutrient (represented by the grey bar on the right) is converted into a fixed amount of bacterial biomass (grey bar on the left), whith the 'conversion' given by the ratio of the parameters ϕ and k.

Fig. 4.10 shows a plot of density as a function of $1/\beta$ taken from simulations, showing a good fit to the form $\rho_{\text{in}} = \rho_0/\beta$. Using this fit, ρ_0 is found to be 0.295 cells $(\mu\text{m})^{-2}$, fairly close to the value 0.264 obtained by inverting the average area of a cell. Note that, by taking the density to be the number of cells divided by the total area within the colony, including empty space when the colony is branched, the equation holds even for $\beta > 1$ and therefore $\rho < \rho_0$.

Note that this result depends crucially on the fact that the dependence of growth rate and uptake rate on the nutrient concentration c have the same functional form; this amounts to assuming that the growth yield of biomass per

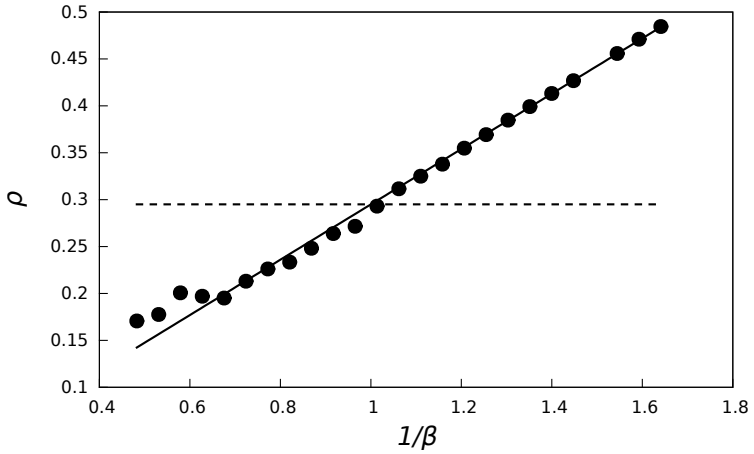

Figure 4.10: Plot from simulations in the flat geometry showing cell density deep within the colony as a function of $1/\beta$, done by varying c_0 while keeping other paramters constant. The 'biomass conservation law' predicts that $\rho = \rho_0/\beta$, and the solid line shows a fit to this, where ρ_0 is used as a fitting parameter, and is found to be equal to 0.295 cells $(\mu\text{m})^{-2}$. The dashed line is $\rho = \rho_0$. The density is calulated as $\rho = N^2/LR$ where L is the colony width ($= 250\mu$m), R the distance travelled by the front and N the total number of cells, i.e. it is averaged over the interior of the colony, including empty space in the case of branched colonies.

unit nutrient is independent of nutrient concentration. This assumption is likely to be reasonable in many situations, and the effect of relaxing it is decribed in section 4.5.

The above result can be used to generate a simple scaling argument for how quickly the colony front will advance. At steady state, the cells are compressed to a strain $\epsilon \equiv 1 - \beta$, and the pressure profile has to rise from 0 at the edge of the population to a maximal value p_* in the bulk within a boundary layer of characteristic size λ. The characteristic length λ can be eliminated by estimating it to be the length by which the front moves in one generation $\lambda \approx V/(\phi f(c_0))$. The bulk value of the pressure $p_*(\epsilon)$ is just large enough that the density of the population is compressed down to the strain ϵ. The elastic constitutive relation $p_*(\epsilon)$ of the microbial population fixes the corresponding pressure, with $p_*(\epsilon) = E\epsilon^{3/2}$ in our case of Hertzian contacts between cells. The pressure p_* pushes the front population at the speed V against the friction force $V\mu\rho_0\lambda$, where $\mu\rho_0$ acts

as a friction coefficient per unit length. Force balance thus yields

$$V \approx \sqrt{\frac{\phi f(c_0) p_*(\epsilon)}{\mu \rho_0}} = \sqrt{\frac{E \phi f(c_0)}{\mu \rho_0}} g(\beta), \tag{4.25}$$

where $g(\beta) = (1-\beta)^{3/4}$.

The above scaling form for the expansion velocity V agrees fairly well with simulations, see Fig. 4.11, in particular the square-root dependence on E. Also, this theory predicts that there is no dependence of the velocity V on the diffusion constant D. We saw in Fig. 4.5 that while there is some dependence, it is not very significant (V only changes by $\sim 30\%$ as D varies over 3 orders of magnitude). However, the dependence on β does not agree as well; in particular V is non-zero for $\beta > 1$. This is presumably because the fact that the colony forms branches in this regime means that the one-dimensional solution is no longer valid. To test this, I performed simulations in a genuinely one dimensional geometry: a line of cells growing end-to-end in a one dimensional nutrient field. The results of this are shown in Fig. 4.12. Here the agreement is better, with $V \approx 0$ for $\beta > 1$, but the form of the function $g(\beta)$ is slightly different to that derived above. However, the data agree very well with the form of $g(\beta)$ obtained from a full numerical solution of Eqs. 4.15-4.17.

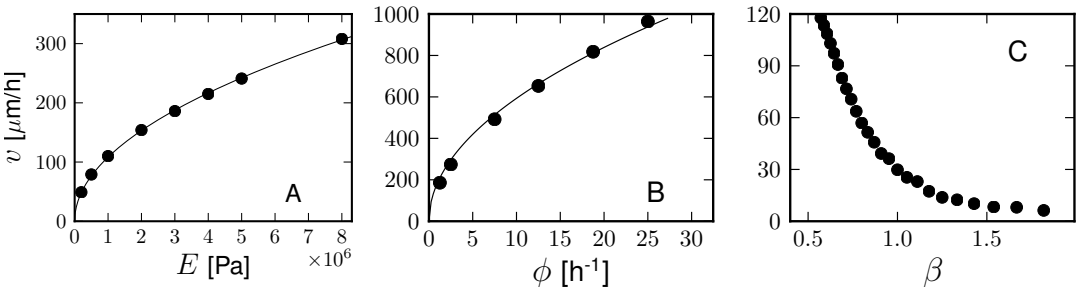

Figure 4.11: Steady state speed of colony growth, v, as a function of various parameters, for 2D simulations in the quasi-1D geometry. A and B have fits to a square root function. In B, ϕ is varied while holding β constant (by inversely varying k). C shows the dependence on β (c_0 is varied while keeping other parameters constant), with a change in behaviour around $\beta = 1$.

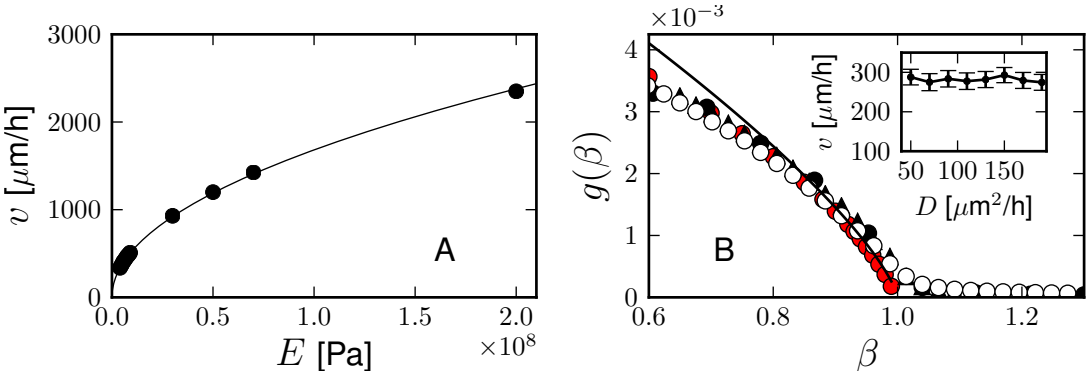

Figure 4.12: Dependence of front speed on parameters in the fully 1D simulation. A: front speed as a function of elastic modulus E, with fit to $v = A\sqrt{E}$. B: Transition from moving to stopped front as a function of β, which occurs when $\beta = 1$. $g(\beta)$ (defined by Eq. (4.25)) is plotted against β (by varying k) for $\phi = 10$ (open circles), 20 (triangles) and 30 (closed circles), showing a good collapse. Here $E = 4\times 10^6$, $D = 100$. Solid line corresponds to theoretical $g(\beta) = (1-\beta)^{3/4}$, and red circles are the numerical solution of Eqs. (4.15-4.17). Inset: v as a function of D, showing no dependence.

4.4.1 A more rigourous derivation of the expansion velocity

We start from equations Eqs. (4.18-4.20), for a travelling wave solution to the compressible fluid equations, travelling at speed V. For simplicity, we take the particular form $f(c) = c/c_1$ for the uptake function f. It is useful first to non-dimensionalize these equations by setting $\tilde{c} = c/c_0$; $\tilde{\rho} = \rho/\rho_0$; $\tilde{v} = v/V$ and $\tilde{z} = (V/D)z$ and omitting the tildes for clarity, to obtain

$$c'' + c' = \beta\Gamma\rho c, \tag{4.26}$$

$$-\rho' + (\rho v)' = \Gamma\rho c, \tag{4.27}$$

$$GF(\rho)\rho' = -\rho v, \tag{4.28}$$

where we now have three dimensionless parameters: $\beta = \phi c_0/k\rho_0$ as before, $\Gamma = \phi c_0 D/(V^2 c_1)$ and $G = E/(\mu D\rho_0)$. The dimensionless function $F(\rho) = (3/2)(1/\rho)^2(1-1/\rho)^{1/2}$.

We can further simplify these by eliminating $v(z)$ using Eq. (4.28) to replace ρv in Eq. (4.27) by $-GF(\rho)\rho'$, and Eq. (4.26) to replace $\Gamma\rho c$ by $(c'' + c')/\beta$. In

this way, we obtain a set of only two 2nd-order differential equations:

$$c'' + c' = \beta\Gamma\rho c, \tag{4.29}$$

$$-\rho' - (GF(\rho)\rho')' = (c'' + c')/\beta, \tag{4.30}$$

which are equivalent to the initial set of equations, with $v(z)$ being now (through Eq. (4.20)) a function of $\rho(z)$. Although we cannot solve Eqs. (4.29), (4.30) in the most general case, we can obtain some asymptotic results for $\beta \approx 1$ in the limit of $G \to \infty$ which is relevant for our simulations. Since there are derivatives over z on both sides of equation (4.30), we can integrate it over z to obtain

$$-\rho - GF(\rho)\rho' = (c' + c - 1)/\beta. \tag{4.31}$$

The constant $-1/\beta$ on the r.h.s. comes (as a result of integration) from the condition that $\rho(-\infty) = 1/\beta$. We then integerate a second time:

$$-G\int_{-\infty}^{0} F(\rho(z))\rho'(z)dz = \int_{-\infty}^{0} \left[\rho + (c' + c - 1)/\beta\right] dz. \tag{4.32}$$

The integral of $F(\rho(z))\rho'(z)$ is simply equal to $\int_1^{1/\beta} F(\rho)d\rho$. Recalling that $F(\rho) = dp/d\rho$, where $p(\rho)$ denotes the pressure, and that in our simulations $p(\rho) = (1 - 1/\rho)^{3/2}$, we obtain that the left-hand side of Eq. (4.32) equals $G(1-\beta)^{3/2}$. The integral on the right-hand side of Eq. (4.32) is more complicated. If we integrate the trivial term c'/β, we obtain

$$G(1-\beta)^{3/2} = -\frac{c(0)}{\beta} + \int_{-\infty}^{0} \left(\rho - \frac{1}{\beta}\right) dz + \int_{-\infty}^{0} \frac{c}{\beta} dz. \tag{4.33}$$

So far, all calculations are exact, but in order to proceed further we have to make some approximations. Let us assume that $\Gamma \ll 1$. Note that in the limit of $z \to -\infty$, $\rho(z) \to 1/\beta$, and Eq. (4.15) reduces to

$$c'' + c' = \Gamma c. \tag{4.34}$$

It follows that $c(z) \propto e^{\Gamma z}$ for $z \ll -1/\Gamma$ and that for $z > -1/\Gamma$ and $\beta \approx 1$ the concentration profile $c(z)$ is more complicated but it still decays over a characteristic length scale $1/\Gamma$. In this limit, $c''(z) \ll c'(z)$ which means that

diffusion becomes negligible. We may therefore assume that $c(0) \approx 1$ and from the mass conservation law we obtain that

$$\int_{-\infty}^{0} (\rho(z) - 1/\beta)dz = \int_{-\infty}^{0} \frac{\beta - 1}{\beta} c(z)dz. \tag{4.35}$$

Inserting this into Eq. (4.33) we obtain

$$G(1-\beta)^{3/2} \cong -\frac{c(0)}{\beta} + \int_{-\infty}^{0} c(z)dz. \tag{4.36}$$

In the limit of $\beta \to 1$, $c(z) \cong e^{\Gamma z}$ also for small z and, neglecting the term $\frac{c(0)}{\beta} \approx 1$, we finally obtain

$$G(1-\beta)^{3/2} \cong \frac{1}{\Gamma}. \tag{4.37}$$

Therefore, for small Γ, $G \propto 1/\Gamma$ is large. In other words, recalling the definition of $G \propto E/D$, our model is dominated by the mechanics of cells (repulsion forces determined by the elastic modulus E) rather than diffusion in the limit of small Γ and large G.

We can use Eq. (4.37) to determine the velocity of the growing front: from the definition of $\Gamma = \phi c_0 D/V^2$ we obtain that

$$V = \sqrt{\frac{\phi D c_0}{\Gamma}} \cong \sqrt{\frac{E(1-\beta)^{3/2}\phi c_0}{\mu \rho_0 c_1}} = \sqrt{\frac{E\phi c_0}{\mu \rho_0 c_1}} g(\beta), \tag{4.38}$$

where

$$g(\beta) \cong (1-\beta)^{3/4}, \tag{4.39}$$

the same result as obtained above in Eq. 4.25 by a simple scaling argument.

In the above analysis we assumed that we were in a regime such that $G \gg 1$, and the growth was dominated by mechanics. It is not yet clear, however, whether this is the regime we will be in for real bacterial colonies growing in thin layers. Although it is difficult to reliably estimate E and μ, we believe that it is. For the bacterium *E. coli*, E is reported to be of order 1-100MPa [117], $D < 5 \times 10^{-10} \mathrm{m}^2/\mathrm{s}$ (for glucose, see Ref. [119]). To estimate $\mu\rho_0$, we recall that its dimension is $\mathrm{kg}/(\mathrm{s} \cdot \mathrm{m}^3)$ and that it can be constructed from dynamical viscosity η ($10^{-3}\mathrm{Pa} \cdot \mathrm{s}$ for water), distance between the cell and the surface a (unknown but surely between 10^{-9} and 10^{-6}m), and cell's length l (about 5×10^{-6}m) as

the only relevant parameters. Thus $\mu\rho_0 = \eta/(al)$ must lie between 2×10^8 to $2 \times 10^{11}\mathrm{Pa} \cdot \mathrm{s/m}^2$. The estimated vlaues for real cells give $G = E/(D\mu\rho_0) \gg 1$, for any experimentally feasible values of the parameters.

4.5 Relaxing the constant growth yield assumption

Up to now we have assumed that the dependence of growth and nutrient uptake on the nutrient concentration have the same functional form $f(c)$, i.e. that the growth yield of biomass per unit nutrient is constant with respect to nutrient concentration. This will not necessarily be the case. For example, organisms may have constant 'maintenance costs', requiring nutrients (in particular energy) for functions other than growth, which would mean that the function describing uptake would be shifted up by a constant compared to that describing growth. *E. coli* cells have relatively low maintenance costs [122] and the assumption of constant growth yield seems to be reasonable for them, however this will not be the case for all bacterial cells [123, 124]. Cells may also, for example, have higher growth yields at lower nutrient concentrations in order to use resources more efficiently when they are scarce. To check how this affects our results, we have performed calculations and simulations in a simple case where the growth and uptake functions are not equal, taking the uptake rate to be given by $kf(c) = kc/c_1$ and the growth rate to be $\phi g(c) = \phi c/(c_1+c)$. This corresponds to a growth yield which smoothly decreases with increasing c.

Applying our incompressible theory to this case, we start with

$$\partial_t c(x,t) = D\partial_x^2 c(x,t) - k\rho_0 \frac{c(x,t)}{c_1}\Theta(x_0 - x),$$

$$v(x_0) = \frac{dx_0}{dt} = \phi \int_{-\infty}^{x_0(t)} \frac{c(x,t)}{c_1 + c(x,t)} dx. \tag{4.40}$$

We search for a solution of the form $c(x,t) = \hat{c}(x - Vt) \equiv \hat{c}(z)$ where V is a constant, yielding

$$-V\hat{c}'(z) = D\hat{c}''(z) - k\rho_0 \frac{\hat{c}(z)}{c_1}\Theta(-z), \tag{4.41}$$

$$V = \phi \int_{-\infty}^{0} \frac{\hat{c}(z)}{c_1 + \hat{c}(z)} dz. \tag{4.42}$$

Equation 4.41 is easily solved:

$$\hat{c}(z) = \begin{cases} c_0 + Ae^{-Vz/D} & z \geq 0 \\ Be^{\lambda z} & z < 0 \end{cases} \tag{4.43}$$

where

$$\lambda = \frac{-v + \sqrt{V^2 + 4Dk\rho_0}}{2D} \tag{4.44}$$

and, using the boundary condition that c and c' must be continuous at $z = 0$,

$$B = \frac{c_0 V}{D\lambda + V}. \tag{4.45}$$

We now put Eq. 4.43 into Eq. 4.42, and after some algebra we get that

$$\beta = \frac{k\rho_0 c_1}{c_0 V \lambda(V)} \log(1 + \frac{c_0 V \lambda(V)}{k\rho_0 c_1}). \tag{4.46}$$

We need to establish for which values of β this equation admits a solution for V. The function $V\lambda(V)$ takes values in the range $[0, k\rho_0)$. Putting the limiting values into Eq. 4.46, we get that a solution for V will exist if the following condition holds:

$$\beta \in \left(\frac{c_1}{c_0} \log \left(1 + \frac{c_0}{c_1} \right), 1 \right). \tag{4.47}$$

So there is a window close to $\beta = 1$ where growth with a constant speed is possible in the incompressible case.

To see how this applies to the compressible case, we ran simulations in one dimension. We have taken $c_1 = c_0 = 1$, so the predicted range of β with finite velocity is $\beta \in (\log(2) \approx 0.69, 1)$. Figure 4.13 shows the velocity v as a function of β, for two different values of the elasticity E. For $\beta > 0.7$, the speed v does not depend on E, suggesting that the colony would grow stably even for incompressible cells.

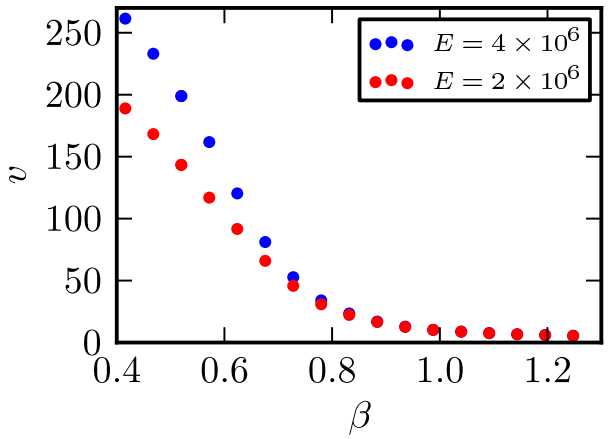

Figure 4.13: Speed of growth as a function of β (by varying k) obtained from the one-dimensional simulations with compressible cells for $f(c) = c$, $g(c) = c/(1+c)$. Two different values of E are shown (blue and red points). Other parameter are $c_0 = 1$, $\phi = 10$, $D = 1000$.

4.6 Three-dimensional growth

So far, our findings are relevant to bacteria growing in monolayers. On agar plates, however, cells are observed to build up vertically in the colony centre [125, 126], as cells are pushed out of the plane when their density becomes high. To probe how this affects our results, we simulate a colony growing in a vertical 2D plane xz (where the z axis is perpendicular to the substrate) instead of the xy plane from previous simulations. We also treat the diffusion of nutrient somewhat differently: rather than taking place in the 2D plane of the surface, it now occurs in the half-plane $z < 0$, modelling the fact that the nutrient in fact diffuses in three dimensions throughout the agar layer. We also incorporate a small attractive interaction between the substrate and the cells. This method of modelling the cells in a different two-dimensional plane rather than fully in three dimensions is far more computationally efficient, and still allows us to study the effect of vertical growth. As is apparent from Fig. 4.14A, cells do now escape out of the plane they start from, due to the force exerted by neighbours. The size of the colony once again grows linearly in time. However, it is not compressibility but the possibility of escape into the vertical direction which now leads to linear growth.

We can make a scaling argument for the speed of growth in a similar way to that developed above for a strictly two-dimensional colony. If the bulk pressure p,

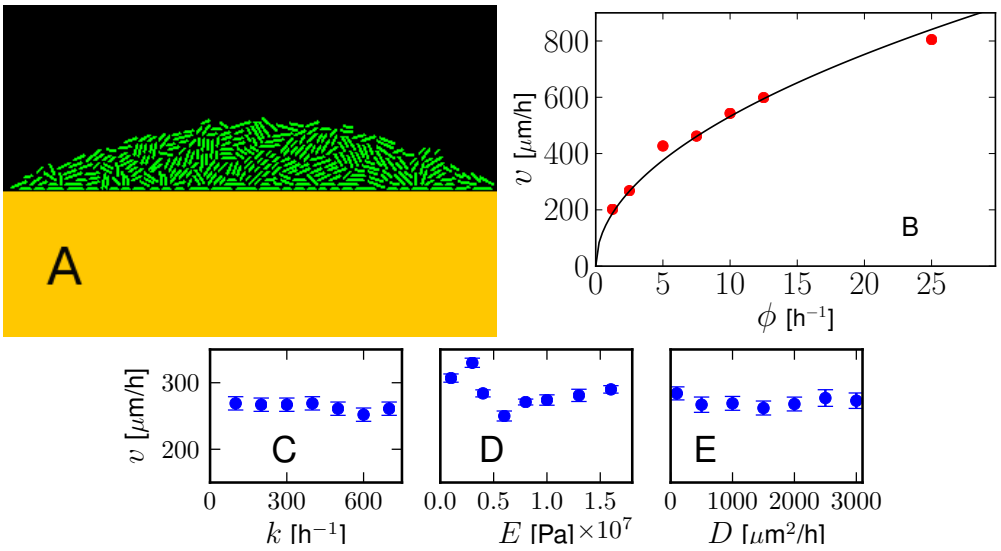

Figure 4.14: Quasi-3D colony growth. A: snapshot. B: Speed of radial colony growth against ϕ, with fit to $A\sqrt{\phi}$. C-E: speed against k, E and D, showing little dependence on any of these parameters. Parameters not being varied take their default values (Fig. 1).

which builds up in a strictly two-dimensional setting, is larger than some critical pressure p_c, cells will be forced out into the z dimension. As a consequence the pressure profile will saturate at p_c in the bulk of the population. In our scaling argument for the speed of the front growth, we replace $p_*(\epsilon)$ in Eq. 4.25 with p_c, which is now a constant. This gives

$$v \approx [(\phi f(c_0) p_c)/(\mu \rho_0)]^{1/2}. \tag{4.48}$$

Figures 4.14B-E show that, in contrast to the 2D case, the expansion speed $v \sim \sqrt{\phi}$ is now independent of the consumption rate k, elastic modulus E and the diffusion constant D, as predicted by this argument. Note that while the radial growth is independent of k, the vertical growth will be affected by it (a smaller k will lead to more vertical growth).

4.7 Nematic order

We have been modelling a growing bacterial colony as a kind of growing fluid. However, we have so far not taken into account the shape of the cells. The shape

of bacterial cells has important consequences for motility, nutrient uptake and cell division, amongst other things [127]. The bacteria we are modelling here are rod-shaped, like *E. coli* and many others. This means that the constituents of the fluid have an extra degree of freedom than if they were round, the angle of their axes, and that the cells can be more or less aligned with each other. The colony, therefore, behaves in some ways as a growing, active, nematic liquid crystal. In addition to fields describing the density, and velocity of the fluid, we can also have a field describing the degree and direction of alignment of the cells. Nematic ordering in bacterial colonies has previously been studied, for example, in [113], in the context of a dense colony of bacteria held in a rectangular channel. Here I will consider the case we have so far been discussing, of an expanding colony.

One effect which is rather unique to the case of a growing nematic is that the expansion flow in the colony will tend to align the cells along the direction of the velocity gradient, leading to an ordering effect and thus a non-zero order parameter. To see this, consider a single cell of length L in a fluid with a velocity gradient in the y-direction, with velocity increasing with increasing y, $\mathbf{v} = v(y)\hat{\mathbf{y}}$. If the cell is at an angle to the gradient, it will experience a greater force closer to its front, creating a torque that will align its direction along the gradient (see Figure 4.15). Quantitatively, the torque on the rod will be

$$\tau = \int_{-L/2}^{L/2} \zeta \ell \cos(\phi) v(y_0 + \ell \sin\phi) d\ell \tag{4.49}$$

where ϕ is the angle of orientation of the cell to the y-axis.

If the length of the rod is much smaller than the length scale over which the velocity changes, we can Taylor expand the velocity to yield

$$\begin{aligned} \tau &= \int_{-L/2}^{L/2} \zeta \left[v(y_0) + v'(y_0)\ell \sin\phi + \right] \ell \cos\phi d\ell \\ &= \frac{2}{3}\zeta v'(y_0) L^3 \sin(2\phi) \end{aligned} \tag{4.50}$$

so that we have

$$\frac{1}{12}\zeta L^3 \frac{d\phi}{dt} = \frac{1}{24}\zeta L^3 v'(y_0)\sin(2\phi) \tag{4.51}$$

where we have used equation (4.3) to relate the torque to the velocity of the rod.

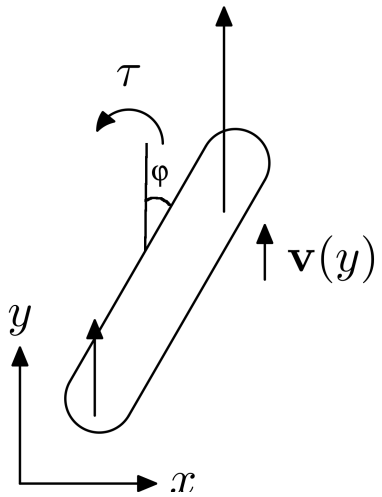

Figure 4.15: A cell in a flow field created by the other cells experiences a torque. The velocity field $\mathbf{v}$ is in the y-direction and increases with increasing y, which causes the cell to align parallel with the flow.

Therefore:

$$\frac{d\phi}{dt} = \frac{1}{2}v'(y_0)\sin(2\phi) \tag{4.52}$$

Note that the friction coefficient ζ has cancelled out, and that the equation is independent of the rod's length. The cell will align either parallel (for $v'(y_0) > 0$) or perpedicular (for $v'(y_0) < 0$) to the y-direction, in a time inversely proportional to the gradient of v. In the growing front of a colony, there is a velocity gradient in the direction of growth, since cells closest to the front are pushed by the growing cells behind them and therefore move faster. Considering a single cell moving in the 'fluid' created by the other cells, we therefore expect an alignment in this direction. Figure 4.16 shows a snapshot of the edge of a large round colony. It can be seen that the cells do indeed tend to align in the direction of growth, that is radially in a round colony. Note that at the edge of the colony some of the cells are aligned tangentially. This is to be expected, as the velocity essentially becomes zero outside the colony, so that $v'(y)$ is negative at the very edge and cells will tend to align tangentially there.

Starting from a single cell, then, the colony is initially very strongly aligned (in an arbitrary direction), as there are only a few cells and they all point in the same direction. As the colony grows, the cells tend to buckle and shift, reducing the order parameter. Then the ordering due to the expansion flow becomes

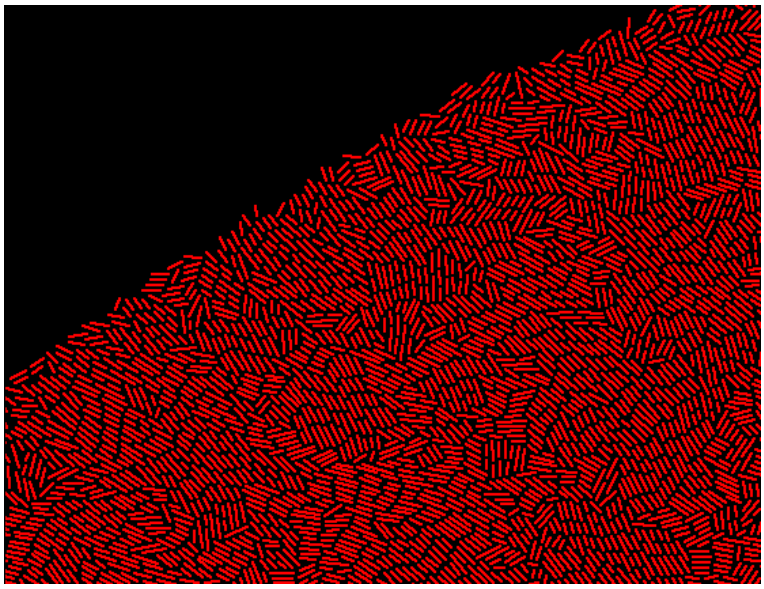

Figure 4.16: Snapshot of a section of a large circular colony from the simulation.

significant, leading to a significant radial ordering of the cells as they form a circular colony. The alignment of the cells can be quantified using the nematic order parameter:

$$Q_{ij} = \langle 2n_i n_j - \delta_{ij} \rangle \tag{4.53}$$

where $\mathbf{n}$ is the unit vector along a cell's axis. Q_{ij} is symmetric and traceless, so in two dimensions only has two independent components. Defining

$$Q = \sqrt{Q_{11}^2 + Q_{12}^2} \tag{4.54}$$

Q describes the degree of ordering in the system: it will be 1 if the cells are perfectly aligned, 0 if their orientations are random. Since we expect that the cells will align radially in a round colony, it is also useful to define a *radial* nematic order parameter

$$R = \left\langle 2\cos^2(\theta - \phi) - 1 \right\rangle \tag{4.55}$$

where $\theta = \tan^{-1}(y/x)$ is the angle from the x-axis of the cell's centre of mass and ϕ its angle of orientation. R will be 1 if cells are oriented perfectly radially within a colony, -1 if they are perfectly tangential. Figure 4.17 shows both Q and R as a function of the number of cells in a colony, showing that indeed the colony initially becomes disordered, and then develops radial order.

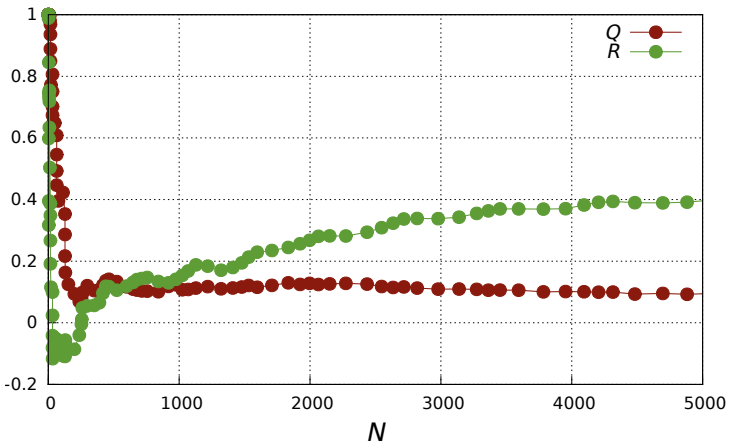

Figure 4.17: Orientational order parameters Q and R plotted as a function of the number of cells within a colony as it grows over time. Both paramters are equal to one when there is only one cell. The radial order parameter then quickly decays, followed by the global order parameter Q as the cells buckle and become less aligned. For large colonies (more than about 500 cells), the radial order parameter increases to around 0.4.

We can also compare the results of our simulations to experimental data on small colonies of bacteria growing on agar plates, as pictured in Fig. 4.3. This experimental work was done by Dario dell'Arciprete. The cells are grown on top of an agar surface with a coverslip pressed on top of them, and imaged using phase-contrast microscopy. The positions and orientations of the cells are then extracted from these images. Fig. 4.18 shows a comparison of the decay of the order parameters Q and R in both experiments and simulations. Note that the decay from high values as the colony first starts to grow is similar (especially for Q), but that the radial ordering effect for large colonies is not visible in experiments. The experimental colonies cannot be much larger than 500 cells, since at this point cells start to push into the agar, forming multiple layers in a similar way to that discussed in Section 4.6, and the radial ordering effect is not significant in the simulations for this number of cells, making comparison difficult.

We also considered the correlations of the orientations of the cells. We calculated the correlation function in two dimensions:

$$g(\mathbf{r}) = \langle \cos(2[\theta_i(\mathbf{0}) - \theta_j(\mathbf{r})]) \rangle \tag{4.56}$$

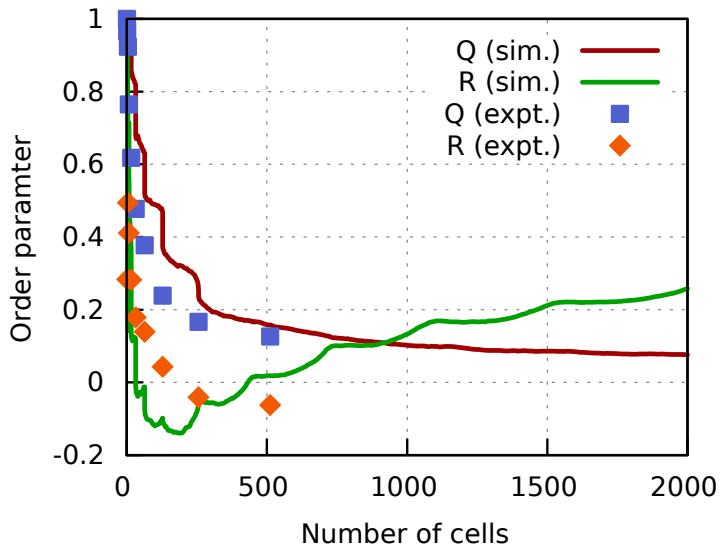

Figure 4.18: Orientational order parameters Q and R plotted as a function of the number of cells within a colony as it grows over time. In this case data from both simulations and experiments are shown. Both data sets are averaged over 33 colonies. The 'jumps' in the values which occur at multiples of 2 are due to this being when most of the cells divide, leading to large changes in the colony structure. For the experimental data, the order parameters were only calculated once every generation.

where the average is over all pairs of cells i, j. The axes are resolved onto the axes of the cell at the origin: for every cell, we calculate the average correlation of cells as a function of the distance along the cell's axis and perpedicular to it, then average this over all cells. Fig. 4.19 shows this function for simulation and experimental colonies. The functions look very similar for the experimental and simulation cases. There are a few peaks in the correlation function perpendicular axis, spaced about a micron apart, since the cells tend to line up in perpendicular rows and have a width of one micron. In the large simulation plot, 5 or 6 peaks are clearly visible, giving an idea of the typical size of these clusters. There are not significant peaks in the parallel direction, but there is a rather large negative correlation at a distance of about two microns in this direction; this is a steric effect due to the fact that two parallel cells cannot get this close to each other. This correlation function was calculated for an equilibrium system of hard spherocylinders in [128]. The plots their look very similar to these; therefore it appears that the activity arising from the growth of the cells does not qualitatively

affect the nature of these correlations.

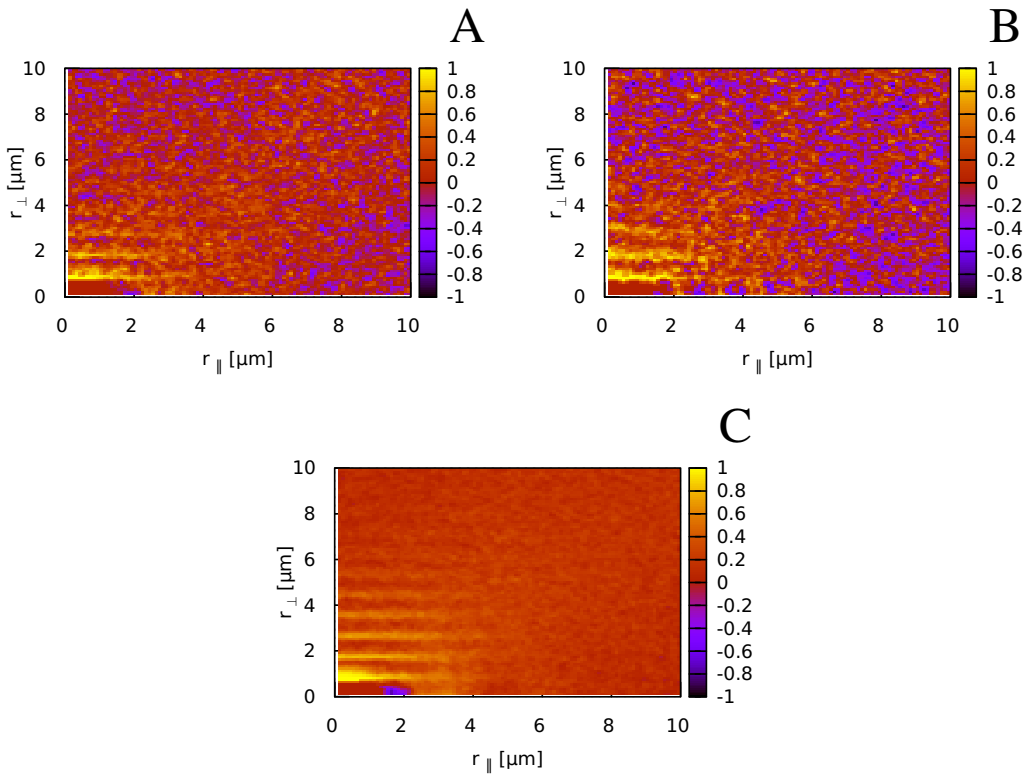

Figure 4.19: Orientational correlation functions $g(\mathbf{r})$ calculated for simulation colony with 517 cells (A), experimental colony with the same number of cells (B), and a simulation colony with 5000 cells for better statistics (C).

4.8 Possible extensions

While I have so far been talking only about bacterial colonies, the above model of a growing cellular 'fluid' might be applicable to other situations involving the growth of cells under limiting conditions, for example tissue and tumour growth in animal cells. These processes similarly involve a collection of cells proliferating and pushing on each other as they grow, often with their growth limited by the diffusion of nutrients. Agent-based and analytical models of tumour growth along these lines have recently been developed, for example, by the group of Prost [42, 45, 129]. A tumour typically first grows exponentially, and then the growth slows as the diffusion of oxygen into the cancerous cells becomes limited,

until blood vessels are developed (vascularization) [130, 131]. The phase before vascularization would appear to be very similar to the situation described above in our model, albeit in three rather than two dimensions. Note that if the cells are growing in a three-dimensional, spherical shape, the above theory should still be valid, but the cells will not be able to 'escape' by moving upwards as they can when growing in a disc.

Additionally, mechanical pressure due to the pushing of cells upon each other is understood to be very important in animal tissues. In particular, pressure appears to affect the growth and death rates of cells, with high pressure decreasing rates of growth and increasing rates of apoptosis [132, 133]. This leads to the idea of the 'homeostatic pressure' of a tissue: the pressure at which rates of birth and apoptosis of cells are balanced and the tissue is at equilibrium [129]. A tissue with a higher homeostatic pressure will crowd out one with a smaller.

This pressure-dependent growth may be an alternative form of growth-limitation in an expanding poplation of cells. Previous experiments and agent-based simulations indicate that a growing population of cells subject to such a pressure dependent growth rate can lead to steady-state (linear) rate of expansion [132, 134, 135]. Very preliminarily, it is relatively easy to extend our previous 'incompressible fluid' model to the case of pressure-dependent growth. We assume that nutrient is plentiful, so that it does not affect growth, and we have two equations for mass and momentum conservation:

$$\nabla \cdot \mathbf{v} = \phi f(p) \tag{4.57}$$

$$\nabla p = -\mu \rho_0 \mathbf{v} \tag{4.58}$$

where p is the pressure and we are assuming an incompressible fluid so that $\rho = \rho_0$ is a constant. The function $f(p)$ describes the pressure-dependence of the growth rate. I take a simple linear form with a cutoff (growth stops completely if $p > p_*$):

$$f(p) = \begin{cases} 1 - p/p_* & p < p_* \\ 0 & \text{otherwise} \end{cases} \tag{4.59}$$

These are easily combined into a single equation for the pressure:

$$\nabla^2 p = -\alpha(1 - p/p_*) \tag{4.60}$$

where $\alpha = \mu\rho_0\phi$. We again consider the one-dimensional case of a front travelling to the right, and look for a solution of the form $p(z) = p(x - Vt)$.:

$$\frac{d^2p}{dz^2} = -\alpha(1 - p/p_*) \tag{4.61}$$

for $z \leq 0$, with boundary condition $p(0) = 0$ (assuming atmospheric pressure is small compared with the cellular pressure). This yields a solution

$$p(z) = p_* \left(1 - e^{\sqrt{\alpha/p_*}z}\right). \tag{4.62}$$

We now note that $V = v(0) = -p'(0)/(\mu\rho_0)$ from Eq. 4.58, giving

$$V = \sqrt{\frac{\phi p_*}{\mu\rho_0}}. \tag{4.63}$$

So steady-state growth is indeed possible in this case. The form of the expansion speed is exactly as would be expected from the scaling argument used in Sections 4.4 and 4.6 above, where the expansion velocity is given by $\sqrt{(\phi p_*)/(\mu\rho_0)}$, where p_* is the pressure deep within the colony, which 'pushes' the growing layer outwards.

Note that if there were no cut off in the growth as a function of pressure (e.g. if $f(p)$ were an exponential decay) a steady-state speed would not exist, as the pressure and therefore the speed would increase without limit as the colony grew.

4.9 Conclusions

In this chapter I have described a model of the growth of bacterial colonies whereby the expansion of the colony is driven by the mechanical pushing of the cells as they grow. Such a system can be usefully modelled as an active, growing, nematic fluid. The model differs significantly from previous models of colony growth based on generalized Fisher-Kolmogorov equations, in that the diffusion of the cells themselves is not important, and makes different predictions. In particular, I have shown that the growth of a round colony at constant density in two dimensions is not possible: the colony will either develop branches (at low nutrient concentrations), or become compressed in the centre (at high nutrient

concentrations). The transition between these two regimes is driven by the efficiency with which the colony converts nutrient into cellular biomass. This result does depend on the fact that the dependence of nutrient uptake and cellular growth rate on nutrient concentration have the same functional form, however relaxing this assumption does not seem to affect the results very much, apart from introducing a rather narrow range of nutrient concentrations at which steady growth is possible. In three dimensions (where cells are able to leave the surface and start growing upwards) the results are again similar, except that cells will tend to leave the surface rather than being physically compressed in the centre if the nutrient concentration in high.

The two-dimensional theory could be tested experimentally by growing cells in a quasi-two-dimensional microfluidic device, i.e. by physically confining them to a two-dimensional space. We predict that in this case under plentiful nutrient conditions the cells in the centre of the colony will become significantly compressed. The same results would also hold for cells (bacterial or animal) growing in a three-dimensional spheroid, so this might be another way to test the theory.

Chapter 5

Competition and genetic drift in biofilms

5.1 Introduction

In the previous chapter I described an agent-based model of the growth of a bacterial biofilm on a surface, giving results on what factors affect how quickly such a colony will grow and what its shape will be. In this chapter I describe further work on this simulation model, but change tack somewhat. I now consider the fact that such a colony is made up of individuals which are in competition with each other, and will study natural selection in this situation. Evolution in populations which are expanding in space has been the subject of much recent research [64, 65, 67, 111, 136], and has some significant differences from well-mixed systems, and from spatial systems where the space is fully occupied to start with. This is mostly due to the so-called 'founder effect', where individuals close to the expanding front of the population have a much better chance of passing their genes on to future generations than those deep within the population. Since there are relatively few of these 'founders', there is a large degree of randomness in terms of which cells are able to pass on their genes into the uncolonized territory. Such randomness is termed 'genetic drift'. Genetic drift is the change over time in the frequency of gene variants due to the random way in which a population reproduces, i.e. due to random sampling [137, 138]. It means that over time frequencies of different variants will shift around, even if there are no fitness differences. Genetic drift in an expanding population is more important than in

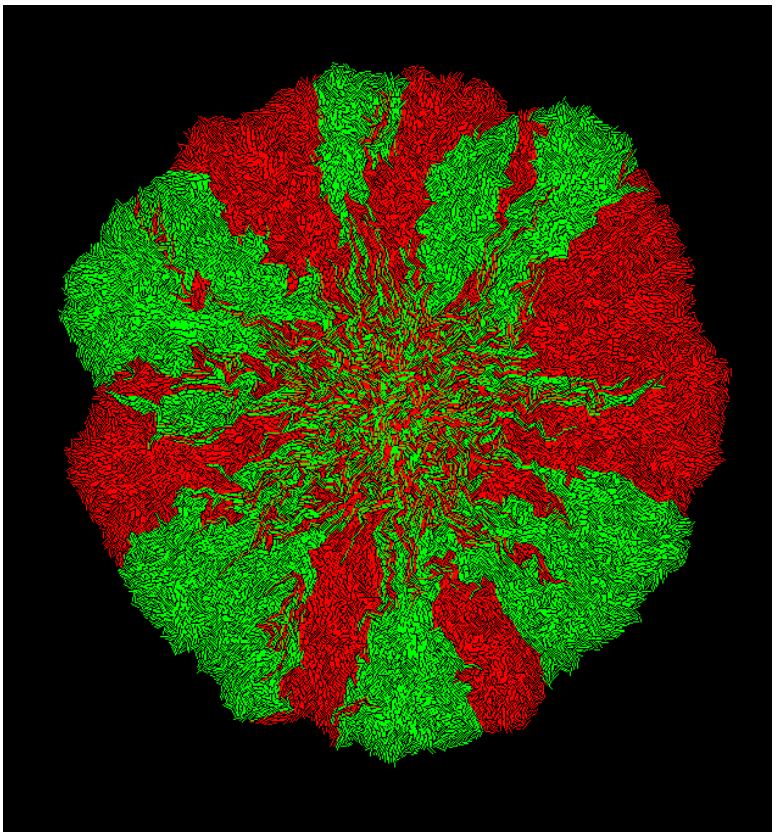

Figure 5.1: A snapshot from our simulations showing the sector patterns. When there were around 1000 cells, half were labelled green, half red, at random.

a well-mixed one for the reasons described above.

The large amount of genetic drift can be strikingly demonstrated in the lab using colonies of bacteria growing on agar plates. Such a colony is started with half of the cells expressing a green flourescent protein, and half a red one, at random, with no other differences between the two cell types. As the colony grows, large red and green sectors form (see [66]; Figure 5.1 shows this situation in our simulation) – a kind of 'genetic demixing' has occurred. This is because only cells in a narrow region at the edge of the colony are able to pass on their genes, due to nutrient limitation and physical confinement by other cells within the colony. Each sector corresponds roughly to the descendants of a single ancestral cell, and these sectors quickly become large due to the large amount of genetic drift.

There has been much previous work exploring evolution during range expansions theoretically, generally using idealized, continuum models, such as modified

Fisher-Kolmogorov equations [67, 136, 139], as well as agent-based simulations used to study issues such as the evolution of cooperation and selfishness in growing biofilms, e.g. [60, 64, 65, 111, 112]. Here we wanted to use our more detailed biophysical model of colony growth on agar plates to explore some experimentally observed effects in this situation. In particular, we are interested in the effect of colony morphology (i.e. the roughness of the expanding front) and mechanical factors such as the shape of the cells, on the dynamics of the sector patterns (and therefore neutral genetic drift), and the fixation of beneficial mutations.

5.1.1 Selection of beneficial mutations

We wanted to study *selection* in an expanding population, rather than the case of 'neutral' evolution when there are no fitness differences described above. In particular, we wanted to analyse what happens to a beneficial mutant, that is, a mutant which has a fitness advantage over the other cells in the colony, as it grows more quickly and therefore produces more offspring. Such a mutant may either go on to completely take over the expanding colony frontier (termed 'fixation'), or it may be randomly outcompeted by other cells and go extinct. The probability that a beneficial mutant will fixate in the population is expected to be much reduced compared to the well mixed case due to the large amount of genetic drift, which means that stochastic fluctuations are more important and can swamp the fitness advantage of the mutation. Essentially, inferior genotypes can 'surf' on the wave of the expanding front. The question of how effective selection is in an expanding colony is of practical importance, as expanding colonies of bacteria such as biofilms are involved in many infections, and these beneficial mutations may correspond, for example, to increased virulence or to antibiotic resistance.

The group of Oskar Hallatschek has recently performed experiments where, instead of flourescently labelling two otherwise identical strains, a strain with a mutation such that it grows faster (i.e. has a fitness adventage) over the wild-type is used. Figure 5.2 shows some preliminary results of these experiments, where, as before, the system was started with a mixture of the two types of cells, and sectors are seen to form as the colony expands. However, in the bottom set of experiments the blue strain has a fitness advantage. Firstly, it can be seen that for the rough front (colony grown at 37°C) the fitter mutant is not completely dominant even at quite long times; at some places along the front there are sectors

of wild-type cells which have stochastically outcompeted it. Secondly, by changing the temperature at which the colonies were grown, their morphology (roughness) can be changed, and we see that rougher fronts have fewer neutral sectors, and seem to hinder the fixation of beneficial mutations. We hypothesised that the roughness of the front affects the fixation proabability because a rougher front will cause the boundaries between sectors to meander more as the colony expands, increasing the amount of stochasticity in the system (i.e. increasing genetic drift) and therefore reducing the fixation probability of beneficial mutants. We used our simulation model to investigate this question, and found that the roughness does indeed appear to affect selection in this way. We also probed other factors which might affect fixation proababilities, such as mechanical features of the cells.

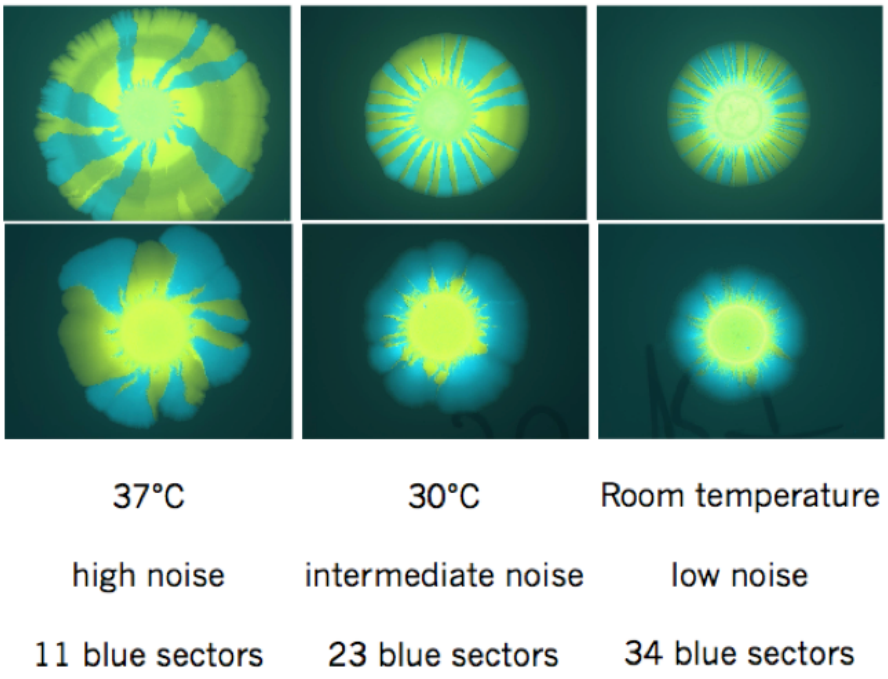

Figure 5.2: Top: neutral sector experiments done at different temperatures, showing a correlation between the roughness of the colony front and the number of sectors. Bottom: a similar experiment, but in this case the blue strain has a fitness advantage over the green. Image courtesy Oskar Hallatschek and Fabian Stewie.

5.2 Simulations

To analyse genetic drift and evolution in our simulations, we perform two main kinds of computational 'experiments'. To characterise the amount of genetic drift in the system, we use the well-studied 'sector' method described above, whereby cells in the colony are given two different labels (e.g. red and green), and the colony evolves, producing a pattern of sectors, as described above in the introduction to this Chapter. By tracking the number of sectors over time (the number decreases roughly as $N_{sectors} = N_0 R^{-\alpha}$ where R is the distance travelled by the colony front and $\alpha > 0$ is some power), we can characterise the amount of genetic drift at the advancing front under different conditions (e.g. different front thickness or roughness).

As a more direct probe of the fate of mutants in an expanding colony, we also run simulations involving 'mutant cells' which have a higher growth rate than other cells. There are many possible ways to introduce such mutant cells. The most biologically realistic is to have a small probability p that a cell will produce a fitter mutant daughter cell on division. This mutant has a larger growth parameter: $\gamma \to \gamma' = \gamma(1 + s)$ where s is the fitness advantage of the mutant. We are then interested in the probability that such a mutant will go on to reach fixation in the population. To do this, we wait until such a mutation occurs, then stop the mutation process to prevent further mutants from interfering with the new mutant lineage, and see whether the lineage goes extinct or fixates. Fixation in this situation is taken to have happened when all the cells which have a growth rate above some small threshold (i.e. all the cells in the growing layer) are mutants, with extinction defined similarly. This simulation is run many times with different random numbers, and the probability of fixation is estimated by taking the proportion of such runs over which the mutant fixates. We run these simulations in the flat geometry for computational efficiency. Snapshots showing the development mutant sectors introduced in this way are shown in Fig 5.3.

5.2.1 Effect of colony front thickness and roughness on fixation probability

One important thing to note is that only cells born extremely close to the frontier of the expanding colony (within a few cell diameters) have a significant chance

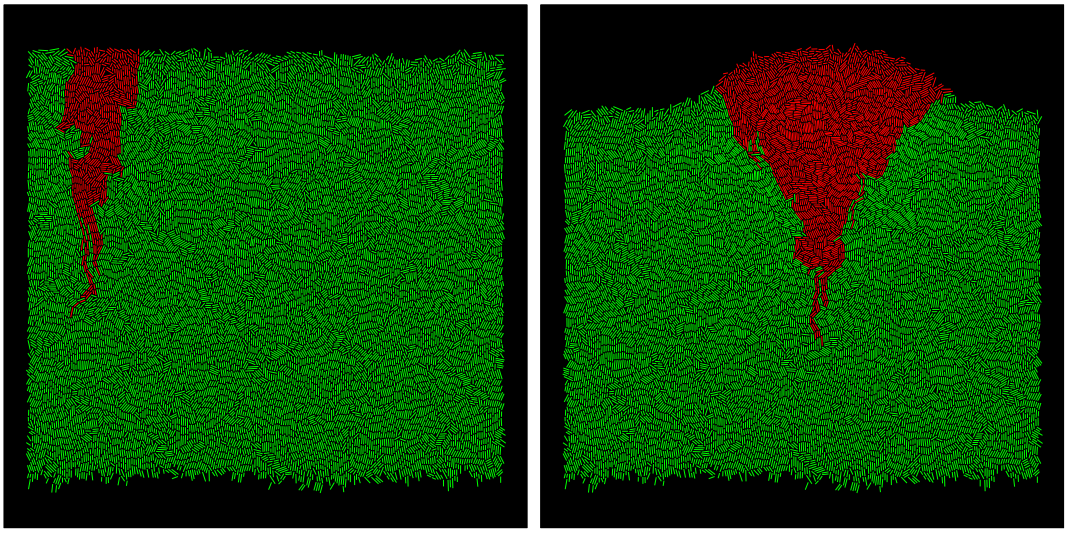

Figure 5.3: Snapshots from simulations showing the development of mutant sectors. Red cells are wild type, green cells are a fitter mutant. Mutant sectors when the fitness advantage is 10% (left) and 50% (right). These mutants are likely to be successful as they have formed macroscopic sectors; most mutants are stochastically outcompeted by wild-type cells before they can produce more than a few descendants.

of going on to fixate in the population. Cells born any deeper within the colony than this not only grow more slowly (due to reduced nutrient concentration) but must get past the cells in front of them. This is unlikely to happen, even if the cell has a significant fitness advantage, as the cell's growth will also tend to push forward the cells in front of it. Figure 5.4 demonstrates this effect. A simulation was run (again in the flat geometry) in which every cell's lineage was tracked to see whether it went on to fixate, or to go extinct at the frontier (one of these two will happen to every lineage eventually). Every time a cell was born, its position behind the front was noted, and then its descendants were tracked to see whether they fixated or went extinct. From this the function $P(z|\text{fixation})$ was calculated, this being the probability that a cell was born a distance z behind the colony front, *given that it then went on to fixate in the population.* As can be seen from the figure, cells born more than $\sim 5\mu$m from the colony edge have a negligible chance of fixating. The function $P(z)$, the probability that a randomly chosen cell is born a distance z from the front irrespective of the fate of its lineage, is shown for comparison, and both functions are plotted for two different front thicknesses.

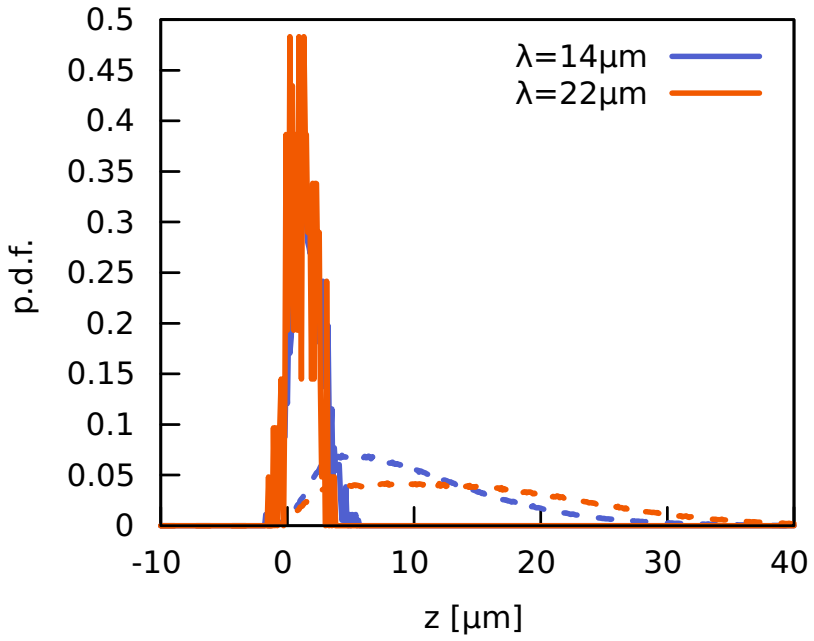

Figure 5.4: $P(z|\text{fixation})$ (solid lines) and $P(z)$ (dashed lines) plotted for two different front thicknesses. This was done for a colony with no mutants, in the flat geometry with $L = 250\mu$m

As mentioned above, the thickness of the growing layer of cells can be varied by changing the initial nutrient concentration c_0. This affects the fixation probability of a mutant, see Fig. 5.5, which shows the probability of fixation of a mutant cell as a function of front thickness, when the mutant is introduced as described above in Section 5.2, by random mutation on birth of a new cell. These results are somewhat difficult to interpret, however, as there are two competing effects occuring. On one hand, increasing the thickness may decrease the fixation probability of a mutant, since as the growing layer becomes thicker, it is more likely that a mutant will be born some distance behind the front, where it is very unlikely to go on to fixate. On the other hand increasing thickness may also increase this probability by making the front smoother (i.e. there are fewer fluctuations in the height of the front), decreasing the meandering of sector boundaries and therefore the amount of genetic drift. These competing effects mean that the probability of fixation is relatively low for both high and low values of the front thickness, with a peak for intermediate values, as can be seen in Fig. 5.5. However, although it is statistically significant, this effect is not very

pronounced.

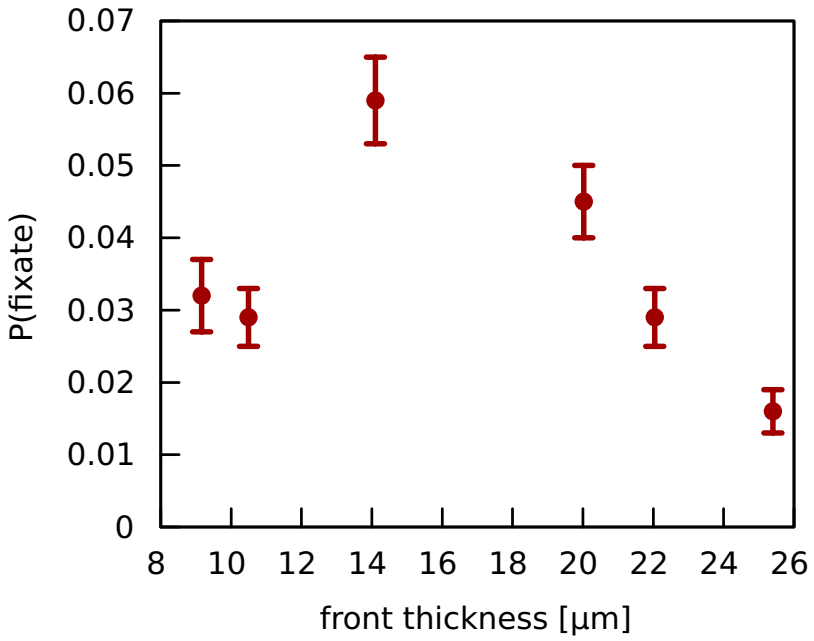

Figure 5.5: Probability of fixation as a function of front thickness. Here the fitness advantage of the mutants was 0.05, and the front width L was 100μm.

To make the effect of the roughness clearer, we used an alternative method of introducing mutants to the front, which removes the effect of front thickness. In the flat geometry, we start from a narrow band of cells, around 100μm in length and 50μm thick, and convert a certain proportion of cells, chosen at random, into fitter mutant cells. The simulation is then run until either the mutants or the wild-type cells completely take over the colony, and the proportion of runs in which the mutants take over is used as an extimate of the fixation probability. Since the initial condition is always the same, the effect whereby front thickness reduces fixation probability due to the possibility of the mutant being born far from the frontier is no longer present. Figs. 5.6A and B show the fixation probability in this case plotted against front thickness and roughness. The roughness is quantified, as before in Chapter 4, by taking the standard deviation of the front height: roughness $\sigma_h = \sqrt{\langle (h(x) - \bar{h})^2 \rangle}$. We see that there is a clear effect whereby a rougher front reduces the fixation probability, in agreement with the preliminary experiments shown in Figure 5.2.

Note that we start these simulations with many mutants rather than one

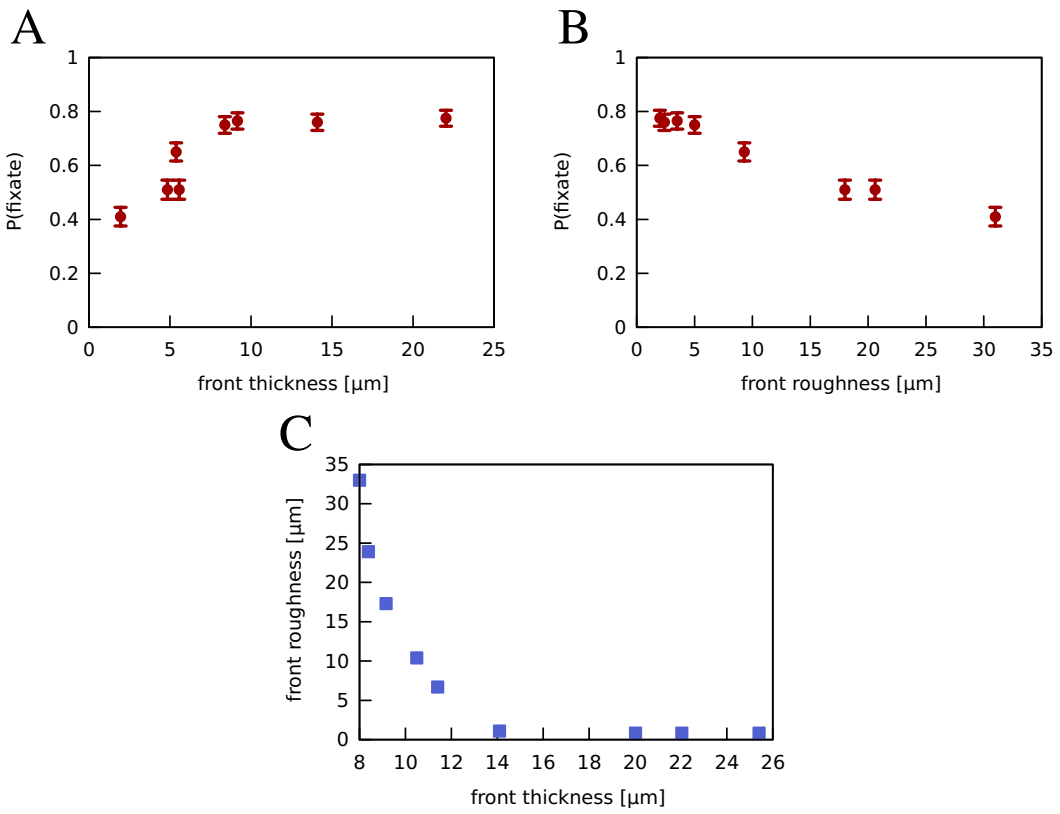

Figure 5.6: Fixation probabilities in the case of multiple mutants, plotted against thickness (A) and roughness (B) of the front. Fitness advantage s was 0.05, $L = 100\mu$m, initial proportion of mutants was 5%. (C) Shows the dependence of front roughness on thickness. The fixation probability appears to be mostly determined by the roughness: both the roughness and P(fixate) saturate for values of the thickness greater than $\sim 15\mu$m.

in order to increase the probability that some mutant lineage fixates in the population, allowing us to achieve a better estimate of the fixation probability using fewer simulation runs. The probability that mutants take over the colony given that there are N mutants in the colony to start with can be related to the probability that a single mutant will take over the colony by noting that the probability that no mutant fixates is equal to $(1-p_1)^N$, where p_1 is the probability that a single mutant fixates, and we assume that the probability of fixation of a given mutant is unaffected by the presence of other mutants, giving

$$p_N = 1 - (1 - p_1)^N.$$

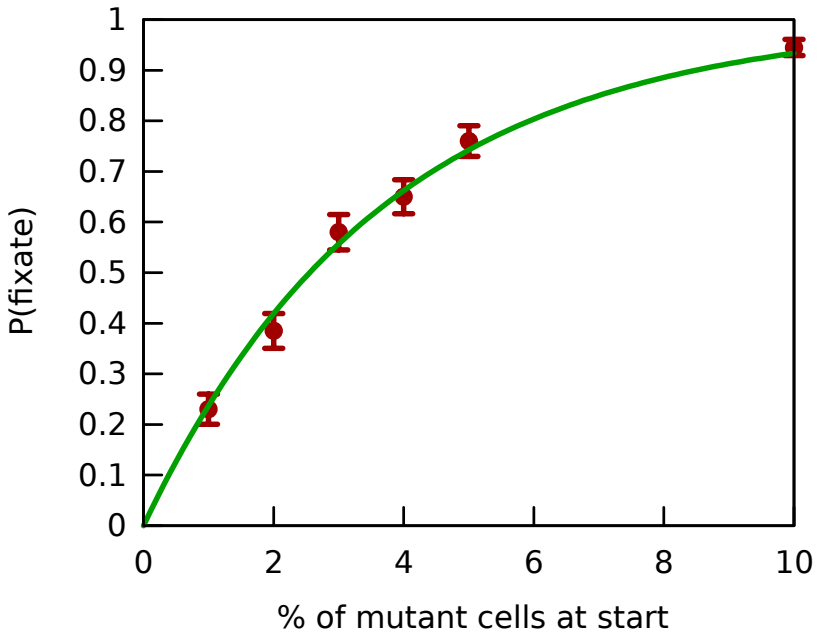

Figure 5.7: Probability of fixation of mutant cells plotted against initial proportion R of mutant cells. Here the thickness of the front was 14μm, and the fitness advantage was 0.1. Green line is a fit to $P(\text{fixate}) = 1 - e^{-aR}$, with the fit parameter $a = 0.271$, corresponding to the prabability of fixation of a single mutant $p_1 = 0.019$.

Assuming that p_1 is small, p_N can be approximated to $p_N \approx 1 - e^{-p_1 N}$. Fig. 5.7 shows the probability of fixation plotted against the initial proportion of fitter mutants along with a fit to the above function. The fit is good, indicating that the assumption of independence above is reasonable, at least for mutant ratios up to 10%.

5.2.2 Number of neutral sectors

In this section I relate the above results on fixation probabilities to the decay of the average number of sectors (lineages) over time in an expanding colony. In the flat geometry, an initial condition like that employed above, with a narrow band of cells approximately 100×50μm, is used. Each cell in this band is given a different label, and the number of such lineages which are still extant (i.e. still present in the growing layer) is measured as the colony advances. The rate at which this number decays gives an idea of the amount of genetic drift occuring in

the expanding colony. Figure 5.8 shows the number of sectors measured in this way and averaged over 10 simulation runs for two different front thicknesses. The thinner front in this case exhibits a branched morphology, as in Fig. 4.4D, and it can be seen that the sector number decays very quickly to one. For the thicker front, which is relatively smooth as in Fig. 4.4C, the sector number decays much more slowly, and is a good fit to $N_{sectors} = N_0 R^{-\alpha} + 1$ (the number of sectors decays to 1, not 0, for long times), with α measured to be ∼0.64.

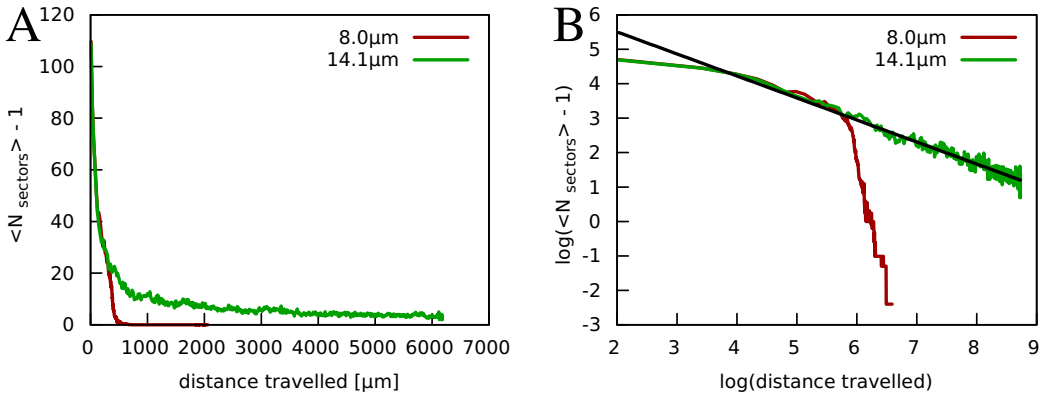

Figure 5.8: Decay of the number of sectors against distance travelled by the front for two different growing layer thicknesses, plotted on linear (A) and log-log (B) scales. The number is averaged over 10 simulation runs. The black line in (B) is a fit to a straight line with slope ∼0.64, corresponding to $\langle N_{sectors} \rangle \sim R^{-0.64} + 1$ where R is the distance travelled.

As expected, then, the number of sectors decays more quickly for thinner fronts, due to the larger amount of genetic drift. Fig. 5.9 shows the number of neutral sectors after the front has travelled a certain distance, plotted against front roughness and thickness. The behaviour of the number of sectors is similar to that of the probability of fixation of a fitter mutant, depending mostly on the roughness of the front, as expected.

5.2.3 Mechanical effects

In this section I describe the effects of varying mechanical aspects of the simulation model – such as the shape of the cells and the nature of the friction force between the cells and the substrate – on genetic drift and fixation probabilities. As mentioned above, the precise nature of the frictional force between a bacterial cell and an agar surface is not currently well understood. In

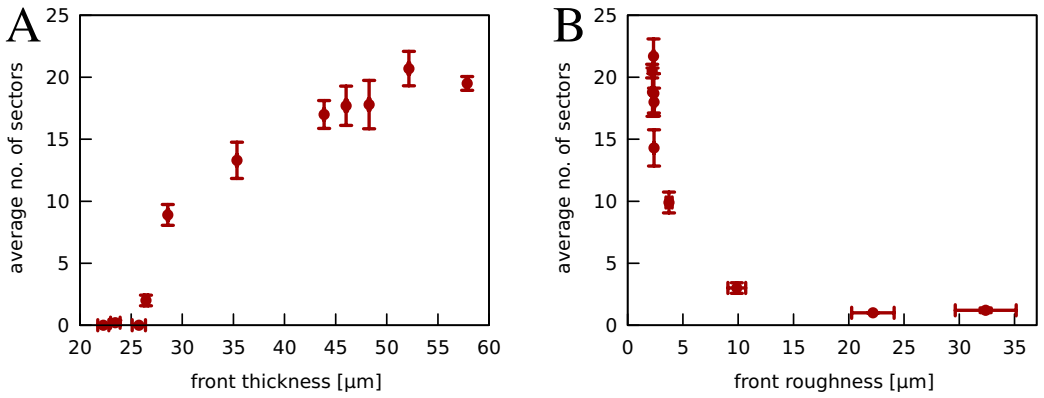

Figure 5.9: Number of neutral sectors plotted against colony front thickness (A) and roughness (B). Simulations were started in the same initial condition with each cell given a different label, and the number of lineages (different labels) remaining in the colony front after it had advanced a distance of 500μm was measured, and averaged over 10 simulation runs for each thickness. Here the lateral width of the simulation box L was 250μm.

the above simulations, the frictional force was taken to be a simple form whereby the force is proportional to the cell's velocity, irrespective of the direction of motion with respect to the cell's axis. To test whether this assumption affected the properties of colonies we are interested in, I ran simulations in which this assumption was changed, by using different friction coefficients in the directions parallel and perpedicular to the cell's axis. This was inspired by the case of the friction felt by rods in solution, in which case the friction coefficient perpendicular to the rod's axis is twice that parallel to its axis [140]; here I allowed these friction coefficients to be free parameters:

$$\dot{r}_\perp = \frac{1}{\zeta_\perp \ell} F_\perp; \tag{5.1}$$

$$\dot{r}_\parallel = \frac{1}{\zeta_\parallel \ell} F_\parallel; \tag{5.2}$$

$$\dot{\phi} = \frac{12}{\zeta_r \ell^3} \tau \tag{5.3}$$

As can be seen in Fig. 5.10, friction anisotropy can strongly affect the probability of fixation of a beneficial mutant. This is because the relative size of the friction coefficient parallel and perpendicular to the cell's axis affects how the cells tend to be oriented close to the colony front: if the perpendicular coefficient

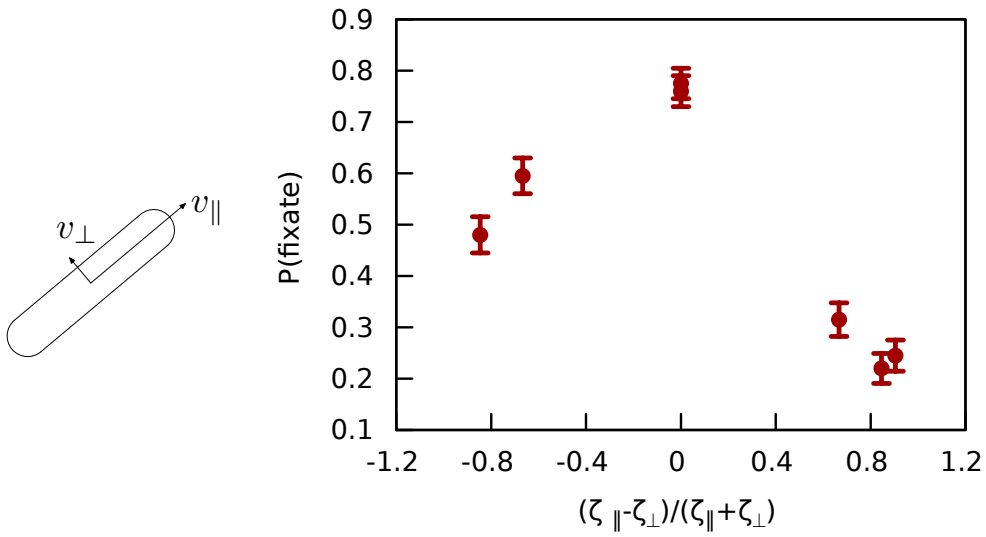

Figure 5.10: Probability of fixation of a beneficial mutant for different levels of friction anisotropy. The parameter used to measure anisotropy is the relative difference between the friction coefficients along the cells' two axes, $(\zeta_\parallel - \zeta_\perp)/(\zeta_\parallel + \zeta_\perp)$. P(fixate) was estimated from the multiple-mutant, fixed initial condition simulation method. As before, $L = 100\mu$m, $s = 0.05$.

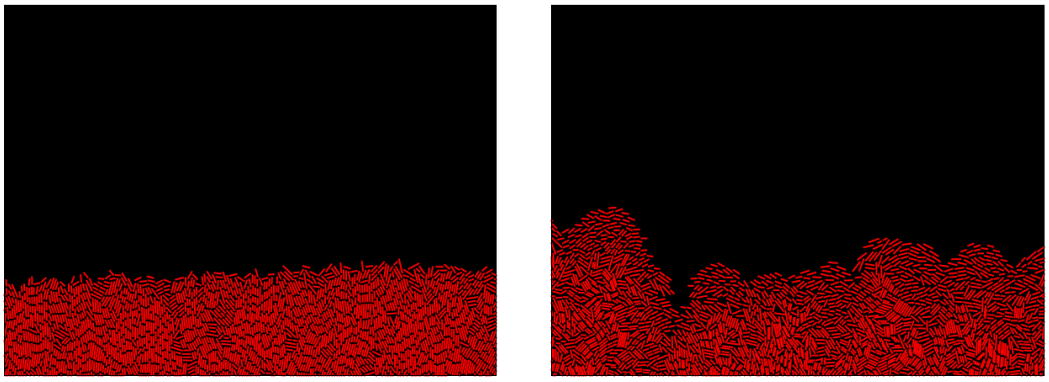

Figure 5.11: Snaphots of a growing colony with isotropic friction, as previously, $\zeta_\parallel = \zeta_\perp = \zeta_r = 1.0$ (left), and with very anisotropic friction, $\zeta_\parallel = 10.0$, $\zeta_\perp = 0.25$ and $\zeta_r = 3.0$ (right).

is larger thay will tend to orient with their axis parallel to the direction of motion, and vice versa. This in turn affects the roughness of the front and the wandering of boundaries between sectors. The fixation probability is much reduced if the friction is anisotropic in either direction, with the effect larger if $\zeta_\parallel > \zeta_\perp$. Figure 5.11 shows a comparison between a colony where the friction

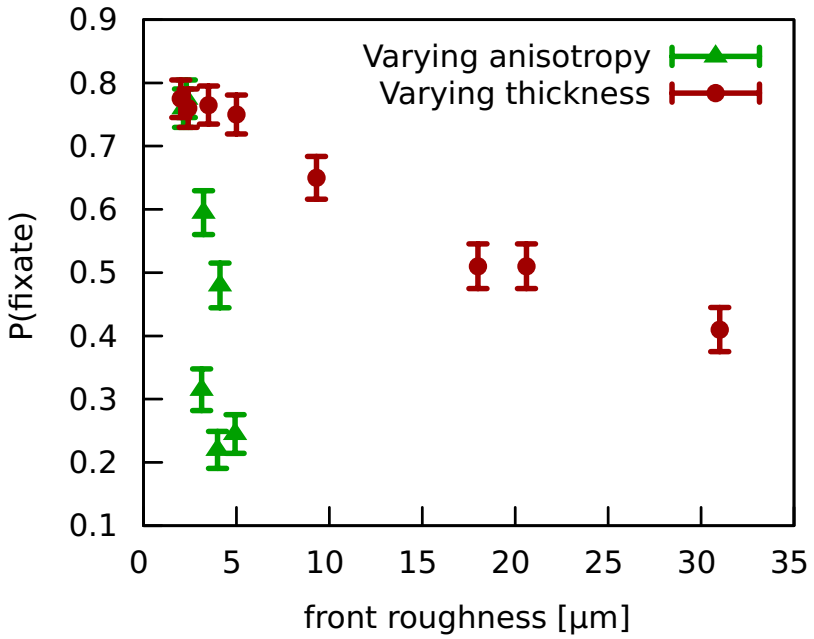

Figure 5.12: Probability of fixation of a beneficial mutant plotted against front roughness. Red points are the same as in Fig. 5.6B, with the roughness being varied by changing the initial nutrient concentration oand therefore the thickness of the growing layer. For the green points, the change in roughness arises from changing the friction anisotropy (data is the same as in Fig. 5.10).

coeffeicient along the cell's axis, $\zeta_{\parallel}$, is much larger that $\zeta_{\perp}$, by a factor of 12, and a colony with isotropic friction as in previous simulations. In the anisotropic case, the cells are significantly more oriented edge-on to the colony, and the roughness is noticeably larger. Such a situation, with $\zeta_{\parallel} > \zeta_{\perp}$ might occur, for example, if cells are able to 'roll' along a surface. Fig. 5.12 shows the same data as above plotted against front roughness rather than anisotropy ratio, along with the fixation probabilities plotted against roughness when the latter is varied by varying the front thickness. Note that while making the friction anisotropic does increase the roughness of the colony front, the reduction in the fixation probability is much greater than would be expected due to the roughness alone, indicating that anisotropy has an effect beyond simply increasing front roughness.

Another simple mechanical feature to vary is the shape of the cells. There is reason to believe this might change the behaviour, since it is observed experimentally that colonies composed of yeast cells, which are round rather than rod-shaped, have many more sectors than colonies of *E. coli* [66]. I therefore

ran simulations with cells of different aspect ratios, ranging from cells much longer than typical *E. coli* cells to cells with a maximal aspect ratio of 2:1 and estimated fixation probabilities as before, see Fig. 5.13. The results show that cell shape does indeed affect fixation probability; however this appears to be an indirect effect due to the cell shape affecting the roughness of the front. If the data are plotted against roughness along with the previous data where $P(\text{fixate})$ was plotted against roughness by varying c_0, they fall onto approximately the same line, in constrast to the case of friction anisotropy, where the effect on fixation probabilities was larger than would be expected based on the change in the roughness of the front.

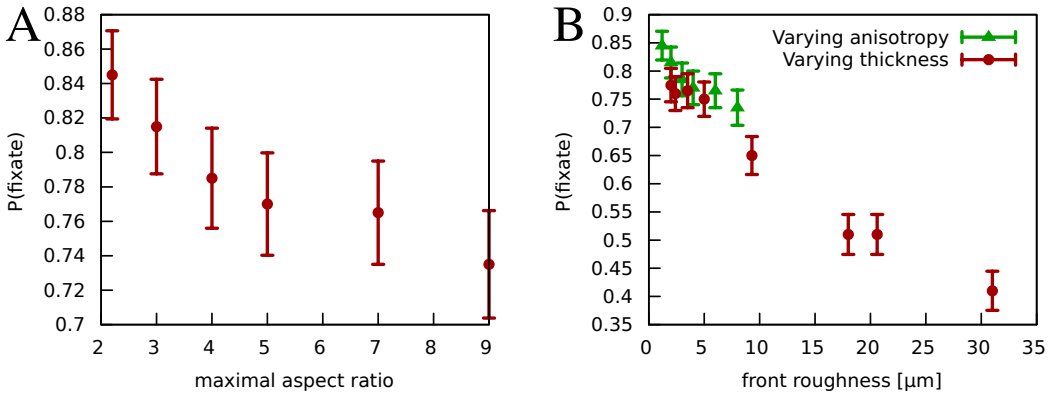

Figure 5.13: A: probability of fixation against maximal aspect ratio of the cells (that is, their aspect ratio just before splitting). B: the same data as in A plotted against the roughness of the front, which also varies with aspect ratio. This is plotted alongside data obtained by instead varying the thickness of the growing front, as before, for comparison. Note that the points appear to fall roughly onto the same line.

5.2.4 Dependence on fitness advantage of the mutant

As mentioned above, the large amount of genetic drift in an expanding colony means that we expect the fixation probability of a mutant cell will be much reduced compared to the well-mixed case. To demonstrate this, I estimated the fixation probability in our model as a function of the fitness advantage s (Fig. 5.14). The probability of fixation is significantly smaller than the well-mixed result $s/(1+s)$, which one obtains for example in the Moran model of competition between individuals without spatial structure, if one individual is

given a fitness advantage s [141]. This is simply because cells born anywhere but at the very front of the colony are very unlikely to go on to fixate, as described in Section 5.2.1. Note that the fixation proabability appears to be linear in s for small s. This contrasts with the theory described in [67] (see Fig. 5.15), which predicts that the probability of fixation of a beneficial mutation should be proportional to $\sqrt{s}$. This theory only considers mutants born at the colony edge, and models the expanding mutant sector as undergoing a random walk, biased to increase in size by a factor proportional to $\sqrt{s}$ due to the geometry of the expanding sector.

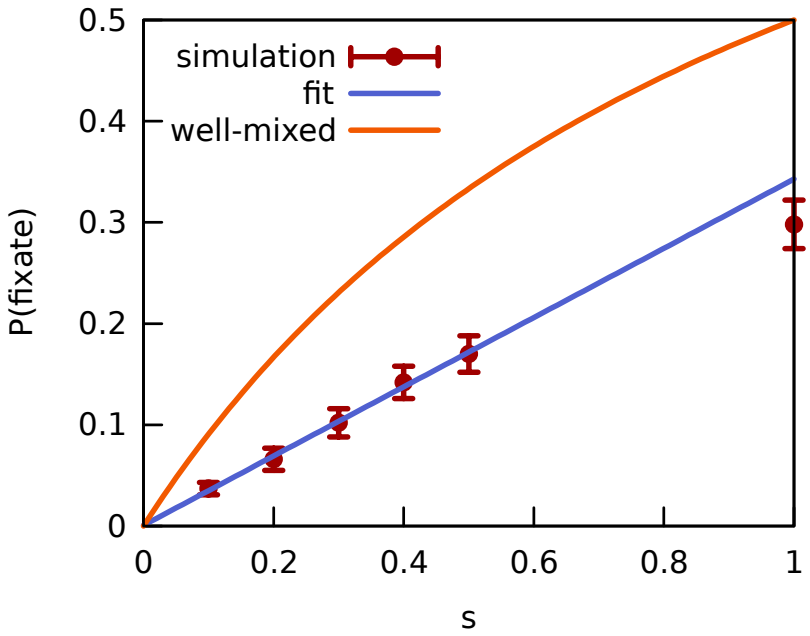

Figure 5.14: Probability of fixation in our simulations as a function of fitness advantage s, with a straight line fit to the simulation data. Also plotted is the theoretical result for the probability of fixation of a mutant with fitness advantage s in the well-mixed case, $s/(1+s)$. These simulations were done in the comoving frame, with $L = 100\mu$m and front thickness 14μm.

To explore this discrepancy, I performed experiments on beneficial mutants under a few simpler population models (see Fig. 5.16). The first is the Moran model, a very common model in population genetics [141, 142], in which there are N individuals and at each time step a random individual is chosen to die; an individual is chosen to replace it with probability proportional to fitness. This model has been very well studied, and the result as mentioned above is that the

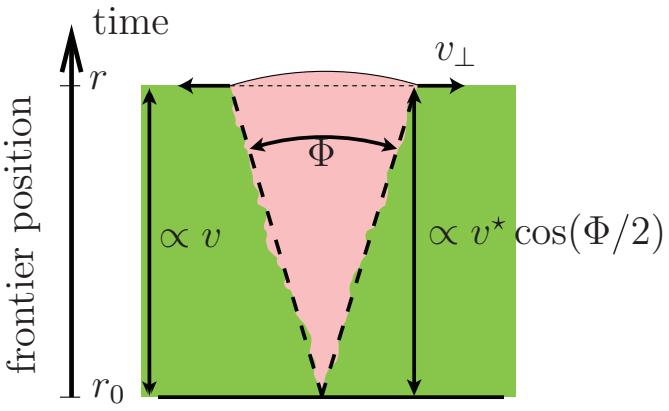

Figure 5.15: Diagram showing the dynamics of a mutant sector with fitness advantage s according to the theory in [67] (reproduced from that paper). Ignoring stochasticity, the mutant sector forms a cone shape (a sector of a circle) as it grows, with opening angle Φ. Due to the geometry, the speed with which the sector expands in the direction perpendicular to the front is given by $v_\perp = \tan[\arccos(\Phi)] \sim \sqrt{s}$. The stochasticity is included by assuming that the sector boundaries perform a random walk along the edge of the colony, with a bias given by $v_\perp$ towards expansion. The probability of fixation is then proportional to $\sqrt{s}$.

fixation probability is approximately $s/(1+s)$ for small s. The second model is a simple model of an expanding population, where we consider a line of cells on a lattice (Fig. 5.16, left). Each time step, the entire colony moves forward one space in the lattice, with each empty space being filled by one of its three neighbours in the current layer, with each of these cells being chosen with a probability proportional to its fitness. Note that it is only necessary to simulate a single layer - this model is equivalent to a one-dimensional population. Finally, I use the Eden model, a stochastic lattice model of a growing population (Fig. 5.16, right), in which at every timestep a cell with at least one empty neighbour site is chosen to reproduce and fills an empty neighbour site at random. Again, the cell which reproduces is chosen weighted by fitness. Fig. 5.17 shows the results of these models for the fixation probability of a beneficial mutant with fitness advantage s, as a function of s. As in the agent-based model, these probabilites are calculated by running an experiment in which a single mutant is introduced many times and measuring the proportion of cases in which it fixates.

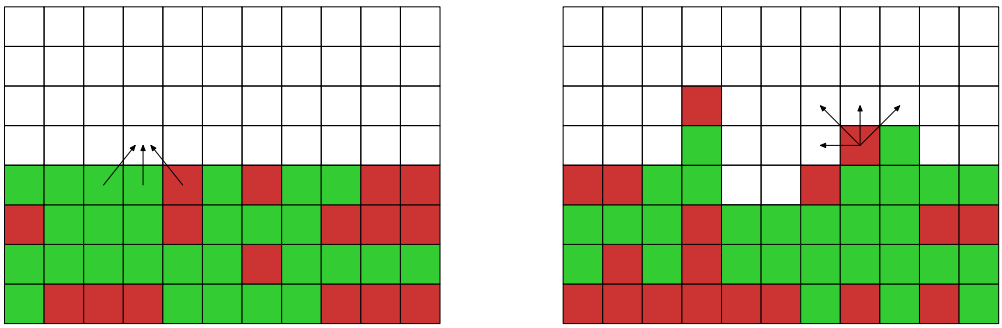

Figure 5.16: Diagrams of the two simple lattice models of colony growth. Left: the one-dimensional model. Each lattice site in the first empty row is filled with one of its three neighbours in the top filled layer. Right: the Eden model. At each time step, a filled site with at least one empty neighbour is chosen at random, and fills one of its empty neighbours.

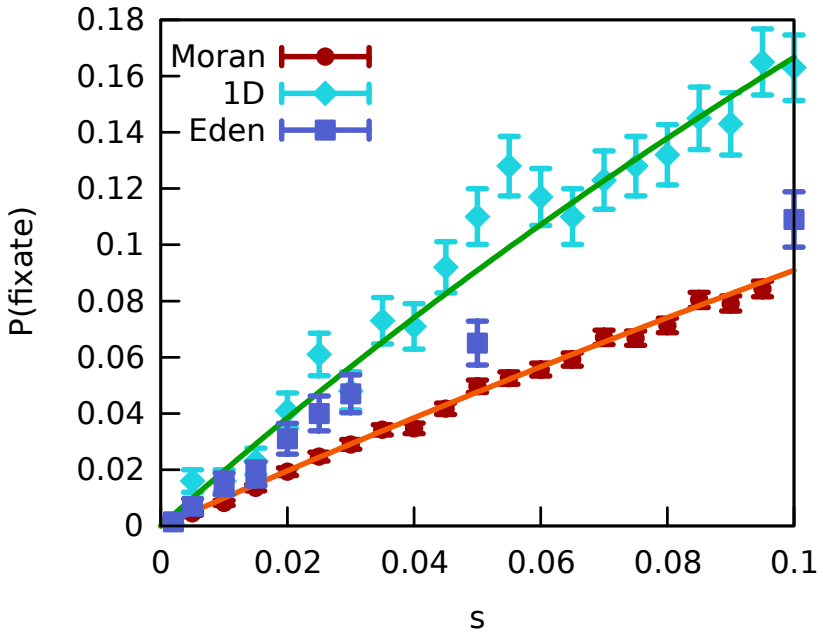

Figure 5.17: Probability of fixation in the Moran, one-dimensional and Eden models. Orange line is the well-mixed (Moran model) prediction, $P_{fix} = s/(1+s)$, green line is $P_{fix} = 2s/(1+2s)$.

The results show that both the Eden model and the one-dimensional model still appear to have fixation probability roughly proportional to s for small s, rather than $\sqrt{s}$. In the 1D case, we would expect this since the bias of the random walk undergone by the mutant sector is itself proportional to s in this case, since

the mutant sector is simply a triangle rather than a sector of a circle; it does not 'bulge outwards'. It is interesting to note that for small s the Eden model fixation probability is very close to that of the 1D model, suggesting that the ability of the front to deviate from being flat does not affect this probability. The red points show the results of the ordinary Moran model, along with the well-known result that $P_{fix} = s/(1+s)$ for small s in this model (orange line). Note that for small s, the Eden and 1D models both fit well to $P_{fix} = 2s/(1+2s)$, the result for a Moran model with a fitness advantage twice as large. It is also interesting that a beneficial mutant in an expanding colony (under any of these models) actually has a significantly *higher* chance of fixating than in the well-mixed case *provided that it is born right at the colony edge*.

As for why the prediction of the theory that $P_{fix} \approx \sqrt{s}$ does not hold, there are two possible explanations. One is that the coarse-grained random-walker theory does not hold when there are only a few cells, i.e. soon after the mutant is born, and this period is crucial to whether or not a mutant will go on to fixate. Another is the fact that the theory does not include any stochasticity in the direction perpendicular to the front, which is certianly present in both the Eden and agent-based models, where the colony front is significantly irregular.

5.3 Conclusions

In this chapter I have described how our biophysical simulation model of growing bacterial colonies can be used to study problems in the evolution of expanding populations. Inspired by experimental work on neutral evolution and selection, I used the model to investigate the rate of fixation of beneficial mutations in a growing colony. Recent experiments have indicated that the morphology of the colony can affect this rate, so I looked at the effect of varying colony morphology (the roughness of the front) on the fixation probability, by varying the concentration of nutrient. This was somewhat complicated by the fact that changing the concentration changes the thickness of the growing layer of cells as well, and these two factors seemed to have competing effects: on one hand a thicker layer (associated with a smoother front) will reduce the fixation rate as more cells will be born far from the colony front and have very little chance to fixate, however on the other hand the smoothness will increase the probability.

To disentangle these effects, I ran simulations starting with a given proportion of fitter mutant cells, rather than a single cell, and measured the probability that mutant cells took over the front. The thickness does not affect this probability, as the mutant cells are evenly spread throughout the layer to begin with (so, for example, the number of mutants right at the edge will not depend on the thickness). From these simulations, I indeed found that the probability of fixation goes down for rougher fronts. This is in agreement with the results of preliminary experiments done by the group of Oskar Hallatschek. It can be understood by considering that the size of a mutant sector undergoes a random walk as its boundaries wander as the colony grows, with a bias to increase due to the fitness advantage. If the front of the colony is rougher, the boundaries will wander more, reducing the effectiveness of the bias in preventing extinction early on, and therefore the fixation probability. This explanation is supported by the fact that the colony roughness also has a strong effect on how quickly the number of sectors decays in the neutral case where differently labelled cells have no fitness difference, with rougher fronts leading to much faster decay.

I also looked at the effects of other parameters involved in our simulation model on the rate of fixation of mutations. The first main result here was that reducing the aspect ratio of the cells increases the fixation probability, and that this is due to a reduction in the roughness of the front. Secondly, altering the frictional force which acts on the cell so that it depends on the direction of the force relative to the cell's axis significantly affects the fixation probability, and this effect is greater than would be expected from the effect on the roughness; this frictional anisotropy seems to increase the amount of genetic drift (extent of sector boundary wandering) in itself, not just by making the front rougher.

Looking again at the fixation of individual mutants, I found that the proabaility that a single mutant born at random in the growing layer will fixate is reduced compared to the well-mixed result, due to the fact that any cell born anywhere but at the very edge (first line of cells) has a very small probability of fixating, since it is very difficult for a cell to 'push through' into the uncolonized space. I also found that the fixation proabaility appears to be linear in the fitness advantage, condtradicting a previous theory which predicted a square-root dependence.

Chapter 6

Conclusions

In this Thesis I have described various models of active matter. These models are used to model biological systems, in particular collections of bacteria, although they are applicable to other systems, such as collections of actin fibres and molecular motors, or animal tissues.

Inspired by the Vicsek model of flocking behaviour and recent work on chemotactic pattern formation in bacterial colonies, I first described a model of collective behaviour where agents move around in a two dimensional space, tend to align their direction of motion with neighbours, and slow down in response to a high local density of agents. Using agent-based simulations, I showed that this model leads to novel pattern formation effects, in particular the formation of coherently moving clusters and high-density 'lanes'. To explore these effects further, we derived approximate coarse-grained 'hydrodynamic' equations describing the model, and analysed the instabilities of these equations both analytically and numerically, achieving fairly good agreement with the results of the simulations.

I then went on to describe a rather different model of bacterial colonies, this time modelling the growth of colonies made up of non-motile cells growing on a surface (biofilms). In contrast to previous models of growth and pattern formation based on Fisher-Kolmogorov equations, we used a fairly detailed biophysical simulation model whereby cells are modelled as rigid rods which grow along their axes, divide, and physically push upon each other as they grow, with the growth limited by a nutrient which is consumed by the cells. These simulations, combined with a continuum theory treating the colony as a kind of actively growing fluid,

yielded some interesting behaviour different from previous models, such as that a colony growing in two dimensions cannot grow at a constant speed unless it either forms branches or the cells in the centre of the colony become compressed. We also posit a new explanation of the often-observed transition of colony morphology between roughly round and branched structures, as being caused by the balance between uptake and consumption of nutrients by the cells: if the density of nutrients is less than that required to produce the density of biomass of cells at close packing, the colony must form branches.

Finally, I used the above-described model of bacterial colony growth to model selection and competition between cells in growing colonies. This was inspired by recent work by Oskar Hallatschek and others on evolution in expanding populations. The expansion of a population into new territory has some interesting effects on evolution, since the colonization of empty space leads to constant population bottlenecks as only a few cells close to the expanding frontier are able to pass on their offspring. This leads to a 'genetic demixing' effect whereby there are large areas of individuals which are genetically similar since they all share a common ancestor which was able to colonize the new space. We looked at the effect this had on selection, and in particular on the fixation of beneficial mutations, which might for example correspond to antibiotic resistance in a bacterial colony. Our first main result here is that selection is less effective than in the well-mixed case due to the fact that mutants born anywhere but exactly at the colony edge have almost no chance of reaching fixation. Secondly, the morphology of the colony can have effects on the rate of fixation of beneficial mutations, with selection being less effective for colonies which have more irregular shapes due to the larger amount of genetic drift.

These projects have various avenues for further exploration. Recent experimental results on collections of molecular motors and actin fibres *in vitro* have shown behaviours, such as moving clusters and lanes, which seem to be similar to those in our model. These systems contain the crucial ingredients of our model: alignment and density-dependent speed (both due to steric/crowding effects). It would be interesting to analyse in more detail whether these effects indeed have the same origin as in our model, perhaps by looking at how the patterns formed depend on factors such as the density of fibres, and by looking in detail at how the average speed of propulsion of the fibres depends on their density.

For the work on mechanical growth of bacterial colonies, it would be interesting to analyse how much the results can be extended to the growth of animal tissues, for example the early growth of a tumour (prior to angiogenesis), which similarly involves a growing collection of cells pushing each other outwards and limited in their growth by the diffusion of factors needed for growth (in particular oxygen). To do this it would be interesting to consider the effects of pressure-dependent growth rates, as outlined at the end of Chapter 4, and also to run simulations in three dimensions, since tumours often grow in spheroids. This would also be interesting as in this case the effect where cells 'pop out' of the plane as they do in 2D growth would not be present, and would represent an alternative three-dimensional version of our model which is more similar to the two-dimensional case.

On the experimental side, it would be very interesting to attempt to validate our results on growth in the two- and quasi-three-dimensional cases. For example, cells could be forced to truly grow in two dimensions using a microfluidic device, in order to test our prediction that the cells ought to become physically compressed in the centre of the colony if nutrient is plentiful; we could test our results relating the density of cellular biomass within the colony to the nutrient concentration. Another avenue would be to use three-dimensional spheroids, either of bacterial or animal cells, as this would also avoid the complication of cells popping out of the plane.

There is still work to be done understanding our results on fixation of mutations in growing colonies. In particular, we still do not fully understand the reason for the discrepancy between the random-walker theory and our simulation results on the dependence of the fixation probability and the fitness advantage of the mutants. We believe that it is due to the stochasticity in the direction perpendicular to the colony front, which is not included in the random-walker theory. To test this we could use a model which has no such stochasticity, but this has so far proved very difficult. Experimental work analysing the effect of colony morphology on the fixation of mutants is currently underway. It would also be very interesting to look at the depencence of rates of fixation on fitness advantage experimentaly, although this is rather difficult as it requires either finding or engineering mutants with a range of fitness advantages (growth rates) over the wild type.

Appendix A

Derivation of Boltzmann equation describing the flying XY model

In this Appendix, I derive the Boltzmann-like equation describing the dynamics of the flying XY model used in Chapter 2 to derive hydrodynamic equations for that model. The idea is to derive a stochastic field equation for the quantity $f(\mathbf{r},\theta) = \sum_{j=1}^{N} \delta(\mathbf{r}-\mathbf{r}_j)\delta(\theta-\theta_j)$, which is the density of particles at position $\mathbf{r}$ with angle θ. To derive the time evolution of f, we use a method similar to what has been used previously in other contexts, see for example [143, 97].

We start from the equation describing the dynamics of the particles, Eq. 3.3:

$$\dot{r}_i = v\,\mathbf{e}_{\theta_i};\ \dot{\theta}_i = \gamma \sum_j F(\theta_j-\theta_i, r_j-r_i) + \sqrt{2\epsilon}\tilde{\eta}_i(t). \tag{A.1}$$

Now, consider a function $g(\mathbf{r}_i,\theta_i)$. Using Itō's Lemma to calculate the derivative of a function of a stochastic variable ([144], [145] Sections 4.1-2), its time derivative is given by

$$\dot{g} = (\nabla_i g)\cdot\dot{\mathbf{r}}_i + \frac{\partial g}{\partial\theta_i}\cdot\dot{\theta}_i + \epsilon\frac{\partial^2 g}{\partial\theta_i^2} \tag{A.2}$$

where ∇_i is the gradient with respect to the coordinate $\mathbf{r}_i$. Using (A.1), this reads

$$\dot{g} = (\nabla_i g)\mathbf{v}_i + \frac{\partial g}{\partial\theta_i}\big[\gamma\sum_j F(\theta_i-\theta_j,\mathbf{r}_i-\mathbf{r}_j) + \sqrt{2\epsilon}\eta_i\big] + \epsilon\frac{\partial^2 g}{\partial\theta_i^2} \tag{A.3}$$

We can rewrite this as

$$\dot{g} = \int d\mathbf{r}d\theta f_i(\mathbf{r},\theta)\Big[\mathbf{v}\nabla g + \frac{\partial g}{\partial\theta}\big[\gamma\sum_j F(\theta-\theta_j,\mathbf{r}-\mathbf{r}_j) + \sqrt{2\epsilon}\eta_i\big] + \epsilon\frac{\partial^2 g}{\partial\theta^2}\Big] \quad \text{(A.4)}$$

where $f_i(\mathbf{r},\theta) = \delta(\mathbf{r}-\mathbf{r}_i)\delta(\theta-\theta_i)$, so that $f(\mathbf{r},\theta) = \sum_i f_i$. Integrating by parts, this becomes

$$\dot{g} = \int d\mathbf{r}d\theta\Big[-\nabla(f_i\mathbf{v}) - \frac{\partial}{\partial\theta}\big[\gamma f_i\sum_j F(\theta-\theta_j,\mathbf{r}-\mathbf{r}_j) + \sqrt{2\epsilon}f_i\eta_i\big] + \epsilon\frac{\partial^2 f_i}{\partial\theta^2}\Big]g \quad \text{(A.5)}$$

We can now use the two identities

$$\begin{aligned}\dot{g}(\mathbf{r}_i(t),\theta_i(t)) &= \frac{\mathrm{d}}{\mathrm{d}t}\int d\mathbf{r}d\theta f_i(\mathbf{r}-\mathbf{r}_i(t),\theta-\theta_i(t))g(\mathbf{r},\theta)\\ &= \int d\mathbf{r}d\theta\dot{f}_i(\mathbf{r}-\mathbf{r}_i,\theta-\theta_i)g(\mathbf{r},\theta)\end{aligned} \quad \text{(A.6)}$$

and

$$F(\mathbf{r}-\mathbf{r}_j,\theta-\theta_j) = \int d\mathbf{r}'d\theta' f_j(\mathbf{r}',\theta')F(\mathbf{r}-\mathbf{r}',\theta-\theta') \quad \text{(A.7)}$$

to write (A.5) as

$$\begin{aligned}&\int d\mathbf{r}d\theta\dot{f}_i\, g(\mathbf{r},\theta) = \int d\mathbf{r}d\theta g(\mathbf{r},\theta)\Big[-\nabla(f_i\mathbf{v})\\ &-\frac{\partial}{\partial\theta}\big[\gamma\int d\mathbf{r}'d\theta' f_i(r,\theta)\sum_j F(\theta-\theta',\mathbf{r}-\mathbf{r}')f_j(\mathbf{r}',\theta') + \sqrt{2\epsilon}f_i\eta_i\big] + \epsilon\frac{\partial^2 f_i}{\partial\theta^2}\Big]\end{aligned} \quad \text{(A.8)}$$

Since this holds for any function g, one gets (after a sumation over i)

$$\begin{aligned}\dot{f}(\mathbf{r},\theta) &= -\nabla[f(\mathbf{r},\theta)\mathbf{v}] - \gamma\frac{\partial}{\partial\theta}\int d\mathbf{r}'d\theta' f(\mathbf{r},\theta)F(\theta-\theta',\mathbf{r}-\mathbf{r}')f(\mathbf{r}',\theta')\\ &+\epsilon\frac{\partial^2}{\partial\theta^2}f(\mathbf{r},\theta) - \frac{\partial}{\partial\theta}\sqrt{2\epsilon}\Lambda(\mathbf{r},\theta)\end{aligned} \quad \text{(A.9)}$$

where $\Lambda(\mathbf{r},\theta)$ is a gaussian white noise that has the same statistics as $\sum_i \eta_i f_i$,

that is

$$\begin{aligned}\langle \Lambda(\mathbf{r},\theta,t)\Lambda(\mathbf{r}',\theta',t')\rangle &= \sum_{i,j} f_i(\mathbf{r},\theta;t) f_j(\mathbf{r}',\theta';t')\delta_{ij}\delta(t-t') \\ &= \sum_i f_i \delta(\mathbf{r}'-r_i)\delta(\theta'-\theta_i)\delta(t-t') \\ &= f(\mathbf{r},\theta)\delta(\mathbf{r}'-\mathbf{r})\delta(\theta'-\theta)\delta(t-t')\end{aligned} \tag{A.10}$$

Finally, equation (A.9) can be written as

$$\begin{aligned}\dot{f}(\mathbf{r},\theta) = -\nabla\cdot[f(\mathbf{r},\theta)\mathbf{v}] - \gamma\frac{\partial}{\partial\theta}\int d\mathbf{r}' d\theta' f(\mathbf{r},\theta)F(\theta-\theta',\mathbf{r}-\mathbf{r}')f(\mathbf{r}',\theta') \\ + \epsilon\frac{\partial^2}{\partial\theta^2}f(\mathbf{r},\theta) - \frac{\partial}{\partial\theta}\sqrt{2\epsilon f(\mathbf{r},\theta)}\eta(\mathbf{r},\theta,t)\end{aligned} \tag{A.11}$$

where $\eta(\mathbf{r},\theta,t)$ is a Gaussian white noise of unit variance. The first term on the RHS describes advection of particles, and crucially has the particle velocity $\mathbf{v}$ inside the gradient; this is very important to describe the self-trapping effect. The second term is the 'collision' term describing interactions between particles, and the third describes the diffusion of each particle's orientation over time due to the noise ϵ. Finally, the last term on the RHS is a noise term, which we ignore as we go on to derive hydrodynamic eqution in Chapter 3; including it would lead to a set of stochastic hydrodynamic equations describing the system.

Appendix B

Linear stability analysis of hydrodynamic equations

In this Appendix I perform some linear stability analysis on the hydrodynamic equations derived in Chapter 3 for the flying XY model with density-dependent motility. These equations are

$$\Rightarrow \partial_t \rho = -\nabla \cdot (v\rho \mathbf{P}) \tag{B.1}$$

$$\begin{aligned}\partial_t \mathbf{W} + \frac{\gamma}{16\epsilon}(\mathbf{W}\cdot\nabla)(v\mathbf{W}) = (\frac{1}{2}\gamma\rho - \epsilon)\mathbf{W} - \frac{\gamma^2}{8\epsilon}W^2\mathbf{W} - \frac{1}{2}\nabla(v\rho) + \\ \frac{3\gamma}{16\epsilon}\nabla(vW^2) - \frac{\gamma}{32\epsilon}v\nabla W^2 - \frac{3\gamma}{16\epsilon}\mathbf{W}\nabla\cdot(v\mathbf{W}) - \frac{\gamma}{8\epsilon}v\mathbf{W}(\nabla\cdot\mathbf{W}) - \frac{\gamma}{8\epsilon}v(\mathbf{W}\cdot\nabla)\mathbf{W} \\ + \frac{1}{16\epsilon}\left[(\nabla\cdot(v\nabla))(v\mathbf{W}) + (\nabla v\cdot\nabla)(v\mathbf{W}) - (\nabla v)\nabla\cdot(v\mathbf{W})\right]\end{aligned} \tag{B.2}$$

In Chapter 3 I performed linear stability analysis on these in some simple cases; here I show the more general case, when we are in the ordered phase and allow spatial fluctuations. We first linearize around the homogeneous solution by setting $\mathbf{W} = W_0\hat{\mathbf{x}} + \delta\mathbf{W}$ and $\rho = \rho_0 + \delta\rho$, where $W_0 = \sqrt{8\epsilon(\epsilon_c - \epsilon)/\gamma^2}$, to obtain:

$$\partial_t \delta\rho = -v(\nabla\cdot\delta\mathbf{W}) - v' W_0 \partial_x \delta\rho \tag{B.3}$$

$$\partial_t \delta\mathbf{W} = (\epsilon_c - \epsilon)\delta\mathbf{W} - \frac{\gamma^2 W_0^2}{8\epsilon}\delta\mathbf{W} - \frac{\gamma^2 W_0^2}{4\epsilon}\hat{\mathbf{x}}\delta W_x$$
$$+ \frac{1}{2}[\gamma\mathbf{W}_0 - V\nabla + \frac{3\gamma W_0^2}{8\epsilon}v'\nabla - \frac{\gamma W_0^2}{2\epsilon}v'\hat{\mathbf{x}}\partial_x]\delta\rho - \frac{3\gamma W_0}{16\epsilon}v\partial_x\delta\mathbf{W} + \frac{5\gamma W_0}{16\epsilon}v\nabla\delta W_x$$
$$- \frac{5\gamma W_0}{16\epsilon}v\hat{\mathbf{x}}(\nabla\cdot\delta\mathbf{W}) + \frac{1}{16\epsilon}[v^2\nabla^2\delta w + W_0\hat{\mathbf{x}}vv'\nabla^2\delta\rho + vv'W_0\hat{\mathbf{x}}(\nabla\partial_x\delta\rho)] \tag{B.4}$$

where we have defined $v = v(\rho_0)$, $v' = v'(\rho_0)$ and $V = v + \rho_0 v'$. Fourier transforming and expressing these eqautions in terms of components, we get

$$\partial_t\delta\rho = -iv\mathbf{q}\cdot\delta\mathbf{W} - v'W_0 iq_x\delta\rho \tag{B.5}$$

$$\partial_t\delta W_x = -2(\epsilon_c - \epsilon)\delta W_x + \frac{1}{2}\left[\gamma W_0 - Viq_x - \frac{\gamma W_0^2}{8\epsilon}v'iq_x\right]\delta\rho + \frac{\gamma W_0}{8\epsilon}viq_x\delta W_x -$$
$$\frac{5\gamma W_0}{16\epsilon}v(i\mathbf{q}\cdot\delta\mathbf{W}) - \frac{1}{16\epsilon}\left[v^2(q_x^2+q_y^2)\delta W_x + vv'W_0(q_x^2+q_y^2)\delta\rho + W_0vv'\delta\rho[q_x^2+q_xq_y]\right] \tag{B.6}$$

$$\partial_t\delta W_y = -\frac{iq_y}{2}\left[V - \frac{3\gamma W_0^2}{8\epsilon}v'\right]\delta\rho - \frac{3\gamma W_0}{16\epsilon}viq_x\delta W_y + \frac{5\gamma W_0}{16\epsilon}viq_y\delta W_x - \frac{1}{16\epsilon}v^2(q_x^2+q_y^2)\delta W_y \tag{B.7}$$

We will analyze these equations by considering three different cases: fluctuations in the x-direction (the direction of $\mathbf{W}$) when v is constant, fluctuations in the x-direction when v is not constant, and fluctuations in the y-direction. When v is constant, it is well-known that the flocking state is unstable to the formation of bands like those in Fig. 3.3 (phase b). This instability has been found in similar hydrodynamic equations of flocking models in [16] and [13]. If $q_y = 0$, we have

$$\partial_t\delta\rho = -ivq\delta W_x - v'W_0 iq\delta\rho \tag{B.8}$$

$$\partial_t\delta W_x = -2(\epsilon_c - \epsilon)\delta W_x + \frac{1}{2}\left[\gamma W_0 - Viq - \frac{\gamma W_0^2}{8\epsilon}v'iq\right]\delta\rho - iqv\frac{3\gamma W_0}{16\epsilon}\delta W_x \tag{B.9}$$

$$\partial_t\delta W_y = -\frac{3\gamma W_0}{16\epsilon}viq\delta W_y \tag{B.10}$$

Now δW_y is decoupled and we can simply examine the other two equations. We look for solutions of the form $\delta\rho$,$\delta\mathbf{W} \sim e^{s(\mathbf{q})t}$. An instability exists if $\Re[s(\mathbf{q})] > 0$ for any $\mathbf{q}$. When v is constant, the eigenvalue equation reads

$$s^2 + s\left[2(\epsilon_c - \epsilon) + ivq\frac{3\gamma W_0}{16\epsilon}\right] + \frac{ivq}{2}(\gamma W_0 - ivq) = 0 \tag{B.11}$$

giving, to second order in q,

$$s_+ = -iqvW_0\frac{\gamma}{4(\epsilon_c-\epsilon)} - \frac{q^2v^2}{4(\epsilon_c-\epsilon)}\left(\frac{7}{4}-\frac{\epsilon}{\epsilon_c-\epsilon}\right) \tag{B.12}$$

$$s_- = -2(\epsilon_c-\epsilon) + iq\frac{vW_0}{2}\left(1-\frac{3\gamma}{8\epsilon}\right) + ... \tag{B.13}$$

The mode s_+ can become unstable when $\frac{7}{4}-\frac{\epsilon}{\epsilon_c-\epsilon} < 0$, corresponding to $\frac{7}{11}\epsilon_c < \epsilon < \epsilon_c$. The banding instability takes place as soon as the order-disorder transition has occurred, but does not extend down to vanishingly small noise, in broad agreement with the microscopic simulation results, and previous work on the banding instability.

We now consider the case where v is not constant, in which case the eigenvalue equation is

$$s^2+s\left[2x+iqW_0v'+ivq\frac{3\gamma W_0}{16\epsilon}\right]+iqW_0v'\left(2x+iqv\frac{3\gamma W_0}{16\epsilon}\right)+\frac{ivq}{2}\left(\gamma W_0-iqV-iqv'\frac{x}{\gamma}\right)=0 \tag{B.14}$$

where we have defined $x = \epsilon_c-\epsilon$. Choosing a particular form for $v(\rho)$, $v = v_0e^{-\lambda\rho}$, the solutions are given by:

$$s_+ = -iqvW_0\left(\frac{\gamma}{4(\epsilon_c-\epsilon)}+v'\right) - \frac{q^2v^2}{4x}\left[\frac{7}{4}-\frac{\epsilon}{\epsilon_c-\epsilon}-\frac{\lambda}{\gamma}(3\epsilon_c-5\epsilon)\right] \tag{B.15}$$

$$s_- = -2x + ... \tag{B.16}$$

Writing $\epsilon^* = \epsilon/\epsilon_c$ and $\lambda^* = \lambda\rho_0$, we find that this mode is unstable in the following regions:

- for $0 < \epsilon^* < \frac{3}{5}$ unstable for $\lambda^* > \frac{(7-11\epsilon^*)/2}{(1-\epsilon^*)(3-5\epsilon^*)} \equiv \lambda_L^*$
- for $\frac{7}{11} < \epsilon^* < 1$ unstable for $\lambda^* < \lambda_L^*$

The first condition shows that for small ϵ the longintudinal instability can appear for large enough λ. The second condition shows that for larger ϵ, when this instability exists even for $\lambda = 0$, it is actually *suppressed* for large enough λ. This effect may be visible in the simulations, in the slope of the line separating phases a and b in Fig. 3.3, but is very subtle.

Finally, we consider fluctuations perpedicular to the direction of motion ($q_x = 0$). In this case the equations are

$$\partial_t \delta\rho = -ivq\delta W_y \tag{B.17}$$

$$\partial_t \delta W_x = -2(\epsilon_c - \epsilon)\delta W_x + \frac{1}{2}\gamma W_0 \delta\rho - \frac{5\gamma W_0}{16\epsilon} viq\delta W_y \tag{B.18}$$

$$\partial_t \delta W_y = -\frac{iq}{2}\left[V - \frac{3\gamma W_0^2}{8\epsilon}v'\right]\delta\rho + \frac{5\gamma W_0}{16\epsilon} viq\delta W_x \tag{B.19}$$

We assume the δW_x mode relaxes since $\epsilon_c > \epsilon$, and neglect it. The remaining two equations give modes with dispersion relations

$$s^2 = -q^2\frac{v}{2}\left[V - \frac{3\gamma W_0^2 v'}{8\epsilon}\right] = -\frac{q^2 v}{4}\left[v + \frac{v'\rho}{2}(3\epsilon^* - 1)\right] \tag{B.20}$$

This mode will be unstable if

$$-\frac{\rho v'}{v} > \frac{2}{3\epsilon^* - 1} \tag{B.21}$$

Taking $v = v_0 e^{-\lambda\rho}$, this condition is

$$\lambda^* > \lambda_T^* = \frac{2}{3\epsilon^* - 1}. \tag{B.22}$$

If $v = v_0 e^{-\lambda\rho} + v_1$ for non-zero v_1 Eq. B.21 cannot be solved analytically, but for small enough v_1 there will be a finite range of λ values where the instability exists. This transverse instability should correspond to the 'lanes' seen in simulations (d(ii) in Fig. 3.3).

Appendix C

List of publications

1. F. D. C. Farrell, M. C. Marchetti, D. Marenduzzo, and J. Tailleur. 'Pattern formation in self-propelled particles with density-dependent motility'. Phys. Rev. Lett. 108: 248101, 2012.

2. F. D. C. Farrell, B. Waclaw, D. Marenduzzo, and O. Hallatschek. 'Mechanically driven growth of quasi-two-dimensional microbial colonies'. Phys. Rev. Lett., 111:168101, 2013

Pattern Formation in Self-Propelled Particles with Density-Dependent Motility

F. D. C. Farrell,[1] M. C. Marchetti,[2] D. Marenduzzo,[1] and J. Tailleur[3]

[1]SUPA, School of Physics and Astronomy, University of Edinburgh, Mayfield Road, Edinburgh EH9 3JZ, United Kingdom
[2]Physics Department and Syracuse Biomaterials Institute, Syracuse University, Syracuse, New York 13244, USA
[3]Laboratoire Matiere et Systemes Complexes, Universit Paris Diderot, 75205 Paris, France

(Received 1 February 2012; published 15 June 2012)

We study the behavior of interacting self-propelled particles, whose self-propulsion speed decreases with their local density. By combining direct simulations of the microscopic model with an analysis of the hydrodynamic equations obtained by explicitly coarse graining the model, we show that interactions lead generically to the formation of a host of patterns, including moving clumps, active lanes, and asters. This general mechanism could explain many of the patterns seen in recent experiments and simulations.

DOI: 10.1103/PhysRevLett.108.248101 PACS numbers: 87.18.Gh, 05.65.+b, 47.54.−r, 87.18.Hf

Collections of self-propelled (SP) particles provide the most common realization of active matter, the study of which constitutes a rapidly growing area of research [1]. Examples of SP particles are bacteria, cells [2], and actin filaments ''walking'' on a carpet of immobilized molecular motors [3].

The term ''active'' is used to contrast these systems with their passive counterparts, such as solutions of diffusing Brownian particles. Active systems exhibit a much richer physics, in particular having a far greater tendency to form patterns. For instance, bacterial colonies of *E. coli* or *S. typhimurium* growing in the lab can self-organize into crystalline or amorphous arrangements of high-density bacterial clumps [4], while biofilms form even more elaborate patterns such as microbial honeycombs, essentially hexagonal lattices of low-density voids [5]. Similarly, actin in high density motility assays [3] organize in moving spots, stripes, and traveling waves.

What is the mechanism underlying the formation of these ''active patterns?'' One may expect that, as the underlying constituents of each system are so different, the answer to this question should also be system-specific. If we are to capture all details of a given active pattern, this is indeed likely to be the case. Yet, a fascinating possibility is that there may exist some generic origin of many of these patterns, stemming from a few universal key features of activity, linked to its inherent nonequilibrium nature. In some cases, pursuing such minimal descriptions can be very rewarding. A well-known example is the hydrodynamic theory of flocking proposed by Toner and Tu in [6], which was inspired by the ''agent-based'' model of Vicsek *et al.* [7]. The latter studied the dynamics of an ensemble of SP particles subjected to aligning interactions, whose ultimate origin may be hydrodynamic or collision-dominated in the cases of bacteria and actin filaments, or more complex for bird flocks or fish schools. Universal features successfully predicted by generic flocking models are spontaneous motion [6–8], giant density fluctuations [9,10], and the emergence of complex spatiotemporal active patterns [10,11].

The original Vicsek model considers point particles of fixed speed and includes no interactions between them other than a rule that aligns their velocities. Recently, focus has shifted onto specific models where additional interactions are included, most commonly steric repulsion [12–18]. Our aim here is to develop a more generic model for interacting SP particles. Interactions are incorporated in our model by assuming that the motility of the SP particles is a decreasing function of their local density [19]. One may envisage several physical mechanisms responsible for a decay of the propulsion velocity with density: here we highlight just two. First, such a slowing down may arise due to local crowding and steric hindrance, just as in [13,14,16,17]. An alternative mechanism can be provided by biochemical signaling such as quorum sensing in bacterial colonies, as recently explored theoretically [20] and experimentally [21]. This second mechanism may lead to slowdown even in dilute suspensions. Our work describes the results of simulations of a microscopic SP particles model with both interactions and alignment rule, the derivation of the corresponding hydrodynamic description of the model in terms of a density and a polarization field, and an analysis of the continuum theory. It therefore provides a direct bridge between microscopic and continuum models, which allows us to identify universal mechanisms driving pattern formation in interacting SP particles. As we shall see, interactions lead to an even larger repertoire of patterns in active particle suspensions than obtained in conventional Vicsek models. These include moving clumps, lanes, and asters (i.e., inward pointing defects of the polarization field with topological charge $+1$), and qualitatively match the patterns found experimentally, e.g., in [3].

We consider a modified version of the Vicsek model [7], where N particles in a box of size L^2 (hence, with overall mean density $\rho_0 = N/L^2$) interact via a pairwise aligning forcing, which simplifies the coarse graining of the microscopic model. In 2D the position r_i and direction, identified by an angle θ_i (or a vector $\mathbf{e}_{\theta_i}$), of the ith particle evolve according to

$$\dot{r}_i = v\mathbf{e}_{\theta_i}; \dot{\theta}_i = \gamma \sum_{j=1}^{N} F(\theta_j - \theta_i, r_j - r_i) + \sqrt{2\epsilon}\tilde{\eta}_i(t), \quad (1)$$

where γ and ϵ describe strength of alignment and fluctuations respectively, and $\tilde{\eta}(t)$ is a Gaussian white noise with zero mean and unit variance. F controls the alignment interactions between the spins. For simplicity, we choose $F(\theta, r) = \sin(\theta)/\pi R^2$ if $|r| < R$ (hereafter we restrict to $R = 1$) and 0 otherwise. This simple choice for F enforces polar alignment of the SP particles and will allow us to make progress anaytically, but we expect our results to extend to far more general forms of polar alignment. In the $v \to 0$ limit, our model is an off-lattice analogue of the XY model for a ferromagnet; hence, we call it the flying XY model. Last, a density-dependent velocity is introduced in the model by stipulating that v depends on the number of particles n within a given radius R_n, as $v(n) = v_0 e^{-\lambda n} + v_1$, where $v_0 \gg v_1 > 0$ are the dilute and crowded limiting velocities respectively, and $\lambda > 0$ controls the decay of the motility decreases with increasing density. Hereafter, we restrict to $R_n = R$.

Figure 1(a) shows a representative phase diagram of the flying XY model in the (ϵ, λ) plane for $N = 3000$ [22]. For small λ, when v is quasiconstant, the phases observed are the same as those in the literature on flocking models [7,10]. Namely, at high ϵ we find a disordered, homogeneous state [region c in Fig. 1(a)], followed by a polarly ordered phase with high density stripes [named stripy phase, b, in Fig. 1(a)] below a critical noise value. For even lower ϵ, we observe a "fluctuating flocking state" (region a) with polar order and large density fluctuations—this state is close to the one described in Refs. [10,11], and we do not discuss it further here. All these phases are expected by analogy with the Vicsek model.

Above a critical value $\lambda_c(\epsilon)$, new patterns appear. Due to the density-dependent motility, the SP particles cluster via

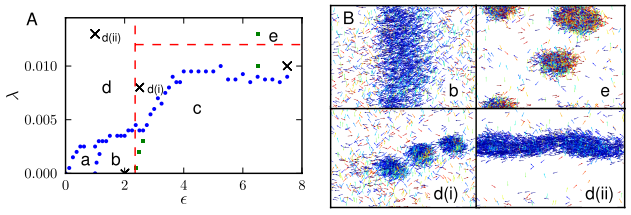

FIG. 1 (color online). (A) Phase diagram in the (ϵ, λ) plane, for $N = 3000$, $L = 10$, $\gamma = 0.16$, $v_0 = 2$, and $v_1 = 0.1$. Blue filled circles on the phase boundary correspond to peaks in the variance of the particle density, while green squares separate states with zero and nonzero mean orientation. Phases are labeled as per discussion in the text. Horizontal and vertical red lines indicate linear instabilities toward clustering and ordering, respectively. (B) Snapshots of the stripy (b), aster (e), moving clumps [d(i)], and lane [d(ii)] patterns. The crosses in A correspond to the snapshots in B. Particles are color coded by direction, with blue (darker gray) horizontal and red (lighter gray) vertical.

a self-trapping mechanism through which they assemble and slow down, creating a positive feedback loop akin to the one in [20]. This process leads to the formation of high-density clumps which slowly coarsen towards a fully phase-separated steady state. The Vicsek-like alignment tendency greatly affects this instability. On one hand, the critical value $\lambda_c(\epsilon)$ decreases almost to zero with decreasing ϵ. Furthermore, the presence of polar order promoted by the alignment changes the nature of the clusters. In Fig. 1(a), we identify at least three distinct patterns, of which snapshots are shown in Fig. 1(b). When ϵ is small, rather than structureless dots, the clusters show an orientational order and move coherently: they form "moving clumps" [pattern d(i) in Fig. 1]. For low ϵ and large λ the moving clumps merge into bands, or lanes [labelled as d(ii)]—within these, however, particles move parallel rather than perpendicular to the band, in contrast with the $\lambda \to 0$ stripy phase. Although we cannot rule out that the lane and moving clump "phases" may merge in the thermodynamic limits, they appear as distinct up to the largest system we simulated, with $N = 48\,000$ [23] [and ρ as in Fig. 1(a)]. Lanes are somewhat reminiscent of the "streaks" of actin filaments observed in [3]—it would be interesting to compare the dynamics of pattern formation in experiments and simulations to probe how similar the two really are. Finally, in the disordered, high ϵ phase, the clusters instead diffuse randomly and are, on average, stationary. Here, a temporal average of the particle orientation patterns shows that the clusters are asters (the aster phase is labeled as e in Fig. 1). However, as discussed in greater detail below, the orientation in the aster is nonstandard: particles point towards its center at the core, but they coherently point outwards in its periphery. We stress that moving clusters, lanes, and asters are not observed either in the standard Vicsek model [7,10] or in the simulations of its standard mean field continuum description [11].

To get a better understanding of the pattern formation process, we now discuss how to coarse grain the microscopic dynamics (1) to obtain a macroscopic description of the model. On symmetry grounds, there are two candidates for the hydrodynamic fields: the conserved particle density ρ and the local alignment, or polarization, vector $\mathbf{P}$. Note that "hydrodynamic" here means slowly varying in space and time—the dynamics of the underlying fluid is not included in our modeling. Following Refs. [20,24], we start with the microscopic Eq. (1) and use Itō calculus to write down a stochastic dynamical equation for the evolution of $f(\mathbf{r}, \theta) = \sum_{j=1}^{N} \delta(\mathbf{r} - r_j)\delta(\theta - \theta_j)$, the microscopic density of particles at position $\mathbf{r}$ with angle θ, which reads

$$\partial_t f(\mathbf{r}, \theta) + \mathbf{e}_\theta \cdot \nabla[vf] = \epsilon \frac{\partial^2 f}{\partial \theta^2} - \frac{\partial}{\partial \theta}\sqrt{2\epsilon f}\eta - \gamma \frac{\partial}{\partial \theta} \int d\theta' d\mathbf{r}' f(\mathbf{r}', \theta') \times f(\mathbf{r}, \theta) F(\theta' - \theta, \mathbf{r} - \mathbf{r}'). \quad (2)$$

The second term on the left-hand side describes familiar advection, but with one important difference: the velocity v appears *inside* the gradient. This is what leads to the instabilities responsible for the new patterns in the simulations. The interaction term in Eq. (2) differs from other models of SP particles where the alignment is explicitly due to "collisions," and the interaction strength depends on v [14,25]. Such cases can be recovered by allowing γ to vary with v. To derive mean-field hydrodynamics equations for the flying XY model, we first drop the noise term, $\sqrt{2\epsilon f}\eta$. Following Bertin, Droz, and Gregoire [25], we Fourier transform Eq. (2) to get equations of motion for $f_k \equiv \int f(\mathbf{r},\theta)e^{ik\theta}d\theta$. Using $2\pi f(\mathbf{r},\theta) = \sum_k f_k e^{-ik\theta}$ and $2\pi F(\theta,\mathbf{r}) = \sum_k F_k e^{-ik\theta}$, we obtain a hierarchy of equations:

$$\partial_t f_k + \frac{\partial}{\partial x}\frac{v f_{k+1} + v f_{k-1}}{2} + \frac{\partial}{\partial y}\frac{v f_{k+1} - v f_{k-1}}{2i} = -k^2\epsilon f_k + i\frac{\gamma k}{2\pi}\sum_m f_m F_{-m} f_{k-m}, \tag{3}$$

where all sums run from $-\infty$ to $+\infty$. In principle, F is slightly nonlocal in space so that the second term of the right-hand side of Eq. (3) should retain a spatial integral. We are, however, interested in the hydrodynamic, large-scale, description of the system, a limit in which R is very small and we assume F to be perfectly local [26]. To obtain mean-field equations for the hydrodynamic variables, we approximate the mesoscopic density of particles $\rho(x,t)$ by the angular average of the microscopic one, i.e., $\rho \equiv f_0$. This can be justified in dense systems [27–29], where interactions are averaged over many neighbors. In a similar fashion, we approximate the x and y component of $\rho\mathbf{P}$ by the real and imaginary part of f_1, respectively. By writing out in full the $k = 0$ case of Eq. (2), we then find that the density field obeys the continuity equation

$$\partial_t \rho = -\nabla\cdot(v\mathbf{W}), \tag{4}$$

where $\mathbf{W} \equiv \rho\mathbf{P}$. To make further progress, we now assume that we are not too deeply in the ordered phase, so that $f(\theta)$ is to first order approximation homogeneous; hence, higher Fourier components (f_k for $k \geq 3$) may be neglected. Following [25], we further assume that f_2 is a fast variable, so that $\dot{f}_2 \simeq 0$ (this requires $\epsilon \neq 0$). After lengthy but straightforward algebra, we obtain the following equation for $\mathbf{W}$,

$$\partial_t \mathbf{W} + \frac{\gamma}{16\epsilon}(\mathbf{W}\cdot\nabla)(v\mathbf{W}) = \left(\frac{1}{2}\gamma\rho - \epsilon\right)\mathbf{W} - \frac{\gamma^2}{8\epsilon}W^2\mathbf{W} - \frac{1}{2}\nabla(v\rho) + \frac{3\gamma}{16\epsilon}\nabla(vW^2) - \frac{\gamma}{32\epsilon}v\nabla W^2 - \frac{3\gamma}{16\epsilon}\mathbf{W}\nabla\cdot(v\mathbf{W}) - \frac{\gamma}{8\epsilon}v\mathbf{W}(\nabla\cdot\mathbf{W}) - \frac{\gamma}{8\epsilon}v(\mathbf{W}\cdot\nabla)\mathbf{W} + \mathcal{O}(\nabla^2). \tag{5}$$

The second term on the left-hand side of Eq. (5) describes self-advection of particles and breaks Galilean invariance [6]. The first two terms on the right-hand side describe the standard spontaneous symmetry breaking leading to polar order and flocking for sufficiently small ϵ in the Vicsek model at $\lambda = 0$. The third, pressurelike term, $-\frac{1}{2}\nabla(v\rho)$, is the most relevant one in our work, as it is responsible for the clustering instability observed in Fig. 1 when $\lambda \neq 0$. Higher order terms in ∇ and $\mathbf{W}$ have minor effects on patterns and will be discussed elsewhere. When v is constant, Eq. (5) reduces to that in Ref. [25], albeit with a different expression for some of the parameters due to differences in the interaction terms defining the microscopic models [25].

Having written down the mean-field equations of motion, Eqs. (4) and (5), we can now assess how their predictions compare with the simulations of the microscopic model. The continuum theory predicts an order-disorder transition at $\epsilon_c = \frac{1}{2}\gamma\rho_0$. For $\epsilon > \epsilon_c$ there is a stable homogeneous disordered state, with $\rho = \rho_0$ and $\mathbf{W} = 0$. For $\epsilon < \epsilon_c$, the equations yield a homogeneous ordered or flocking state with $\rho = \rho_0$ and $\mathbf{W} = W_0\hat{\mathbf{x}}$, where we have chosen the x axis along the direction of broken symmetry and $W_0 = \sqrt{8\epsilon(\epsilon_c - \epsilon)/\gamma^2}$. The mean-field transition at ϵ_c does not depend on λ and coincides with that of the equilibrium XY model. The order-disorder phase boundary predicted by the theory is compared to its numerical counterpart in Fig. 2(a). We then study the linear stability of the homogeneous disordered state at $\epsilon > \epsilon_c$ against spatially inhomogeneous fluctuations. It is straightforward to show that when $\lambda \neq 0$, the homogeneous disordered phase becomes unstable for all wave numbers when $v(\rho_0) + \rho_0 v'(\rho_0) < 0$. This instability, referred to as a clustering instability, arises due to the term $-\frac{1}{2}\nabla(v\rho)$ in the equation for $\mathbf{W}$. The threshold between

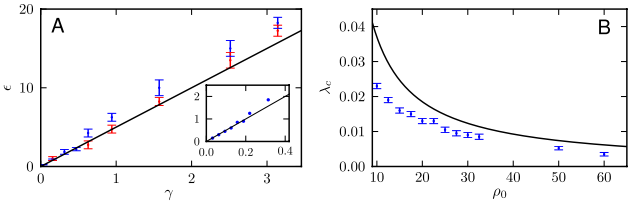

FIG. 2 (color online). (a) Phase boundary for the flying XY model when $\lambda = 0$, showing the critical value of ϵ as a function of γ. Blue (darker gray) points for $v = 2.0$, red (lighter gray) for $v = 0.5$. Inset: data for $v = 2.0$ for smaller values of γ. (b) Phase boundary for $\epsilon = 5$, $\gamma = 0.16$. In all cases $L = 10$ and $N = 1000$.

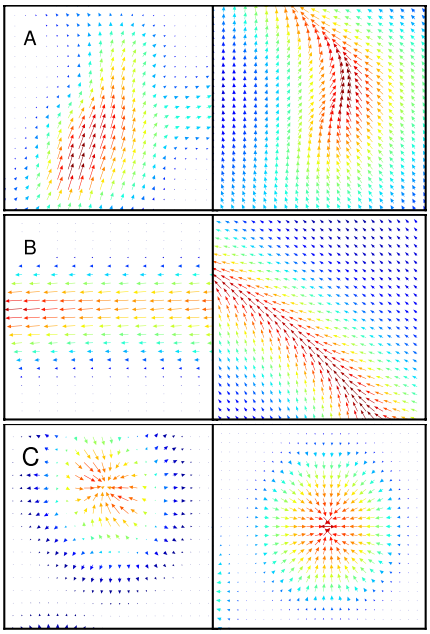

$\tilde{\lambda}$	0.75	1.5
$\tilde{v}_1$	0.05	0.09
$\tilde{\gamma}$	1.6	3.6
$\tilde{D}$	-	0.02

$\tilde{\lambda}$	1.2	1.5
$\tilde{v}_1$	0.05	0.12
$\tilde{\gamma}$	4.8	4.5
$\tilde{D}$	-	0.02

$\tilde{\lambda}$	0.94	1.5
$\tilde{v}_1$	0	0
$\tilde{\gamma}$	0.64	2.3
$\tilde{D}$	-	0.01

FIG. 3 (color online). Patterns found for $\lambda \neq 0$ in the microscopic simulations (left column) and in the numerical solution of the hydrodynamic equations (right). Tables show dimensionless parameter values: $\tilde{\lambda} = \lambda\rho_0$, $\tilde{v}_1 = v_1/v_0$, $\tilde{\gamma} = \gamma\rho_0/\epsilon$, $\tilde{D} = D\epsilon/v_0^2$. Arrows show the $\mathbf{W}$ field, colors the density [red (gray): high; blue (dark gray): low; yellow (light gray): intermediate]. In the right column, only a fraction of the simulated system is shown for clarity.

homogeneous and clustered phases found numerically at large ϵ is close to but below the prediction [(Fig. 2(b)]. This is reasonable, as the linear stability can only access the spinodal line: fluctuations may trigger phase separation for lower λ.

To go beyond the simple linear stability analysis of the homogeneous disordered state, account for the effect of the nonlinear terms, and, hence, explore the range of patterns compatible with our hydrodynamics equations, we solved Eqs. (4) and (5) numerically, by means of a standard finite difference scheme [23]. In order to enhance the stability of our algorithm, we included a diffusive term $D\nabla^2\rho$ on the right-hand side of Eq. (4). Our numerical results show that all the five patterns, or phases, observed in the microscopic simulations (fluctuating flocking state, moving stripes and lanes, static asters, and moving clumps) can be found within Eqs. (4) and (5)—Fig. 3 portrays a comparison of the $\lambda \neq 0$ patterns. Interestingly, the origin of the atypical asters can be directly read from Eq. (5). In the steady-state, low gradient, small $\mathbf{W}$ approximation, Eq. (5) reduces to $(\gamma\rho/2 - \epsilon)\mathbf{W} = \nabla(\rho v/2)$ and $\nabla(v\rho)$ thus acts as an ordering field for $\mathbf{W}$. Along the radius of an aster, the density increases toward the center, whereas the velocity decreases. Their product can thus be nonmonotonic, which makes $\mathbf{W}$ change direction, hence the atypical asters seen in the microscopic simulations. In the continuum simulations, even though $\nabla\rho v$ can change sign, the presence of the diffusive terms disallows sharp gradients, and we did not find parameters for which $\nabla\rho v$ was dominating. We could, however, end up with both inward-pointing or outward-pointing asters, corresponding to phases with high-density clumps (at small λ, shown in Fig. 3(c) or low-density voids (at larger λ, similar to those discussed in [5], not shown).

We have shown that a density-dependent motility in our flying XY model, a close relative of the Vicsek model, yields new patterns in suspensions of SP particles. Such patterns include moving clumps, lanes, and asters. All these patterns have experimental counterparts [3–5]. By explicitly linking the microscopic and coarse-grained mean- field dynamics, we were able to identify the key ingredients that trigger the appearance of the new patterns in the "pressure term"—$\frac{1}{2}\nabla(v\rho)$: when this turns negative, new patterns form. Importantly, the patterns we see are not very sensitive to the precise form of $v(\rho)$. For instance, steric hindrance results in velocities that typically decrease linearly with density [29] and would give similar instabilities.

We close with a comparison with other models featuring patterns similar to ours. Continuum equations for microtubule-kinesin solutions leading to aster formation have been proposed in [30]. These included a phenomenological term $\sim S\nabla(\rho)$ with $S > 0$, and ρ the density of motors bound to microtubules, which is similar to our term $-\frac{1}{2}\nabla(v\rho)$. In the $\lambda = 0$ limit, Refs. [11,25] show that asters are absent if the prefactors in the nonlinear terms in the continuum equations are obtained via systematic coarse-graining (however, they do appear if these prefactors are tuned independently [31]).

Finally, Peruani *et al.* [17] studied a microscopic lattice variant of the Vicsek model and also found asters and moving clumps, dubbed traffic jams and gliders. This is again naturally explained by our theory, as their origin in [17] lies in the slowdown of particles due to crowding jamming, which brings up an effective "pressure term" analogous to that in Eq. (5). A density-dependent motility, induced either by steric hindrance or by crosslinkers between actin fibers, may also at the basis of the formation of similar patterns in the actin-walker experiments in [3].

We thank M. R. Evans for useful discussions. M. C. M. was supported by the National Science Foundation through Grants No. DMR-0806511 and No. DMR-1004789.

[1] S. Ramaswamy and J. F. Joanny, Nature (London) **467**, 33 (2010); S. Ramaswamy, Annu. Rev. Condens. Matter Phys. **1**, 323 (2010).
[2] D. Bray, *Cell Movements: From Molecules to Motility* (Garland, New York, 2001), 2nd ed.
[3] V. Schaller, C. Weber, C. Semmrich, E. Frey, and A. R. Bausch, Nature (London) **467**, 73 (2010); S. Khler, V. Schaller, and A. R. Bausch, Nature Mater. **10**, 462 (2011);

V. Schaller *et al.*, Proc. Natl. Acad. Sci. U.S.A. (to be published).
[4] J. D. Murray, *Mathematical Biology* (Springer-Verlag, Berlin, 2003), Vol. 2.
[5] R. Thar and M. Kuhl, FEMS Microbiol. Lett. **246**, 75 (2005).
[6] J. Toner and Y. H. Tu, Phys. Rev. Lett. **75**, 4326 (1995); Phys. Rev. E **58**, 4828 (1998); J. Toner, Y. Tu, and S. Ramaswamy, Ann. Phys. (N.Y.) **318**, 170 (2005).
[7] T. Vicsek, A. Czirók, E. Ben-Jacob, I. Cohen, and O. Shochet, Phys. Rev. Lett. **75**, 1226 (1995).
[8] A. Baskaran and M. C. Marchetti, Proc. Natl. Acad. Sci. U.S.A. **106**, 15 567 (2009).
[9] R. A. Simha and S. Ramaswamy, Phys. Rev. Lett. **89**, 058101 (2002).
[10] G. Gregoire and H. Chaté, Phys. Rev. Lett. **92**, 025702 (2004); H. Chaté, F. Ginelli, G. Grégoire, and F. Raynaud, Phys. Rev. E **77**, 046113 (2008).
[11] S. Mishra, A. Baskaran, and M. Cristina Marchetti, Phys. Rev. E **81**, 061916 (2010).
[12] G. Gregoire, H. Chaté, and Y. Tu, Physica (Amsterdam) **181D**, 157 (2003).
[13] F. Peruani, A. Deutsch, and M. Bär, Phys. Rev. E **74**, 030904(R) (2006).
[14] A. Baskaran and M. C. Marchetti, Phys. Rev. Lett. **101**, 268101 (2008).
[15] Y. Yang, V. Marceau, and G. Gompper, Phys. Rev. E **82**, 031904 (2010).
[16] S. Henkes, Y. Fily, and M. Cristina Marchetti, Phys. Rev. E **84**, 040301(R) (2011); S. R. McCandlish, A. Baskaran, and M. F. Hagan, Soft Matter **8**, 2527 (2012).
[17] F. Peruani, T. Klauss, A. Deutsch, and A. Voss-Boehme, Phys. Rev. Lett. **106**, 128101 (2011); F. Ginelli, F. Peruani, M. Bär, and H. Chaté, Phys. Rev. Lett. **104**, 184502 (2010).
[18] One should further distinguish between collection of sterically interacting SP particles where alignment is imposed á la Vicsek and others where it comes solely from steric repulsion of rodlike particles [13–15,17]. In the latter case, steric repulsion yields nematic rather than polar order.
[19] Other functional dependencies lead to a less rich physics—details will be given elsewhere.
[20] J. Tailleur and M. E. Cates, Phys. Rev. Lett. **100**, 218103 (2008); M. E. Cates, D. Marenduzzo, I. Pagonabarraga, and J. Tailleur, Proc. Natl. Acad. Sci. U.S.A. **107**, 11 715 (2010).
[21] C. Liu *et al.*, Science **334**, 238 (2011).
[22] Larger values of N, routinely needed to reliably characterize the nature of the phase transition in Vicsek models [10], lead to negligible corrections for our phase boundary [23].
[23] See Supplemental Material at http://link.aps.org/supplemental/10.1103/PhysRevLett.108.248101 for additional details on finite size effects and on our finite difference simulations of the hydrodynamic equations of motion.
[24] D. S. Dean, J. Phys. A **29**, L613 (1996).
[25] E. Bertin, M. Droz, and G. Gregoire, J. Phys. A **42**, 445001 (2009).
[26] A nonlocal F can be dealt, e.g., as in [20].
[27] H. Zinn-Justin, *Quantum Field Theory and Critical Phenomena* (Clarendon, Oxford, 1989).
[28] J. Tailleur, J. Kurchan, and V. Lecomte, J. Phys. A **41**, 505001 (2008).
[29] A. G. Thompson, J. Tailleur, M. E. Cates, and R. A. Blythe, J. Stat. Mech. (2011) P02029.
[30] H. Y. Lee and M. Kardar, Phys. Rev. E **64**, 056113 (2001); S. Sankararaman and G. I. Menon, Phys. Rev. E **70**, 031905 (2004).
[31] A. Gopinath *et al.*, arXiv:1112.6011 [Phys. Rev. E (to be published)]; K. Gowrishankar and M. Rao, arXiv:1201.3938.

Mechanically Driven Growth of Quasi-Two-Dimensional Microbial Colonies

F. D. C. Farrell,[1,*] O. Hallatschek,[2,3] D. Marenduzzo,[1] and B. Waclaw[1]

[1]SUPA, School of Physics and Astronomy, University of Edinburgh, Mayfield Road, Edinburgh EH9 3JZ, United Kingdom
[2]MPI for Dynamics and Self-Organization, Bunsenstrasse 10, D-37073 Göttingen, Germany
[3]Department of Physics, University of California, Berkeley, California 94720, USA

(Received 25 March 2013; published 14 October 2013)

We study colonies of nonmotile, rod-shaped bacteria growing on solid substrates. In our model, bacteria interact purely mechanically, by pushing each other away as they grow, and consume a diffusing nutrient. We show that mechanical interactions control the velocity and shape of the advancing front, which leads to features that cannot be captured by established Fisher-Kolmogorov models. In particular, we find that the velocity depends on the elastic modulus of bacteria or their stickiness to the surface. Interestingly, we predict that the radius of an incompressible, strictly two-dimensional colony cannot grow linearly in time, unless it develops branches. Importantly, mechanical interactions can also account for the nonequilibrium transition between circular and branching colonies, often observed in the lab.

DOI: 10.1103/PhysRevLett.111.168101 PACS numbers: 87.18.Hf, 87.10.−e, 87.18.Fx

Active matter, which constantly takes energy from its environment in order to do work [1], has recently attracted much interest. Particular examples are collections of cells such as tissues and suspensions of swimming bacteria [2–4], and microbial colonies, in which activity is caused by growth, death, and migration of cells. The combination of these three factors has been shown to lead to a variety of interesting and universal patterns [5–8]. For example, bacteria such as *B. subtilis* or *E. coli* grown on Petri dishes form patterns ranging from circular, through Eden-like [9], to diffusion-limited aggregationlike patterns [10]. Such patterns have been traditionally modelled using a system of diffusive Fisher-Kolmogorov equations [11,12] which combine migration (diffusion of bacteria), bacterial growth, and nutrient diffusion. This approach, however, does not accurately represent the growth on surfaces on the microscopic level, where expansion is caused by cells pushing each other out of the way as they grow, rather than by migration.

In this Letter, we study the role of mechanical interactions in the growth of dense colonies on solid substrates. Inspired by recent experiments in microfluidic devices [13], we study quasi-two-dimensional growth of a colony of nonmotile single-celled organisms which consume nutrient in order to grow and divide. We argue—supported by computer simulations and analytical calculations—that mechanical interactions between bacterial cells can account for the emergence of a nonequilibrium transition between quasi-circular and branched colonies as a function of the ratio between the nutrient consumption rate and the growth rate. The strength of mechanical interactions determines the speed with which the colony expands in space, with diffusion of the nutrient playing a secondary role. We also show that the leading edge of the front is very sharp, and the bacterial density is discontinuous at the front, in contrast to a smooth, exponential profile predicted by models based on coupled Fisher equations [8,12]. Our results are relevant to the growth of biofilms [14–16], which are ubiquitous in nature and are involved in a variety of medical and technological problems. As

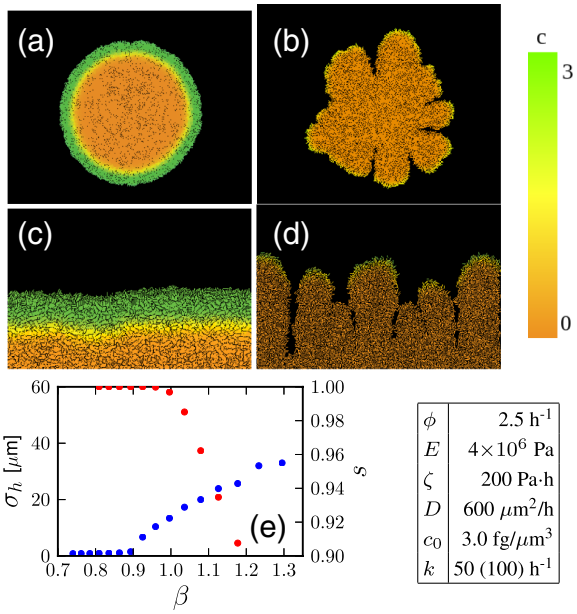

FIG. 1 (color online). (a),(b) Snapshots from the simulation of $N \sim 10^5$ cells, for low (a) and high (b) values of the branching parameter β (see also, videos in Supplemental Material [19]). Colors correspond to the local nutrient concentration, see the color map on the right. Only a thin layer of cells grows appreciably. (c),(d) Growth in a narrow, long strip, for low (c) and high (d) β. The frame is comoving with the front. (e) Roughness of the front σ_h (blue or dark points) and fraction of space filled by cells, s (red or light points), as a function of β (flat geometry, box width $L = 250$ μm). Table shows parameter values used; k was increased to 100 in (b) and (d). These are the default parameter values used in the rest of the Letter unless otherwise stated.

mechanical interactions may alter the colony morphology, and the fixation probability of (potentially harmful) mutants [17,18], understanding their role is of paramount importance.

We simulate bacteria using two-dimensional Newtonian dynamics. Cells are modelled as growing spherocylinders of constant diameter $d = 1\ \mu$m and variable length that split in half to yield two cells when they reach some critical length ℓ_c (usually 4 μm). The colony grows on a two-dimensional flat surface with nutrient concentration $c(x, y)$. The nutrient diffuses with diffusion constant D. Initially, $c = c_0$ everywhere, and c is always held constant at the edges of the simulation box, which is made large enough that the boundary does not affect the growth. Nutrients are consumed at a rate $kf(c)$ per unit biomass density, where $f(c)$ is a monotonically increasing dimensionless function. In most simulations, we use a Monod function $c/(c_{\text{half}} + c)$ with half-saturation constant c_{half}. Cells grow (by elongation) at a rate $v_g f(c)$. All parameters and their values are detailed in the Supplemental Material [19].

The cells interact mechanically. The force between overlapping bacteria is assumed to be given by the Hertzian theory of elastic contact [13,20,21]: $F = Ed^{1/2}h^{3/2}$ where h is the overlap and E parametrizes the strength of the interaction and is proportional (modulo a dimensionless prefactor) to the elastic modulus of the cells, and the dynamics is overdamped so that velocity is proportional to force, $v = F/\zeta$, where ζ is the friction coefficient.

We start our simulations from either a single initial cell or a line of cells, and follow the shape of the colony after many rounds of cell replication, leading to a circular colony or a horizontal advancing front, respectively. Figure 1 shows that the morphology of a large colony of bacteria can be either smooth or branched, depending on the parameters of the model.

By performing simulations for different parameter sets we have found that the fate (smooth or branched) of the colony is determined by a dimensionless "branching parameter" $\beta = (k\rho_0)/(\phi c_0)$, where ρ_0 is the close-packed cell density, and the other parameters have been defined previously.

For small values of β, the front of the colony remains smooth throughout the simulation [Figs. 1(a) and 1(c)], whereas for large values branches develop [Figs. 1(b) and 1(d)]. Note that, as in real colonies [17], the nutrient becomes depleted within the colony so that only cells in a thin layer at the front are growing. To pinpoint the location of the transition, we compute the roughness of the front [Fig. 1(e)], defined as the mean square deviation of points on the front from its average position, as in Ref. [6]. At $\beta \simeq 0.9$, there is a transition from a flat to a rough front, whereas at $\beta \simeq 1$, there is a switch between a quasicircular front and one with branches, demonstrated by the filling fraction s falling below 1. This behavior is similar to that observed in Ref. [6].

This transition between branched and smooth colony fronts is well known in real colonies [22] and has been the subject of many theoretical studies [8,12], which usually attribute it to the interplay between diffusion (migration) of bacteria and diffusion of the nutrient. In our model, however, the transition is driven by the uptake of nutrient by the cells and their growth by mechanical pushing, and is unaffected by the diffusion rate of the nutrient.

To gain a better understanding of this transition, we approximate the growing colony as an incompressible cellular "fluid" [23]. Mass conservation in such a fluid is described by the equation $\nabla \cdot \mathbf{v} = \phi f(c(\mathbf{x}))$, where $\mathbf{v}$ is the fluid velocity, $f(c)$ is the dimensionless nutrient uptake function, and ϕ is the growth rate of the cellular fluid, given by $\phi = v_g/\ell_c$. Let us begin with a one dimensional case of a colony advancing from the left and consuming nutrient, and characterized by a single number $x_0(t)$ which is the position of the front

$$\partial_t c(x, t) = D\partial_x^2 c(x, t) - k\rho_0 f(c(x, t))\Theta(x_0 - x), \quad (1)$$

$$v(x_0) = \frac{dx_0}{dt} = \phi \int_{-\infty}^{x_0(t)} f(c(x, t))dx. \quad (2)$$

Here D is the nutrient diffusion constant, k the rate of uptake of nutrient by cells, ρ_0 the cell density (constant everywhere due to incompressibility), and Θ is the Heaviside step function. Because cells do not migrate and they are tightly packed, the density is either ρ_0 or zero, and hence, Eq. (2) can be derived from the continuity equation and the incompressibility condition, assuming that $\rho(x, t) = \rho_0\Theta(x_0(t) - x)$. We also impose boundary conditions that $c(-\infty) = 0$ and $c(\infty) = c_0$.

We first determine whether Eqs. (1) and (2) admit a travelling-wave solution $c(x, t) = \hat{c}(x - vt) \equiv \hat{c}(z)$ in the limit $t \to \infty$, where the velocity v of the front is constant. The resulting equations for $\hat{c}(z)$ and v are

$$-v\hat{c}'(z) = D\hat{c}''(z) - k\rho_0 f(\hat{c})\Theta(-z), \quad (3)$$

$$v = \phi \int_{-\infty}^{0} f(\hat{c}(z))dz. \quad (4)$$

For $z > 0$, the solution to Eq. (3) is given by $\hat{c}(z) = c_0 + Ae^{-vz/D}$ [as $c(\infty) = c_0$]. For $z < 0$, we can rearrange the equation to yield $f(\hat{c}(z)) = (1/k\rho_0)[D\hat{c}''(z) + v\hat{c}'(z)]$, which, upon insertion into Eq. (4), gives

$$v = \frac{\phi}{k\rho_0}[D\hat{c}'(0) + v\hat{c}(0)] = \frac{\phi c_0}{k\rho_0}v, \quad (5)$$

where we have integrated by parts, and used the fact that $\hat{c}$ vanishes at $-\infty$, and that $\hat{c}$ and $\hat{c}'$ must be continuous at $z = 0$. Therefore, a solution for v exists only if $\phi c_0 = k\rho_0$ (or $\beta = 1$) exactly: we have found that in the incompressible limit the front cannot advance at a constant speed. This is in contrast to the Fisher framework, where travelling waves exist for a range of parameters. Numerical solutions

of Eqs. (1) and (2) fully confirm our prediction, showing exponential growth for $\beta < 1$ and sublinear growth for $\beta > 1$, see Supplemental Material [19]. This is only true if the growth and the uptake rate on c have the same functional form, $f(c)$. This is a good approximation for *E. coli* and other bacteria with low maintenance costs [24], but is not true in general [25]. Choosing different dependencies on c for these rates, however, leads to qualitatively similar conclusions, with constant growth possible in a narrow window of β close to 1.

The hint from this simplified 1D model is that $\beta = 1$ is a critical value that separates different regimes of colony growth. For $\beta > 1$, growth is limited by nutrient diffusion, whereas for $\beta < 1$ diffusion does not play any role. However, the front has more freedom in 2D than in 1D—it can become branched. Since this transition occurs close to $\beta = 1$, it is appealing to conjecture that the branching transition in Fig. 1 is linked to the switch in growth laws for incompressible colonies described above.

Second, incompressible theory predicts that growth cannot be linear, unless $\beta = 1$ exactly. This is inconsistent with experimental results: the size of a colony of nonswimming bacteria growing on stiff agar gels does increase linearly with time [26]. Moreover, our simulations also lead to a finite steady state speed. The speed found in simulations depends on the elasticity E, as can be seen in Fig. 2(a), suggesting the compressibility of the cells is important.

Generalizing the theory above to compressible cells in 1D, we now need equations for mass and momentum conservation, as well as the nutrient diffusion equation

$$\partial_t c = D\partial_x^2 c - k\rho f(c), \tag{6}$$

$$\partial_t \rho + \partial_x(\rho v) = \phi\rho f(c), \tag{7}$$

$$\partial_x p = -\mu\rho v. \tag{8}$$

The term $\mu\rho v$ describes the friction between the surface and the cells. The pressure $p(\rho)$ is determined by the force acting between the cells. We take $p[\rho(x)] = E[1 - \rho_0/\rho(x)]^{3/2}$ to be consistent with our simulations, because the force that acts between two overlapping cells is then proportional to $Ed^{1/2}h^{3/2}$, where $h = d[1 - \rho_0/\rho(x)]$ is the overlap. ρ_0 is the uncompressed density of closely packed cells.

Although Eqs. (6)–(8) cannot be solved analytically, numerical solution (see Supplemental Material [19]) shows that a travelling wave now exists for $\beta < 1$. The density profile close to the edge decays according to a power law towards the uncompressed cell density ρ_0. This is in striking contrast to Fisher-Kolmogorov waves, which exhibit exponential density profiles in the wave tip [12]. Many other properties of the solution to Eqs. (6)–(8) can be deduced without solving the equations. First, a "biomass conservation law" from Eqs. (6) and (7) states that one unit of nutrient biomass makes ϕ/k units of bacterial biomass,

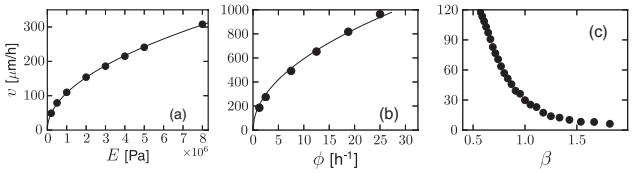

FIG. 2. Steady state speed of colony growth, v, as a function of various parameters, for 2D simulations in the quasi-1D geometry. (a) and (b) have fits to a square root function. In (b), ϕ is varied while holding β constant (by inversely varying k). (c) shows the dependence on β (c_0 is varied while keeping other parameters constant), with a change in behavior around $\beta = 1$.

and hence the density $\rho(-\infty)$ deep in the colony must be $\phi c_0/k$. This explains why a travelling wave solution cannot exist in the incompressible case: unless the cell density ρ_0 equals exactly $\phi c_0/k$ it will not match the density of biomass produced by the nutrient. It also explains why there is a morphological transition to branched colonies at $\beta \simeq 1$: growth of a compact colony is not possible for $\beta > 1$ as it would need to have a density less than ρ_0. Finally, it suggests that if bacteria are restricted to grow as a monolayer, then, when nutrient is abundant, they will grow exponentially until intermicrobial forces within the colony are so large that the bacteria in the middle are squashed to the appropriate density ρ_0/β.

We can estimate the velocity of the travelling wave using a simple scaling argument. At steady state, the cells are compressed to the strain $\epsilon \equiv 1 - \beta$, and the pressure profile has to rise from 0 at the edge of the population to a maximal value p_* in the bulk within a boundary layer of characteristic size λ. The characteristic length λ can be eliminated by estimating it to be the length by which the front moves in one generation $\lambda \approx v/[\phi f(c_0)]$. The bulk value of the pressure $p_*(\epsilon)$ is just large enough that the density of the population is compressed down to the strain ϵ. The elastic constitutive relation $p_*(\epsilon)$ of the microbial population fixes the corresponding pressure, with $p_*(\epsilon) = E\epsilon^{3/2}$ in our case of Hertzian contacts between cells. The pressure p_* pushes the front population at the speed v against the friction force $v\mu\rho_0\lambda$, where $\mu\rho_0$ acts as a friction coefficient per unit length. Thus, force balance yields

$$v \approx \sqrt{\frac{\phi f(c_0) p_*(\epsilon)}{\mu\rho_0}} = \sqrt{\frac{E\phi f(c_0)}{\mu\rho_0}}\, g(\beta), \tag{9}$$

where $g(\beta) = (1 - \beta)^{3/4}$.

To test the above formula, we performed a fully one-dimensional version of our simulations described above, as this removed the effects of branching and was much more computationally efficient. The results are shown in Fig. 3. Figure 3(a) shows that the front speed grows as $\sqrt{E}$ as predicted by Eq. (9), and Fig. 3(b) shows that the dependence of v on β is in good agreement with the numerically and theoretically predicted $g(\beta)$, although the theoretical

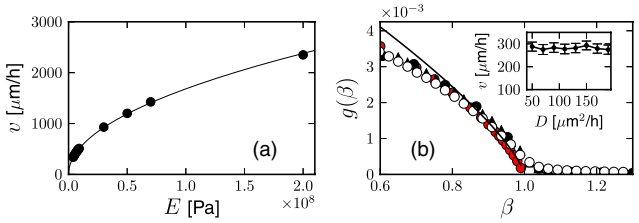

FIG. 3 (color online). Dependence of front speed on parameters in the fully 1D simulation. (a) Front speed as a function of elastic modulus E, with fit to $v = A\sqrt{E}$. (b) Transition from moving to stopped front as a function of β, which occurs when $\beta = 1$. $g(\beta)$ [defined by Eq. (9)] is plotted against β (by varying k) for $\phi = 10$ (open circles), 20 (triangles), and 30 (closed circles), showing a good collapse. Here $E = 4 \times 10^6$, $D = 100$. Solid line corresponds to theoretical $g(\beta) = (1 - \beta)^{3/4}$, and red (grey) circles are the numerical solution of Eqs. (6)–(8). Inset: v as a function of D, showing no dependence.

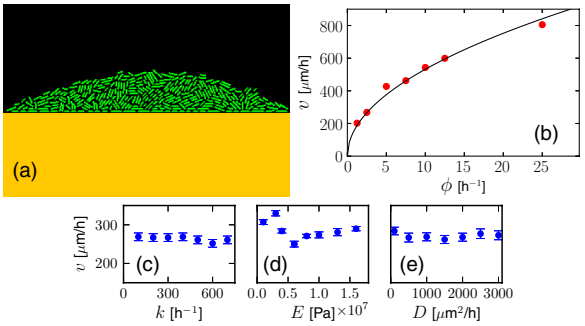

FIG. 4 (color online). Quasi-3D colony growth. (a) Snapshot. (b) Speed of radial colony growth against ϕ, with fit to $A\sqrt{\phi}$. (c)–(e) Speed against k, E and D, showing little dependence on any of these parameters. Parameters not being varied take their default values (Fig. 1).

form $g(\beta) = (1 - \beta)^{3/4}$ is only accurate for β close to 1. Figure 2 shows that the square-root dependence on E and ϕ also holds in the 2D case, but the function $g(\beta)$ is again different, and does not go to zero for $\beta > 1$, due to the branching. In the Supplemental Material [19], we perform a more rigorous derivation of Eq. (9), showing that it is valid when the dimensionless parameter $G = E/(\mu D \rho_0) \gg 1$ and β is close to 1. We also show that mechanics-dominated growth $G \gg 1$ is relevant for any experimentally feasible parameters. An interesting feature of this limit is that, since the dynamics are dominated by mechanics rather than nutrient diffusion, v does not depend on D.

So far, our findings are relevant to bacteria growing in monolayers. On agar plates, however, cells are observed to build up vertically in the colony center [27,28]. To probe how this affects our results, we simulate a colony growing in a vertical 2D plane xz (where the z axis is perpendicular to the substrate) instead of the xy plane from previous simulation. We also incorporate attractive cell-substrate interactions, and we model the diffusion in the $z < 0$ half-plane only, which models the substrate. This situation is far more computationally efficient than fully 3D simulations (see Supplementary Material [19]), and still allows us to study the effect of vertical growth. As is apparent from Fig. 4(a), cells do now escape out of the plane they start from, due to the force exerted by neighbors. The size of the colony once again grows linearly in time. However, it is not compressibility, but the possibility of escape into the vertical direction, which leads to linear growth.

In fact, if the bulk pressure $p_*(\epsilon)$, which builds up in a strictly two-dimensional setting, is larger than some critical pressure p_c, cells will escape into the z dimension. As a consequence the pressure profile will saturate at p_c in the bulk of the population. In our scaling argument for the speed of the front growth, we then have $v \approx \{[\phi f(c_0) p_c]/(\mu \rho_0)\}^{1/2}$. Figures 4(b)–4(e) show that, in contrast to the 2D case, the expansion speed $v \sim \sqrt{\phi}$ is now independent of the consumption rate k, elastic modulus E, and the diffusion constant D. Note that while the radial growth is independent of k, the vertical growth will be affected by it.

In conclusion, we have studied the growth of bacterial colonies where nonmotile microorganisms replicate and push each other away as they grow. We find a transition between two different growth regimes, controlled by the balance between growth and uptake of nutrients. Our model differs from biofilm simulations [29,30] which do not explicitly model mechanical forces. We also find that the functional form of the density profile close to the bacterial edge qualitatively differs from those predicted by Fisher-Kolmogorov models, and predict that the speed at which the front propagates depends only weakly on the nutrient diffusion rate D, for a wide range of D. Our predictions should be experimentally testable, especially in 3D, or directly in 2D using a microfluidic device restricting cell growth to a single layer. This could be used to estimate the elastic modulus of the cells through Eq. (9).

Additionally, our results may be relevant in other situations involving the growth of cells under limiting conditions, such as animal and cancerous tissues, which similarly involve a collection of cells proliferating and pushing on each other as they grow, often with their growth limited by the diffusion of nutrients. Mechanical interactions are understood to be very important in such systems; in particular, mechanical pressure has been hypothesized to strongly affect the growth and apoptosis rates of cells, leading to an alternative form of growth limitation [31–33]. Simulations and experiments indicate that this can lead to a steady state speed of growth [31]. It would be interesting to model this effect in our framework, and to study its interplay with nutrient limitation of growth.

We thank R. J. Allen and M. R. Evans for helpful comments on this manuscript. O. H. thanks the Deutsche Forschungsgemeinschaft (DFG) for financial support (Grant No. A15, SFB 937). B. W. acknowledges the support of a Leverhulme Trust Early Career Fellowship.

*Corresponding author.
ffarrell123@gmail.com

[1] S. Ramaswamy, Annu. Rev. Condens. Matter Phys. **1**, 323 (2010).
[2] M. Basan, J.-F. Joanny, J. Prost, and T. Risler, Phys. Rev. Lett. **106**, 158101 (2011).
[3] R. A. Simha and S. Ramaswamy, Phys. Rev. Lett. **89**, 058101 (2002).
[4] A. Sokolov, I. S. Aranson, J. O. Kessler, and R. E. Goldstein, Phys. Rev. Lett. **98**, 158102 (2007).
[5] E. Ben-Jacob, O. Schochet, A. Tenenbaum, I. Cohen, A. Czirók, and T. Vicsek, Nature (London) **368**, 46 (1994).
[6] J. Bonachela, C. Nadell, J. Xavier, and S. Levin, J. Stat. Phys. **144**, 303 (2011).
[7] M. E. Cates, D. Marenduzzo, I. Pagonabarraga, and J. Tailleur, Proc. Natl. Acad. Sci. U.S.A. **107**, 11715 (2010).
[8] K. Kawasaki, A. Mochizuki, M. Matsushita, T. Umeda, and N. Shigesada, J. Theor. Biol. **188**, 177 (1997).
[9] M. Eden, in *Proceedings of the Fourth Berkeley Symposium on Mathematical Statistics and Probability* (University of California Press, Berkeley, 1961), pp. 223–239.
[10] H. Fujikawa and M. Matsushita, J. Phys. Soc. Jpn. **58**, 3875 (1989).
[11] E. Ben-Jacob, I. Cohen, and H. Levine, Adv. Phys. **49**, 395 (2000).
[12] J. Murray, *Mathematical Biology* (Springer-Verlag, Berlin, 2003), Vol. 2, Chaps. 5–6.
[13] F. Volfson, S. Cookson, J. Hasty, and L. Tsimring, Proc. Natl. Acad. Sci. U.S.A. **105**, 15346 (2008).
[14] J. W. Costerton, P. S. Stewart, and E. P. Greenberg, Science **284**, 1318 (1999).
[15] B. A. Hense, C. Kuttler, J. Müller, M. Rothballer, A. Hartmann, and J.-U. Kreft, Nat. Rev. Microbiol. **5**, 230 (2007).
[16] J. B. Xavier, E. Martinez-Garcia, and K. R. Foster, Am. Nat. **174**, 1 (2009).
[17] O. Hallatschek and D. Nelson, Evolution (Lawrence, Kans.) **64**, 193 (2010).
[18] J. Kuhr, M. Leisner, and E. Frey, New J. Phys. **13**, 113013 (2011).
[19] See Supplemental Material at http://link.aps.org/supplemental/10.1103/PhysRevLett.111.168101 for further details of simulations and calculations, and for supplementary videos.
[20] D. Boyer, W. Mather, O. Mondragón-Palomino, S. Orozco-Fuentes, T. Danino, J. Hasty, and L. S. Tsimring, Phys. Biol. **8**, 026008 (2011).
[21] L. D. Landau and E. M. Lifschitz, *Theory of Elasticity* (Elsevier, Oxford, 2008), 3rd ed.
[22] J. A. Shapiro, BioEssays **17**, 597 (1995).
[23] A similar analysis has been performed in the context of biofilm growth in: I. Klapper and J. Dockery, SIAM J. Appl. Math. **62**, 853 (2002); D. A. Head, Phys. Rev. E **88**, 032702 (2013).
[24] J. Monod, Annu. Rev. Microbiol. **3**, 371 (1949).
[25] S. J. Pirt, Proc. R. Soc. B **163**, 224 (1965).
[26] O. Hallatschek, P. Hersen, S. Ramanathan, and D. Nelson, Proc. Natl. Acad. Sci. U.S.A. **104**, 19926 (2007).
[27] L. Z. Pipe and M. J. Grimson, Mol. Biosyst. **4**, 192 (2008).
[28] A. Seminara, T. E. Angelini, J. N. Wilking, S. Vlamakis, H. adn Ebrahim, R. Kolter, D. A. Weitz, and M. P. Brenner, Proc. Natl. Acad. Sci. U.S.A. **109**, 1116 (2012).
[29] J. U. Kreft, G. Booth, and J. W. T. Wimpenny, Microbiology **144**, 3275 (1998).
[30] L. A. Lardon, B. V. Merkey, S. Martins, A. Dötsch, C. Picioreanu, J.-U. Kreft, and B. F. Smets, Environ. Microbiol. **13**, 2416 (2011).
[31] D. Drasdo, S. Hoehme, and M. Bock, J. Stat. Phys. **128**, 287 (2007).
[32] M. Basan, J. Prost, J. Elgeti, and J. F. Joanny, Phys. Biol. **8**, 026014 (2011).
[33] B. Shraiman, Proc. Natl. Acad. Sci. U.S.A. **102**, 3318 (2005).

Bibliography

[1] S. Ramaswamy. The Mechanics and Statistics of Active Matter. *Annu. Rev. Cond. Matt. Phys., Vol 1*, **1**, 2010.

[2] M. C. Marchetti, J. F. Joanny, S. Ramaswamy, T. B. Liverpool, J. Prost, M. Rao, and R. A. Simha. Hydrodynamics of soft active matter. *Rev. Mod. Phys.*, **85**:1143–1182, 2013.

[3] A. Schechter. Birds of a feather. *New Scientist*, Jan 1999.

[4] D. J. T. Sumpter. The principles of collective animal behaviour. *Philos. Trans. R. Soc. Lond. B. Biol. Sci.*, **361**(1465):5–22, 2006.

[5] T. Vicsek, A. Czirók, E. Ben-Jacob, I. Cohen, and O. Shochet. Novel Type of Phase Transition in a System of Self-Driven Particles. *Phys. Rev. Lett.*, **75**(6):1226–1229, 1995.

[6] C. W. Reynolds. Flocks, herds and schools: A distributed behavioral model. *ACM SIGGRAPH Comput. Graph.*, **21**(4):25–34, 1987.

[7] J. Toner and Y. Tu. Flocks, herds, and schools: A quantitative theory of flocking. *Phys. Rev. E*, **58**(4):4828–4858, 1998.

[8] P. M. Chaikin and T. C. Lubensky. *Principles of Condensed Matter Physics*. Cambridge University Press, Cambridge, 1995.

[9] G. Grégoire, H. Chaté, and Y. Tu. Moving and staying together without a leader. *Phys. D Nonlinear Phenom.*, **181**(3-4):157–170, 2003.

[10] G. Grégoire and H. Chaté. Onset of Collective and Cohesive Motion. *Phys. Rev. Lett.*, **92**(2):025702, 2004.

[11] J. Toner, Y. Tu, and S. Ramaswamy. Hydrodynamics and phases of flocks. *Ann. Phys. (N. Y).*, **318**(1):170–244, 2005.

[12] H. Chaté, F. Ginelli, and F. Raynaud. Collective motion of self-propelled particles interacting without cohesion. *Phys. Rev. E*, **77**(4):046113, 2008.

[13] S. Mishra, A. Baskaran, and M. C. Marchetti. Fluctuations and Pattern Formation in Self-Propelled Particles. *Phys. Rev. E - Stat. Nonlinear Soft Matter Phys.*, **81**(6 Pt 1):061916, 2010.

[14] M. R. D'Orsogna, Y. L. Chuang, A. L. Bertozzi, and L. S. Chayes. Self propelled particles with soft-core interactions: Patterns, stability and collapse. *Phys. Rev. Lett.*, **96**:104302, 2006.

[15] G. Baglietto and E. V. Albano. Nature of the order-disorder transition in the Vicsek model for the collective motion of self-propelled particles. *Phys. Rev. E - Stat. Nonlinear Soft Matter Phys.*, **80**(5 Pt 1):050103, 2009.

[16] E. Bertin, M. Droz, and G. Grégoire. Hydrodynamic equations for self-propelled particles: microscopic derivation and stability analysis. *J. Phys. A Math. Theor.*, **42**(44):33, 2009.

[17] I. Couzin, J. Krause, N. Franks, and S. Levin. Effective leadership and decision-making in animal groups on the move. *Nature*, **433**(February):2–5, 2005.

[18] I. D. Couzin, J. Krause, R. James, G. D. Ruxton, and N. R. Franks. Collective memory and spatial sorting in animal groups. *J. Theor. Biol.*, **218**(1):1–11, 2002.

[19] H. Hildenbrandt, C. Carere, and C. Hemelrijk. Self-organized aerial displays of thousands of starlings: a model.

[20] C. K. Hemelrijk and H. Hildenbrandt. Some causes of the variable shape of flocks of birds. *PLoS One*, **6**(8):e22479, 2011.

[21] M. Ballerini, N. Cabibbo, R. Candelier, A. Cavagna, E. Cisbani, I. Giardina, A. Orlandi, G. Parisi, A. Procaccini, M. Viale, and V. Zdravkovic. An empirical study of large, naturally occurring starling flocks: a benchmark in collective animal behaviour. 2008.

[22] M. Ballerini, N. Cabibbo, R. Candelier, A. Cavagna, E. Cisbani, I. Giardina, V. Lecomte, A. Orlandi, G. Parisi, A. Procaccini, M. Viale, and V. Zdravkovic. Interaction ruling animal collective behavior depends on topological rather than metric distance: evidence from a field study. *Proc. Natl. Acad. Sci. U. S. A.*, **105**(4):1232–7, 2008.

[23] G. F. Young, L. Scardovi, A. Cavagna, I. Giardina, and N. E. Leonard. Starling flock networks manage uncertainty in consensus at low cost. *PLoS Comput. Biol.*, **9**(1):e1002894, 2013.

[24] F. G. Woodhouse and R. E. Goldstein. Spontaneous Circulation of Confined Active Suspensions. *Phys. Rev. Lett.*, **109**(16):168105, 2012.

[25] S. r. Vedel, S. Tay, D. M. Johnston, H. Bruus, and S. R. Quake. Migration of cells in a social context. *Proc. Natl. Acad. Sci. U. S. A.*, **110**:129–34, 2013.

[26] H. H. Wensink, J. Dunkel, S. Heidenreich, K. Drescher, R. E. Goldstein, H. Löwen, and J. M. Yeomans. Meso-scale turbulence in living fluids. *Proc. Natl. Acad. Sci. U. S. A.*, **109**(36):14308–13, 2012.

[27] F. Ginelli, F. Peruani, M. Bär, and H. Chaté. Large-Scale Collective Properties of Self-Propelled Rods. *Phys. Rev. Lett.*, **104**(18):184502, 2010.

[28] A. Baskaran and M. C. Marchetti. Hydrodynamics of self-propelled hard rods. *Phys. Rev. E*, **77**(1):011920, 2008.

[29] F. Peruani, A. Deutsch, and M. Bär. Nonequilibrium clustering of self-propelled rods. *Phys. Rev. E. Stat. Nonlin. Soft Matter Phys.*, **74**:030904, 2006.

[30] A. Baskaran and M. C. Marchetti. Statistical mechanics and hydrodynamics of bacterial suspensions. *Proc. Natl. Acad. Sci. U. S. A.*, **106**(37):15567–15572, 2009.

[31] R. A. Simha and S. Ramaswamy. Hydrodynamic Fluctuations and Instabilities in Ordered Suspensions of Self-Propelled Particles. *Phys. Rev. Lett.*, **89**(5), 2002.

[32] D. A. Fletcher and R. D. Mullins. Cell mechanics and the cytoskeleton. *Nature*, **463**:485–492, 2010.

[33] Jonathon Howard. *Mechanics of Motor Proteins and the Cytoskeleton*. Sinauer Associates Inc., 2005.

[34] F. Nédélec, T. Surrey, A. Maggs, and S. Leibler. Self-organization of microtubules and motors. *Nature*, **389**:6648, 1997.

[35] T. Surrey, L. S. Nédélec, F., and E. Karsenti. Physical properties determining self-organization of motors and microtubules. *Science*, **292**:1167, 2001.

[36] F. Jülicher, K. Kruse, J. Prost, and J. F. Joanny. Active behavior of the cytoskeleton. *Phys. Rep.*, **449**:3–28, 2007.

[37] K. Kruse, J. F. Joanny, F. Julicher, J. Prost, and K. Sekimoto. Asters, vortices, and rotating spirals in active gels of polar filaments. *Phys. Rev. Lett.*, **92**(7), 2004.

[38] A. C. Callan-Jones, J.-F. Joanny, and J. Prost. Viscous-fingering-like instability of cell fragments. *Phys. Rev. Lett.*, **100**:258106, 2008.

[39] N. Yoshinaga, J.-F. Joanny, J. Prost, and P. Marcq. Polarity patterns of stress fibers. *Phys. Rev. Lett.*, **105**:238103, 2010.

[40] O. du Roure, A. Saez, A. Buguin, R. H. Austin, P. Chavrier, and P. Siberzan. Force mapping in epithelial cell migration. *Proc. Natl. Acad. Sci. USA*, **102**:23902395, 2004.

[41] A. Mertz, S. Banerjee, Y. Che, G. German, Y. Xu, C. Hyland, M. Marchetti, V. Horsley, and E. Dufresne. Scaling of Traction Forces with the Size of Cohesive Cell Colonies. *Phys. Rev. Lett.*, **108**, 2012.

[42] J. Ranft, M. Basan, J. Elgeti, J.-F. Joanny, J. Prost, and F. Jülicher. Fluidization of tissues by cell division and apoptosis. *Proc. Natl. Acad. Sci. U. S. A.*, **107**(49):20863–8, 2010.

[43] M. Basan, J.-F. Joanny, J. Prost, and T. Risler. Undulation Instability of Epithelial Tissues. *Phys. Rev. Lett.*, **106**(15), 2011.

[44] E. Hannezo, J. Prost, and J.-F. Joanny. Instabilities of monolayered epithelia: shape and structure of villi and crypts. *Phys. Rev. Lett.*, **107**:078104, 2011.

[45] M. Basan, J. Prost, J.-F. Joanny, and J. Elgeti. Dissipative particle dynamics simulations for biological tissues: rheology and competition. *Phys. Biol.*, **8**(2):026014, 2011.

[46] S. A. Sandersius, M. Chuai, C. J. Weijer, and T. J. Newman. A 'chemotactic dipole' mechanism for large-scale vortex motion during primitive streak formation in the chick embryo. *Phys. Biol.*, **8**:045008, 2011.

[47] R. M. Donlan. Biofilms: microbial life on surfaces. *Emerg. Infect. Dis.*, **8**:881–890, 2002.

[48] M. Fletcher. Bacterial biofilms and biofouling. *Curr. Opin. Biotechnol.*, **5**(3):302–306, 1994.

[49] M. B. Miller and B. L. Bassler. Quorum sensing in bacteria. *Annu. Rev. Microbiol.*, **55**:165–199, 2001.

[50] J. W. Costerton, P. S. Stewart, and E. P. Greenberg. Bacterial biofilms: a common cause of persistent infections. *Science (80-.).*, **284**(5418):1318–22, 1999.

[51] L. R. Hoffman, D. A. D'Argenio, M. J. MacCoss, Z. Zhang, R. A. Jones, and S. I. Miller. Aminoglycoside antibiotics induce bacterial biofilm formation. *Nature*, **436**:1171–1175, 2005.

[52] D. G. Davies, M. R. Parsek, J. P. Pearson, B. H. Iglewski, J. W. Costerton, and E. P. Greenberg. The involvement of cell-to-cell signals in the development of a bacterial biofilm. *Science*, **280**:295–298, 1998.

[53] J. N. Wilking, V. Zaburdaev, M. De Volder, R. Losick, M. P. Brenner, and D. A. Weitz. Liquid transport facilitated by channels in Bacillus subtilis biofilms. *Proc. Natl. Acad. Sci. U. S. A.*, **110**(3):848–52, 2013.

[54] E. Ben-Jacob, I. Cohen, and H. Levine. Cooperative self- organization of microorganisms. *Adv. Phys.*, (May 2013):37–41, 2000.

[55] C. D. Nadell, J. B. Xavier, and K. R. Foster. The sociobiology of biofilms. *FEMS Microbiol. Rev.*, **33**:206–224, 2009.

[56] S. Mitri, J. a. B. Xavier, and K. R. Foster. Social evolution in multispecies biofilms. *Proc. Natl. Acad. Sci. U. S. A.*, **108 Suppl**:10839–10846, 2011.

[57] D. Monroe. Looking for chinks in the armor of bacterial biofilms. *PLoS Biol.*, **5**(11):e307, 2007.

[58] E. Ben-Jacob, O. Schochet, A. Tenenbaum, I. Cohen, A. Czirók, and T. Vicsek. Generic modelling of cooperative growth patterns in bacterial colonies. *Nature*, **368**(6466):46–9, 1994.

[59] J. U. Kreft, G. Booth, and J. W. Wimpenny. BacSim, a simulator for individual-based modelling of bacterial colony growth. *Microbiology*, **144 (Pt 1**:3275–87, 1998.

[60] J. B. Xavier, C. Picioreanu, and M. C. M. van Loosdrecht. A framework for multidimensional modelling of activity and structure of multispecies biofilms. *Environ. Microbiol.*, **7**:1085–1103, 2005.

[61] L. A. Lardon, B. V. Merkey, S. Martins, A. Dötsch, C. Picioreanu, J.-U. Kreft, and B. F. Smets. iDynoMiCS: next-generation individual-based modelling of biofilms. *Environ. Microbiol.*, **13**(9):2416–34, 2011.

[62] H. Fujikawa and M. Matsushita. Fractal Growth of Bacillus subtilis on Agar Plate. *J. Phys. Soc. Jpn*, 1989.

[63] J. Shapiro. The sigificances of bacterial colony patterns. *Bioessays*, (i), 1995.

[64] J.-U. Kreft. Biofilms promote altruism. *Microbiology*, **150**(Pt 8):2751–60, 2004.

[65] J. B. Xavier and K. R. Foster. Cooperation and conflict in microbial biofilms. *Proc. Natl. Acad. Sci.*, **104**(3):876–881, 2007.

[66] O. Hallatschek, P. Hersen, S. Ramanathan, and D. R. Nelson. Genetic drift at expanding frontiers promotes gene segregation. *Proc. Natl. Acad. Sci. U. S. A.*, **104**(50):19926–30, 2007.

[67] O. Hallatschek and D. R. Nelson. Life at the front of an expanding population. *Evolution*, **64**(1):193–206, 2010.

[68] K. Kawasaki, A. Mochizuki, M. Matsushita, T. Umeda, and N. Shigesada. Modeling spatio-temporal patterns generated by Bacillus subtilis. *J. Theor. Biol.*, **188**(2):177–85, 1997.

[69] J. D. Murray. *Mathematical Biology, Vol. 2*. Springer-Verlag, Berlin, 2003.

[70] D. Frenkel and B. Smit. *Understanding molecular simulation*. Academic Press, London, 1996. ISBN 0-12-267370-0.

[71] D. Helbing, M. Treiber, A. Kesting, and M. Schönhof. Theoretical vs. empirical classification and prediction of congested traffic states. *Eur. Phys. J. B*, **69**(4):583–598, 2009.

[72] M. Treiber, A. Kesting, and D. Helbing. Three-phase traffic theory and two-phase models with a fundamental diagram in the light of empirical stylized facts. *Transp. Res. Part B Methodol.*, **44**(8-9):983–1000, 2010.

[73] D. Helbing, I. Farkas, and T. Vicsek. Simulating dynamical features of escape panic. *Nature*, **407**(6803):487–90, 2000.

[74] D. Balcan, V. Colizza, B. Gonçalves, H. Hu, J. J. Ramasco, and A. Vespignani. Multiscale mobility networks and the spatial spreading of infectious diseases. *Proc. Natl. Acad. Sci. U. S. A.*, **106**(51):21484–9, 2009.

[75] M. Ajelli, B. Gonçalves, D. Balcan, V. Colizza, H. Hu, J. J. Ramasco, S. Merler, and A. Vespignani. Comparing large-scale computational approaches to epidemic modeling: agent-based versus structured metapopulation models. *BMC Infect. Dis.*, **10**(1):190, 2010.

[76] A. J. McLane, C. Semeniuk, G. J. McDermid, and D. J. Marceau. The role of agent-based models in wildlife ecology and management. *Ecol. Modell.*, **222**(8):1544–1556, 2011.

[77] Blythe, R. A. Neutral evolution: A null model for language dynamics. *Adv. Compl. Sys.*, **15**:1150015, 2011.

[78] V. Loreto, A. Mukherjee, and F. Tria. On the origin of the hierarchy of color names. *Proc. Natl. Acad. Sci. U. S. A.*, **109**(18):6819–24, 2012.

[79] E. Samanidou, E. Zschischang, D. Stauffer, and T. Lux. Agent-based models of financial markets. *Reports Prog. Phys.*, **70**(3):409–450, 2007.

[80] S. Gualdi, M. Tarzia, F. Zamponi, and J.-P. Bouchaud. Tipping points in macroeconomic Agent-Based models. *J. Econ. Dyn. Cont.*, 2014, in press.

[81] J.-P. Bouchaud. Crises and collective socio-economic phenomena: simple models and challenges. *J. Stat. Phys.*, **151**:567–606.

[82] E. H. Stanley. Scaling, universality, and renormalization: Three pillars of modern critical phenomena. *Rev. Mod. Phys.*, **71**(2), 1999.

[83] L. P. Kadanoff. Scaling and universality in statistical physics. *Physica A*, **163**(1), 1990.

[84] L. Verlet. Computer 'experiments' on classical fluids. i. thermodynamical properties of lennard-jones molecules. *Phys. Rev.*, **159**:98–103, 1967.

[85] W. Mattson and B. Rice. Near-neighbor calculations using a modified cell-linked list method. *Comp. Phys. Comm.*, **119**(135), 1999.

[86] L. Landau. On the theory of phase transitions. *Zh. Eksp. Teor. Fiz.*, **7**:19–32, 1937.

[87] S. R. de Groot and P. Mazur. *Non-equilibrium Thermodynamics*. Dover, 1985.

[88] R. A. Fisher. The Wave of Advance of Advantageous Genes. *Ann. Eugen.*, **7**:355–369, 1937.

[89] W. H. Press, S. A. Teukolsky, W. T. Vetterling, and B. P. Flannery. *Numerical Recipes, 3rd Edition.* Cambridge University Press, Cambridge, 2007.

[90] J. G. Charney, R. Fjrtoft, and J. von Neumann. Numerical integration of the barotropic vorticity equation. *Tellus*, **2**:237–254, 1950.

[91] M. Nagy, T. Daruka, and T. Vicsek. New aspects of the continuous phase transition in the scalar noise model (snm) of collective motion. *Physica A*, **373**(445), 2007.

[92] M. Aldana, V. Dossetti, C. Huepe, V. M. Kenkre, and H. Larralde. Phase transitions in systems of self-propelled agents and related network model. *Phys. Rev. Lett.*, **98**:095702, 2007.

[93] H. Chaté, F. Ginelli, and F. Raynaud. Modeling collective motion: variations on the vicsek model. *Eur. Phys. J. B*, **64**(3), 2008.

[94] T. Ihle. Kinetic theory of flocking: Derivation of hydrodynamic equations. *Phys. Rev. E*, **83**(3):030901, 2011.

[95] F. Ginelli and H. Chaté. Relevance of Metric-Free Interactions in Flocking Phenomena. *Phys. Rev. Lett.*, **105**(16):168103, 2010.

[96] A. Peshkov, S. Ngo, E. Bertin, H. Chaté, and F. Ginelli. Continuous Theory of Active Matter Systems with Metric-Free Interactions. *Phys. Rev. Lett.*, **109**(9):098101, 2012.

[97] J. Tailleur and M. Cates. Statistical Mechanics of Interacting Run-and-Tumble Bacteria. *Phys. Rev. Lett.*, **100**(21):218103, 2008.

[98] M. E. Cates, D. Marenduzzo, I. Pagonabarraga, and J. Tailleur. Arrested phase separation in reproducing bacteria creates a generic route to pattern formation. *Proc. Natl. Acad. Sci. U. S. A.*, **107**(26):11715–20, 2010.

[99] M. Schnitzer. Theory of continuum random walks and application to chemotaxis. *Phys. Rev. E*, 1993.

[100] F. Peruani, J. Starruß, V. Jakovljevic, L. Sø gaard Andersen, A. Deutsch, and M. Bär. Collective Motion and Nonequilibrium Cluster Formation in Colonies of Gliding Bacteria. *Phys. Rev. Lett.*, **108**(9):098102, 2012.

[101] H. P. Zhang, A. Beer, E. L. Florin, and H. L. Swinney. Collective motion and density fluctuations in bacterial colonies. *Proc. Natl. Acad. Sci. USA*, **107**(31), 2010.

[102] F. Peruani, A. Deutsch, and M. Br. Nonequilibrium clustering of self-propelled rods. *Phys. Rev. E*, **74**:030904, 2006.

[103] A. G. Thompson, J. Tailleur, M. E. Cates, and R. A. Blythe. Lattice models of nonequilibrium bacterial dynamics. *J. Stat. Mech. Theory Exp.*, **2011**(02):P02029, 2011.

[104] F. Peruani, L. Schimansky-Geier, and M. Bär. Cluster dynamics and cluster size distributions in systems of self-propelled particles. *Eur. Phys. J. Spec. Top.*, **191**(1):173–185, 2011.

[105] V. Schaller, C. Weber, C. Semmrich, E. Frey, and A. R. Bausch. Polar patterns of driven filaments. *Nature*, **467**(7311):73–7, 2010.

[106] V. Schaller, C. A. Weber, B. Hammerich, E. Frey, and A. R. Bausch. Frozen steady states in active systems. *Proc. Natl. Acad. Sci. U. S. A.*, **108**(48):19183–8, 2011.

[107] M. Eden. A two-dimensional growth process. In J. Neyman, editor, *Proc. 4th Berkeley Symp. Math. Probab.*, pages 223–239. University of California Press, 1961.

[108] M. Kardar, G. Parisi, and Y.-C. Zhang. Dynamic Scaling of Growing Interfaces. *Phys. Rev. Lett.*, **56**:889–892, 1986.

[109] F. Family and T. Vicsek. Scaling of the active zone in the Eden process on percolation networks and the ballistic deposition model. *J. Phys. A. Math. Gen.*, **18**(2):L75–L81, 1985.

[110] T. Witten and L. Sander. Diffusion-Limited Aggregation, a Kinetic Critical Phenomenon. *Phys. Rev. Lett.*, **47**:1400–1403, 1981.

[111] J. a. B. Xavier, E. Martinez-Garcia, and K. R. Foster. Social evolution of spatial patterns in bacterial biofilms: when conflict drives disorder. *Am. Nat.*, **174**(1):1–12, 2009.

[112] S. Mitri, J. a. B. Xavier, and K. R. Foster. Social evolution in multispecies biofilms. *Proc. Natl. Acad. Sci. U. S. A.*, **108 Suppl**:10839–46, 2011.

[113] D. Volfson, S. Cookson, J. Hasty, and L. S. Tsimring. Biomechanical ordering of dense cell populations. *Proc. Natl. Acad. Sci. U. S. A.*, **105**(40):15346–51, 2008.

[114] L. D. Landau and E. M. Lifschitz. *Theory of Elasticity, 3rd ed.* Elsevier, Oxford, 2008.

[115] E. J. Wentland, P. S. Stewart, C. T. Huang, and G. A. McFeters. Spatial variations in growth rate within Klebsiella pneumoniae colonies and biofilm. *Biotechnol. Prog.*, **12**(3):316–21.

[116] R. Milo, P. Jorgensen, U. Moran, G. Weber, and M. Springer. BioNumbers–the database of key numbers in molecular and cell biology. *Nucleic Acids Res.*, **38**:D750–D753, 2010.

[117] H. H. Tuson, G. K. Auer, L. D. Renner, M. Hasebe, C. Tropini, M. Salick, W. C. Crone, A. Gopinathan, K. C. Huang, and D. B. Weibel. Measuring the stiffness of bacterial cells from growth rates in hydrogels of tunable elasticity. *Mol. Microbiol.*, **84**(5):874–91, 2012.

[118] A. Varma, B. W. Boesch, and B. O. Palsson. Stoichiometric interpretation of Escherichia coli glucose catabolism under various oxygenation rates. *Appl. Envir. Microbiol.*, **59**(8):2465–2473, 1993.

[119] L. Mignot and G.-A. Junter. Diffusion in immobilized-cell agar layers: influence of microbial burden and cell morphology on the diffusion coefficients ofl-malic acid and glucose. *Appl. Microbiol. Biotechnol.*, **32**(4):418–423, 1990.

[120] I. Klapper and J. Dockery. Finger Formation in Biofilm Layers. *SIAM J. Appl. Math.*, **62**(3):853–869, 2002.

[121] H. Darcy. *Les fontaines publiques de la ville de Dijon.* 1856.

[122] J. Monod. The growth of bacterial cultures. *Annu. Rev. Microbiol.*, **3**(1):371–394, 1949.

[123] S. J. Pirt. The Maintenance Energy of Bacteria in Growing Cultures. *Proc. R. Soc. B Biol. Sci.*, **163**(991):224–231, 1965.

[124] J. Russell and G. Cook. Energetics of bacterial growth: balance of anabolic and catbolic reactions. *Microbiol. Rev.*, **59**(1), 1995.

[125] L. Z. Pipe and M. J. Grimson. Spatial-temporal modelling of bacterial colony growth on solid media. *Mol. Biosyst.*, **4**(3):192–8, 2008.

[126] A. Seminara, T. E. Angelini, J. N. Wilking, H. Vlamakis, S. Ebrahim, R. Kolter, D. A. Weitz, and M. P. Brenner. Osmotic spreading of Bacillus subtilis biofilms driven by an extracellular matrix. *Proc. Natl. Acad. Sci. U. S. A.*, **109**(4):1116–21, 2012.

[127] K. D. Young. The selective value of bacterial shape. *Microbiol. Mol. Biol. Rev.*, **70**(3):660–703, 2006.

[128] M. A. Bates and D. Frenkel. Phase behavior of two-dimensional hard rod fluids. *J. Chem. Phys.*, **111**(12), 2000.

[129] M. Basan, T. Risler, J.-F. Joanny, X. Sastre-Garau, and J. Prost. Homeostatic competition drives tumor growth and metastasis nucleation. *HFSP J.*, **3**(4):265–72, 2009.

[130] J. Folkman. Tumor angiogenesis: therapeutic implications. *N. Engl. J. Med.*, **285**:182–186, 1971.

[131] D. Hanahan and R. Weinberg. The hallmarks of cancer. *Nature*, **100**(1):57–70, 2000.

[132] D. Drasdo, S. Hoehme, and M. Block. On the Role of Physics in the Growth and Pattern Formation of Multi-Cellular Systems: What Can We Learn from Individual-Cell Based Models? *J. Stat. Phys.*, **128**(1-2):287–345, 2007.

[133] B. I. Shraiman. Mechanical feedback as a possible regulator of tissue growth. *Proc. Natl. Acad. Sci. U. S. A.*, **102**(9):3318–23, 2005.

[134] A. Brú, J. Pastor, I. Fernaud, I. Brú, S. Melle, and C. Berenguer. Super-Rough Dynamics on Tumor Growth. *Phys. Rev. Lett.*, **81**(18):4008–4011, 1998.

[135] A. Brú, S. Albertos, J. Luis Subiza, J. L. García-Asenjo, and I. Brú. The universal dynamics of tumor growth. *Biophys. J.*, **85**(5):2948–2961, 2003.

[136] K. S. Korolev, M. J. I. Müller, N. Karahan, A. W. Murray, O. Hallatschek, and D. R. Nelson. Selective sweeps in growing microbial colonies. *Phys. Biol.*, **9**(2):026008, 2012.

[137] M. Kimura. Evolutionary rate at the molecular level. *Nature*, **217**(5129), 1968.

[138] J. Masel. Genetic drift. *Curr. Biol.*, **21**(20), 2011.

[139] R. Lehe, O. Hallatschek, and L. Peliti. The rate of beneficial mutations surfing on the wave of a range expansion. *PLoS Comput. Biol.*, **8**(3):e1002447, 2012.

[140] M. Doi and S. F. Edwards. *The Theory of Polymer Dynamics*. Oxford University Press, Oxford, 1990.

[141] M. A. Nowak. *Evolutionary Dynamics*. Belknap/Harvard, Cambridge, Massachusetts, 2006.

[142] D. L. Hartl and A. G. Clark. *Principles of Population Genetics, 4th edition*. Sinauer, Sunderland, MA, 1997.

[143] D. S. Dean. *J. Phys. A Math. Gen.*, **29**:L613–L617, 1996.

[144] K. Itō. On stochastic differential equations. *Memoirs, American Mathematical Society*, **4**:1–51, 1951.

[145] B. Øksendal. *Stochastic Differential Equations. An Introduction with Applications*. Springer, 2000.